Scholars' Mine

Summer 2012

Complex oxides as novel transparent conductors

Altynbek Murat

Follow this and additional works at: https://scholarsmine.mst.edu/doctoral_dissertations

Part of the Physics Commons

Department: Physics

Recommended Citation

COMPLEX OXIDES AS NOVEL TRANSPARENT CONDUCTORS

by

ALTYNBEK MURAT

A DISSERTATION

Presented to the Faculty of the Graduate School of the

MISSOURI UNIVERSITY OF SCIENCE AND TECHNOLOGY

In Partial Fulfillment of the Requirements for the Degree

DOCTOR OF PHILOSOPHY

in

PHYSICS

2012

Approved by

Dr. Julia E. Medvedeva, Advisor
Dr. George D. Waddill
Dr. Paul E. Parris
Dr. Yew San Hor
Dr. Jay A. Switzer

PUBLICATION DISSERTATION OPTION

This dissertation has been prepared in the form of sections written in normal dissertation style and sections consisting of three articles that have been published or submitted for publication. Sections 1, 2, and 6 are written in normal dissertation style. Section 3 has been published in Physical Review B **85** 155101 (2012). Section 4 has been submitted for publication in Physical Review B. Section 5 is in the final preparation for submission to Physical Review B. The articles are prepared in the style utilized by the American Physical Society.

ABSTRACT

Ab-initio density functional approach is employed to investigate the structural, optical, and electronic properties of twelve undoped (non)stoichiometric multicomponent oxides with layered structure $RAMO_4$ [R^{3+}=In or Sc, A^{3+}=Al or Ga, and M^{2+}=Ca, Cd, Mg, or Zn], as candidates for novel transparent conducting oxides.

The compositional complexity of $RAMO_4$ leads to a wide range of band gaps varying from 2.45 eV for InGaCdO$_4$ to 6.29 eV for ScAlMgO$_4$. We find that despite the different band gaps in the constituent binary oxides, namely, 2–4 eV in CdO, In$_2$O$_3$, or ZnO; 5–6 eV for Ga$_2$O$_3$ or Sc$_2$O$_3$; and 7–9 eV in CaO, MgO, or Al$_2$O$_3$, the states of *all* cations contribute to the bottom of the conduction band of $RAMO_4$. We show that this hybrid nature of the conduction band originates from the unusual fivefold atomic coordination of A^{3+} and M^{2+} cations and suggests that both structurally and chemically distinct layers of $RAMO_4$ are expected to participate in carrier transport. This is consistent with the obtained isotropic electron effective mass of 0.3–0.5 m$_e$.

Next, in order to understand the carrier generation mechanism in $RAMO_4$, we have systematically investigated the formation of native point defects in three representative InAMO_4 oxides. We find that the donor antisite defects in InGaZnO$_4$ and InAlZnO$_4$ occur in higher concentrations than oxygen vacancies which are major donors in binary oxides. Also in contrast to the binary TCOs, the formation energy of cation vacancies is significantly lower in InAMO_4 owing to a large structural relaxation around the defect. As a result, the equilibrium Fermi level is pushed away from the conduction band and deeper into the band gap. The results agree well with the observed dependence of the conductivity on the oxygen partial pressure in InGaZnO$_4$.

These systematic investigations provide a significant insight into the role of chemical composition and structural complexity of $RAMO_4$ materials on the carrier generation mechanisms and the resulting properties.

ACKNOWLEDGMENTS

First and foremost, I cannot stress enough how deeply thankful I am to have worked with my advisor, Dr. Julia E. Medvedeva. I will forever be indebted to her for providing the opportunities to study fascinating research topics, as well as offering me endless support and encouragement. Without her immense guidance and motivation, none of this work would have been possible.

Moreover, I would like to express my gratitude and appreciation to Dr. George D. Waddill, Dr. Paul E. Parris, Dr. Yew San Hor, and Dr. Jay A. Switzer for taking their time to serve on my Ph.D. committee and all their help.

I would like to thank Dr. Ahmad Hasan for his encouragement, support, and most importantly advising me to purse my Ph.D.

I am very grateful to my friends at Missouri University of Science & Technology for making my stay in Rolla very interesting, enjoyable, and for all the great memories.

Finally, I am very thankful to my parents, my sister Altynjan, and my loving wife Marina for their endless love, encouragement, patience, and unwavering support. Without their love and support, I would not have made it.

TABLE OF CONTENTS

LIST OF ILLUSTRATIONS

LIST OF TABLES

1. INTRODUCTION

1.1. OVERVIEW

Transparent conducting oxides (TCOs) are unique materials that exhibit high optical transparency in the visible region and controllable nearly-metallic electrical conductivity. The range of technological applications and devices which use TCO as a vital component, is remarkable: it includes flat panel displays, electrochromic and smart windows, photovoltaic cells, and transparent electronics [1, 2, 3].

The current TCO market is mainly dominated by doped binary post-transition metal oxides such as In_2O_3, SnO_2, CdO, and ZnO. Obtaining a high electrical conductivity while maintaining a good optical transparency remains challenging even in the conventional TCOs. Large carrier concentrations required for improved conductivity lead to significant optical absorption and also limit the carrier mobility due to ionized impurity scattering [1]. Thus, achieving optimal device performance requires deep understanding of the fundamentals behind the complexity of these unique materials.

Until recently, much of the research work and development in the TCO field has been primarily limited to optimizing and improving the performance of conventional binary n-type TCOs [1, 3, 4]. However, high worldwide demand for TCO-based technological devices, as well as rapid development of novel TCO-based applications, stimulated the search for alternative TCO materials, those that are more efficient, cost effective, and have broader range of both electrical and optical properties [1, 3, 5]. As a result, the number of research groups working in the field of TCOs increased dramatically in the recent years, and a variety of novel TCO materials with optical and electronic properties controllable via chemical composition has been introduced [3, 5]. The novel TCOs include multicomponent oxides with ternary (such as Cd_2SnO_4, $ZnGa_2O_4$, and $ZnSnO_3$) and quaternary (e.g., $InGaO_3(ZnO)$) compositions as well

as solid solutions (e.g., $Ga_{2-2x}In_{2x}O_3$). These complex TCOs are primarily based on the composition of the conventional TCOs, as illustrated in Fig. 1.1 [1, 2, 3, 6, 7]. In particular, among the successful multicomponent oxides are the crystalline and amorphous $InGaO_3(ZnO)_m$ ($m \leq 4$) TCO and complex $RAO_3(MO)_m$ compounds (where R=In; A=Ga, Al; M=Divalent Cation; m=1-11) with layered structure, which have been under several investigations [8, 9, 10, 11]. These materials have been already employed as a conducting channel layer in transparent thin-film transistors (TFTs) [12].
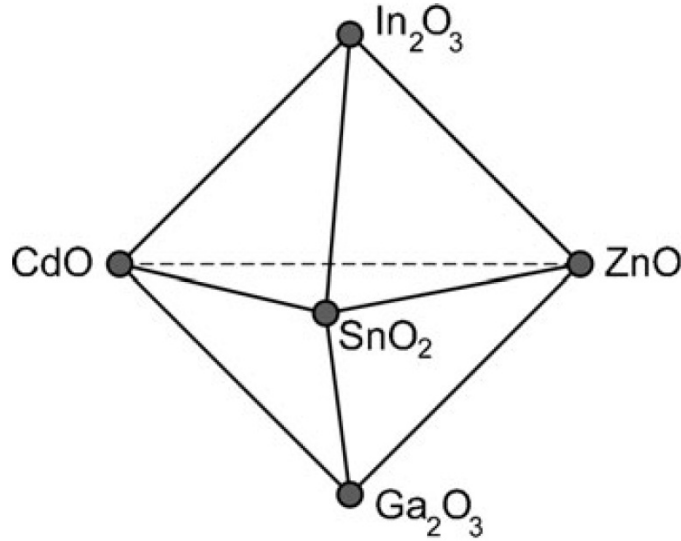
Figure 1.1: Composition space for the conventional TCO materials. Most of the current complex TCOs are based on this composition space.

The main advantage of the multicomponent TCOs is the ability to offer a wide range of tunable electrical and optical properties. These properties include band gaps, band offsets, carrier concentrations, and carrier transport that can be benefitted by a variety of TCO-based applications, such as high performance solar cells and invisible electronics [13, 14]. In addition, multicomponent oxides offer a chance to go beyond the conventional oxides in their compositions, by utilizing the cheap and abundant light-metal oxides (such as Al, Mg, and Ca). The presence of these light-metals in multicomponent oxides is highly attractive since they help stabilize the multi-cation structure, allow for a broader optical transmission window

due to a larger band gap, and also help control the carrier content while preserving the carrier mobility [3, 5, 15, 16].

Yet, the multicomponent TCOs have not outperformed the conventional binary TCOs. Both the electrical conductivity and the carrier mobility achieved in the complex TCOs, such as Cd_2SnO_4 and $InGaZnO_4$, σ=100-3000 S/cm and μ=10-20 $cm^2V^{-1}s^{-1}$, respectively, are considerably lower than those achieved in the binary TCOs. For example, the highest conductivity observed, specifically, in Sn doped In_2O_3 (ITO) materials, is σ=5-10$\times 10^3$ S/cm whereas the mobility is μ=50-1000 $cm^2V^{-1}s^{-1}$ [10, 13, 17, 18].

To understand the origin of the limited conductivity and carrier mobility in multicomponent oxides, as well as to shed light on the role played by each constituent oxide, a more thorough and systematic investigation of the structural, electronic, and optical properties as well as carrier generation mechanisms in complex oxides is needed [19]. For this, ab-initio methods based on the density functional theory have proven to be useful [20, 21, 22]. Electronic band structure investigations can (i) provide accurate description of the structural, electronic, and optical properties of undoped stoichiometric and nonstoichiometric oxides, and (ii) help develop fundamental understanding of the microscopic origins of the complex materials behavior. Moreover, the availability and the advancement of high performance computers, as well as an increased set of theoretical and ab-initio methods opened up possibilities to systematically investigate and knowledgeably manipulate the properties of known TCOs for improved performance as well as to search for novel TCO candidates beyond the conventional post transition-metal oxides [1, 3, 21].

1.2. CONVENTIONAL BINARY TCOS

This section is devoted to a review of the current status and the microscopic properties of conventional TCOs, based on the results of both experimental and theoretical investigations.

Conventional TCOs [such as F doped SnO_2, Sn doped In_2O_3 (ITO), and F or Al doped ZnO] are, primarily, the oxides of group IIB-IVB metals. They are wide-band-gap insulators in their un-doped stoichiometric state, with a direct (optical) band gap above 3 eV. The experimental direct band gaps obtained for the conventional host oxides are 3.5–3.7 eV for In_2O_3, 3.1–3.6 eV for ZnO, and 3.6–4 eV for SnO_2. The obtained experimental isotropic effective masses are 0.28–0.35 m_e for In_2O_3, 0.23–0.30 m_e for SnO_2, and 0.28–0.32 m_e for ZnO, respectively, given in the units of the electron mass, m_e [1, 3, 23]. Alone, the above basic host properties cannot explain the differences in the observed conductivities, given in Table 1.1, suggesting that carrier generation mechanism plays a critical role in the resulting electrical properties.

Table 1.1: List of some of the representative conventional TCOs with their highest approximate conductivities σ and mobilities μ obtained experimentally. Also, their characteristic properties desired for various TCO-based applications are listed [2].

TCOs	σ (10^3 S/cm)	μ (cm^2/V·s)	Characteristic property
In_2O_3:Sn	10	100	Highest conductivity
SnO_2:F	5	70	Highest work function, lowest cost
ZnO:Al	6.5	50	Easy to etch
ZnO:F	2.5	30	Highest transparency, least toxic

It is important and instructive to know and assess the trend of capabilities of conventional TCOs based on the observed results. Gordon et al. [2] suggested that effective TCO materials should have both a high electrical conductivity and a low absorption of visible light. Hence, a figure of merit for TCO materials can be defined

as the ratio between the observed electrical conductivity and the optical absorption coefficient. Within the Boltzmann formulation, the electrical conductivity σ can be defined as $\sigma = ne\mu$, where μ is the electron mobility, n is the carrier concentration, and e is the charge of the electron. In addition, mobility μ can be expressed as $\mu = e\tau/m^*$, where τ is the relaxation time and m^* is the effective mass of the carriers.

Among the conventional TCOs, as listed in Table 1.1, the highest attained experimental conductivity and electron concentrations are in the following order: In_2O_3:Sn $>$ZnO:Al $>$ SnO_2:F $>$ ZnO:F [2]. In terms of the figure of merit, they follow a different order: ZnO:F $>$ZnO:Al $>$ In_2O_3:Sn $>$$SnO_2$:F [2]. In addition, from the technological point of view, factors and characteristic properties, such as work functions, stability and durability, cost efficiency, safety, and etchability are important, playing a great role when comparing the TCO material performance [2]. Thus, when assessed on several factors, each conventional TCO has its own merits which are suitable and desired for certain TCO-based applications and devices. As a result, the above four compounds, although best-performing in terms of conductivity, are insufficient for rapidly developing TCO-based applications and development of alternative TCOs is required [3].

Understanding the theoretical fundamentals of conventional TCOs is the foundation for the success of novel TCO materials' development as well as for improving the performance of the existing ones. Within this foundation, electronic band structure investigations can be used to understand the structural, optical, and electrical properties of the TCO materials [1, 3, 5]. From an electronic band structure point of view, the binary conventional TCOs has both an empty conduction band and a completely-filled valance band, as shown in Figure 1.2(a). In order to become conducting, these insulators have to be degenerately doped to shift the Fermi level E_F up into the conduction band, as shown in Figure 1.2(b).

Figure 1.2: (a) A schematic electronic band structure of an insulating binary oxide of conventional TCOs, with a band gap of E_g. The conduction band is a highly dispersed parabolic band resulting from interactions between metal s and oxygen p states. Here, the Fermi level, E_F, lies within the band gap E_g. (b) A schematic band structure of conventional transparent and conducting oxide. The conductivity resulted from the degenerate doping that shifted the Fermi level E_F up into the conduction band via a Burstein-Moss shift, E_{BM}.

The most important characteristic, common to all conventional n-type TCOs, is the highly dispersed, single free-electron-like (parabolic) conduction band, as illustrated in Fig. 1.2 [24, 25, 26]. When the material is properly doped, this high dispersion provides a high mobility of extra carriers because of their small effective mass. Also, it results in low optical absorption because of the low density of states in the dispersed conduction band. In addition, due to this highly dispersed conduction band, the Fermi level E_F shifts deep into the conduction band, which is called the Burstein-Moss (BM) shift, E_{BM} [27, 28]. This BM shift results in several optical

transitions, including: inter-band transitions from the valance band to the conduction band E_v; transitions from the partially filled conduction band to the next empty band E_c; and intra-band transitions within the conduction band E_i. All these transitions contribute to the optical absorption, but their intensity depends on the density of states.

Both the high mobility of extra carriers and the high carrier concentration contribute to better conductivity (conductivity $\sigma = ne\mu$, where n is the carrier concentration, μ is the electron mobility, and e is the charge of the electron). However, for better performance, increasing the carrier mobility is preferred over increasing the carrier concentration because high carrier concentrations may result in an increase of optical absorption [26]. Thus, obtaining a desired high conductivity without sacrificing the low optical absorption (transparency) is very challenging and considered as one of the major bottlenecks of the TCO materials development [1, 7].

The calculated electronic band structures of conventional TCOs shown in Figure 1.3 are similar in that they share the key characteristics of a highly dispersed parabolic conduction band. This conduction band arises from the interaction between the oxygen $2p$ and metal s states. The valence bands are formed from the oxygen $2p$ states. From the plots of partial density of states, illustrated in Figure 1.3, the conduction band includes similar contributions from both the oxygen $2p$ and metal ns states. This is critical for the charge transport - it represents a uniform charge density distribution in the conduction band [15]. These states serve as a 3-dimensional network for carrier transport.

The direct band gaps obtained from first-principles band structure calculations are 3.38 eV, 3.50 eV, 3.41 eV, and 2.28 eV for In_2O_3, SnO_2, ZnO, and CdO, respectively. The calculated average electron effective masses are 0.28 m_e for In_2O_3, 0.31 m_e for SnO_2, 0.35 m_e for ZnO, and 0.23 m_e for CdO, respectively [15, 30]. These calculated values of band gaps and effective masses are in good agreement with the

Figure 1.3: Electronic band structure and partial density of states for the binary base oxides of the conventional TCOs, In_2O_3, SnO_2, ZnO, and CdO [15]. First-principles calculations within the screened-exchange local density approximation [29] is employed. In the DOS plots, the thick, dashed, and thin lines represent metal s, metal p, and oxygen p states, respectively.

previously mentioned experimental results, thus, presenting the predictive power of ab-inito methods based on the density functional theory.

Knowledge of the basic properties of conventional binary TCO hosts allows for further search of alternative TCO materials, such as multicomponent complex oxides.

1.3. MULTICOMPONENT TCOS

Rapid development of TCO-based applications requires TCO materials with a wide range of electronic and optical properties that are beyond what conventional binary TCOs (doped In_2O_3, SnO_2, ZnO, and CdO) can offer. In particular, broader optical properties, such as tunable band gaps and plasma frequencies, as well as controllable electrical properties, such as resistance, carrier concentration, and mobility, are required. To meet this demand, complex compounds with ternary (such as Cd_2SnO_4, $ZnGa_2O_4$, and $ZnSnO_3$) and quaternary (e.g., $InGaO_3(ZnO)$) compositions

as well as solid solutions with properties controllable via the chemical compositions, were introduced and investigated [1, 3, 6, 19, 31]. Also, investigations emerged on TCO-based materials with oxide constituents that are beyond the composition of conventional TCOs, such as $MgIn_2O_4$ which incorporates the main-group light metals (Al, Ca, and Mg) [1, 32]. Incorporation of light-metals in multicomponent oxides are desirable since they can broaden the optical transmission window due to their larger band gap [3].

Among the complex quaternary oxides, $InGaO_3(ZnO)_m$ ($m \leq 4$) TCO and other $RAO_3(MO)_m$ compounds (R=In; A=Ga, Al; M=Divalent Cation; m=1-11), with layered structure, have been the most widely investigated [8, 9, 11]. $RAO_3(MO)_m$ compounds have structurally different alternating layers of $RO_{1.5}$ and $AMO_{2.5}$, as shown in Figure 1.4. It has been reported [9, 33, 34] that a possible advantage of these layered materials is to increase conductivity by separating the layers where carrier donors (usually, aliovalent substitutional impurities) reside and the layers that contribute to conduction. This would help to avoid charge scattering on the ionized impurities. However, the role of structural complexity and chemical composition as well as the origins of the carrier generation in these multicomponent oxides have been a subject of active debate [9, 19, 26, 35]. For example, despite the belief that the $InO_{1.5}$ ($RO_{1.5}$) layer is responsible for conductivity [9, 26] in $InGaO_3(ZnO)$, another study suggested that the $InGaO_3(ZnO)$ might be a Zn 4s conductor [34]. Recent first-principles electronic band structure investigations of several undoped stoichiometric multicomponent $RAMO_4$ oxides with layered structure [36, 37] revealed that atoms from both structurally and chemically distinct $RO_{1.5}$ and $AMO_{2.5}$ layers contribute comparably to the conduction band. This finding suggested that an isotropic charge transport can be achieved in $RAMO_4$ compounds once they are degenerately doped.

Figure 1.4: The unit cell of $RAMO_4$ with a rhombohedral $R\bar{3}m$ structure. Three similar blocks consisting of one $RO_{1.5}$ and two $AMO_{2.5}$ layers alternate along the [0001] direction. A^{3+} and M^{2+} ions are distributed randomly.

Ab-initio investigations of multicomponent $InGaZnO_4$ also showed that its electronic properties such as highly dispersed s-like conduction band, wide band-gap, and small isotropic effective mass, are similar to those in the constituent TCO hosts [15, 19]. For example, the calculated band gaps are 3.38 eV for In_2O_3, 4.91 eV for Ga_2O_3 and 3.41 eV for ZnO while it is 3.29 eV for the multicomponent $InGaZnO_4$. Similarly, the calculated average electron effective masses are 0.28 m_e for In_2O_3, 0.34 m_e for Ga_2O_3, 0.35 m_e for ZnO, and 0.34 m_e for $InGaZnO_4$. Despite the similar host properties, the obtained experimental conductivities (σ) and mobilities (μ) in the complex multicomponent TCO are much lower compared to those obtained in conventional TCOs. The highest obtained conductivities are between 120 to 500 S/cm and the mobilities (μ) are up to 24 $cm^2V^{-1}s^{-1}$ in the complex multicomponent TCO [3, 5, 9, 10, 13, 17, 18, 35] whereas the constituent In_2O_3 and ZnO have conductivities as high as 10^3 to 10^4 S/cm and mobilities up to 1000 $cm^2V^{-1}s^{-1}$ [1, 2, 38].

Hence, one needs to understand why the complex oxides have not yet outperformed the conventional TCOs, despite similar host properties (band gaps, effective mass) and the uniform conduction band in the complex TCO hosts. Based on the expected charge transport properties in RAMO$_4$, neither the TCO hosts nor the host properties but likely the carrier generation mechanism is responsible for the performance limitations of complex TCOs, such as the lower mobilities and conductivities mentioned earlier. Since the carrier generation mechanism behind the conductivity of the complex multicomponent oxides has not been established, it needs to be studied further [1, 3, 25].

Moreover, in multicomponent oxides containing the cations from both groups (i.e., post-transition metals (In, Zn) and light main-group metals (Mg, Al)), the respective energy locations of the cations' states may not be the same as in single-oxide constituents due to the interaction between different cations via a shared oxygen neighbor. Indeed, it was found [19] that the bottom of the conduction band in RAMO$_4$ is governed by the states of *all* cations despite the fact that the band gaps in the corresponding basis oxides differ significantly (3.38 eV for In$_2$O$_3$, 3.41 eV for ZnO, 9.08 eV for Al$_2$O$_3$, and 7.55 eV for MgO). Moreover, the electronic properties in a multicomponent oxide may deviate significantly from that expected from the electronic band structures of the single-cation (basis) oxides owing to the differences in the interatomic distances and the atomic coordination numbers in the complex oxide as compared to those in the bulk ground-state (lowest energy) structures of the constituent oxides.

Thus, a more thorough understanding and a more systematic first-principles investigation of the properties of layered RAMO$_4$-based multicomponent oxides would contribute to the advancement of known and the development of novel TCOs. Factors that promote these investigations include:

- Multicomponent oxides offer a way to tune the structural, electronic, and optical properties desired for specific applications via chemical composition. The tunability of the properties makes the multicomponent oxides one of the most appealing materials for further investigations.

- Multicomponent oxides offer a possibility to go beyond the composition of conventional binary oxides by utilizing the cheap, abundant light-metal oxides (such as Mg, Al, and Ca) in their compositions. Presence of these light metals in multicomponent TCOs is attractive for achieving a broader optical transmission window associated with a wider band gap. This may allow one to introduce more multicomponent compounds as novel TCO candidates and supports the need to understand the role and effect of structural peculiarities and chemical composition.

- The carrier generation mechanism behind the conductivity of these multicomponent oxides has not been established. Different carrier generation mechanisms need to be studied to truly understand what makes them conducting. Thus, it is crucial to have the knowledge of the current status of carrier generation in the conventional TCOs as a groundwork for creating defects. A detailed discussion on the carrier generation in TCO hosts appears in the following section.

1.4. CARRIER GENERATION IN TCO HOSTS

There are two major ways to introduce carriers in wide-band-gap oxides, the TCO hosts. The first way is by varying the growth conditions (growth temperature and oxygen partial pressure) which controls the concentration of native (intrinsic) point defects in the oxide sample. These imperfections in the crystal lattice involve only the constituent elements and may include vacancies (missing atoms at regular lattice positions) and interstitials (extra atoms occupying interstices in the lattice). The second way is via intentional (extrinsic) doping with aliovalent substitutional impurities [39].

The best performing conventional binary TCOs employ substitutional impurity doping. They are, primarily, Sn doped In_2O_3 (ITO), F doped SnO_2, F or Al doped ZnO, and Sn doped CdO. Some of the highest conductivities achieved among these are 42×10^3 S/cm in Sn doped CdO, 5×10^3 S/cm in F doped SnO_2, and 10×10^3 S/cm in ITO [2, 6, 40]. These conductivities strongly depend on the type of the dopant - its valence, ionic size radius, and electronic configuration. For example, extensive experimental studies have been conducted on preparing ZnO films with different doping elements such as Group III (Al, Ga, and In), Group IV (Si, Ge, and Zr), and Group VII (F) elements. These studies resulted in a wide range of electrical conductivities of up to 1.2×10^3 S/cm in In doped ZnO films [6, 41]. However, in addition to the change in the electronic band structure of the host oxide due to the presence of dopant, the resulting electron transport maybe also affected by the charge compensation due to native defects which can be electron donors (anion vacancies) and acceptors (cation vacancies) [15]. The charge compensation can be understood as follows: in a wide band gap material, a donor electron can lower its energy if it falls into an empty intrinsic defect state (such as a cation vacancy state). If the energy gain exceeds the cost of creating the defect, the donor action is completely compensated by the defect if there is thermal equilibrium [3]. Thus, not only the ability to introduce different type of dopants but also the knowledge of defect physics is critical for understanding the complexity behind the carrier generation mechanism in TCOs.

Recent electronic band structure investigations [15] compared the properties of impurity doped and oxygen deficient conventional oxides. It was revealed that similar conductivity factor can be achieved in both cases. The conductivity factor is the square of the calculated electron velocity multiplied by the density of states in the vicinity of the Fermi level since the conductivity σ depends on both, the electron

group velocity and the density of states near the Fermi level, according to:

$$\sigma = \frac{2e^2}{\Omega} \sum_{k\lambda} |v_{k\lambda}|^2 \tau_{k\lambda} \delta(E_{k\lambda} - E_F). \tag{1.1}$$

Here e is the electron charge, Ω – the volume of the Brillouin zone, k – the wave vector, λ – the band index, v – the electron group velocity, $\tau(\epsilon)$ – the relaxation time, and E_F is the Fermi energy. However, the conductivity also depends on the relaxation time, and it was shown that a smaller relaxation time can be expected in case of oxygen defects as compared to impurity doped materials [15].

Here, we will discuss how native point defects in oxides can be investigated from first-principles. The formation energy of a defect in any charge state modeled using a corresponding background charge, can be calculated as a function of the Fermi level and the corresponding chemical potential:

$$E^f(E_F, \mu) = E_{defect} - E_{host} \pm \mu_\alpha + q(E_F) \tag{1.2}$$

where E_{defect} and E_{host} are the total energies for the oxide with the defect and the stoichiometric oxide in the same-size supercell, respectively; μ_α is the chemical potential of atom α added to (−) or removed from (+) the lattice; q is the defect charge state; E_F is the Fermi energy taken with respect to the top of the valence band. The chemical potential $\mu_\alpha = \mu_\alpha^0 + \Delta\mu_\alpha$ is taken with respect to the chemical potential μ_α^0 of the elementary metals or the O_2 molecule, whereas $\Delta\mu_\alpha$ is a deviation from the elemental chemical potential determined by the growth conditions which depend on the temperature and oxygen partial pressure [42, 43].

Once the defect formation energy E^f is determined, the concentration of the defect in the solid can be found through the relation

$$c = N_{sites} \exp(\frac{-E^f}{k_B T}) \tag{1.3}$$

where N_{sites} is the number of sites per unit volume the defect can be incorporated on, k_B is the Boltzmann constant, and T is the temperature. Equation (1.3) shows that the defects with high formation energies will occur in low concentrations and vice versa. The equilibrium Fermi level in equation 1.2 is determined from the charge neutrality condition of the material which takes into account all charged acceptor and donor defects as well as all carriers (electrons and holes) [42, 44]. Overall, the formation energy of either a native defect or an impurity and, hence, its concentration can be computed entirely from first principles [3].

Carrier generation mechanisms in binary TCOs have been investigated from first-principles [15, 19, 24, 37]. As an example of possible defects in conventional TCOs, Table 1.2 summarizes defects in ZnO. The defect notations in Table 1.2 are: V_O - oxygen vacancy, Zn_i - zinc interstitial, and Ga_{Zn}- Ga atom substituted on zinc site.

Table 1.2: Possible defects in ZnO.

Character		Defects
Native point defects	Donor:	V_O, Zn_i
	Acceptor:	V_{Zn}, O_i
Impurities(Substitutional)	Donor:	F_O, B_{Zn}, Al_{Zn}, Ga_{Zn}, In_{Zn}, H_i, Li_i
	Acceptor:	Cu_{Zn}, Li_{Zn}, N_O

One can easily formulate and compute the formation energy of any native defects or impurities from the total energies. For example, in the case of oxygen vacancy (V_O) in ZnO, the formation energy is

$$E^f(V_O^q) = E_{tot}(V_O^q) - E_{tot}(ZnO) + \mu_O + q(E_F + E_{VBM}) \tag{1.4}$$

where $E_{tot}(V_O^q)$ is the total energy of a supercell containing the oxygen vacancy in the charge state q, $E_{tot}(ZnO)$ is the total energy of a ZnO perfect crystal in the same supercell, and μ_O is the oxygen chemical potential.

Moreover, it is instructive to plot the formation energies as a function of Fermi level to examine the behavior of defects when the doping level changes. Figure 1.5 illustrates the formation energies of defects in ZnO for both oxygen-rich and metal-rich (oxygen-poor) growth conditions [44]. The oxygen-rich and metal-rich conditions correspond to $\Delta\mu_O=0$ and $\Delta\mu_{Zn}=0$, respectively. It can be seen from Fig. 1.5 that the substitutional defects such as Al_{Zn} can produce free carriers in metal-rich conditions, without being compensated by the native acceptor defects. However, in oxygen-rich conditions, Al_{Zn} is compensated by the native Zn vacancies. This compensation occurs when the formation energy of Zn vacancies becomes comparable to the formation energy of the Al_{Zn} at some Fermi energy, i.e., moving the Fermi energy to a band edge causes the spontaneous formation of that compensating defect [39, 45]. In terms of native defects, in metal-rich condition, the oxygen vacancies have the lowest formation energies when the Fermi level lies near the conduction band minimum, hence, results in highest carrier concentrations. Thus, native point defects play a critical role when determining the major defect in a material.

Figure 1.5: Calculated defect formation energies of intrinsic and extrinsic defects in ZnO, as a function of Fermi level. The dots mark the transition energies between different charge states [44].

Knowledge of the basics of doping in conventional TCOs can be applied to complex $RAMO_4$ compounds. For the multicomponent oxides, such as $InGaO_3(ZnO)$,

the free carriers were believed to be due to the formation of oxygen vacancy defects. However, based on the first-principles investigations, it was shown that the oxygen vacancies are deep defects and so can not explain the observed conductivities in these materials [46]. In marked contrast to binary oxides, the RAMO$_4$ compounds have many different possible intrinsic and extrinsic defects which can coexist, due to their structural and the chemical complexity. In addition, because of the structurally and chemically distinct layers in RAMO$_4$ compounds, there can be several different defect locations with different neighboring atoms. The possible defects for InGaZnO$_4$ can be seen from Table 1.3 which serves as an example of possible defects in RAMO$_4$ compounds. First-principles investigations of these native point defects will play a critical role in determining the carrier generation mechanisms in RAMO$_4$ compounds.

Table 1.3: Possible defects in InGaZnO$_4$.

	Donors	Acceptors
Vacancies	V$_O$	V$_{In}$, V$_{Zn}$, V$_{Ga}$
Interstitials	In$_i$, Ga$_i$, Zn$_i$	O$_i$
Cation disorder	In$_{Zn}$, Ga$_{Zn}$	Zn$_{Ga}$, Zn$_{In}$

1.5. DISSERTATION OUTLINE

We have systematically investigated the structural, optical, and electronic properties of both undoped stoichiometric and doped twelve complex multicomponent RAMO$_4$ materials (R^{3+}=In or Sc; A^{3+}=Al or Ga; and M^{2+}=Ca, Cd, Mg, or Zn) as novel TCOs. This combinatorial study allowed us to understand which composition, doping mechanism, and/or carrier concentration result in a better TCO properties as well as helped guiding us to the right materials for further research.

In our first-principles investigations, we employed highly precise, state-of-the-art, full-potential linearized augmented plane wave (FLAPW) [20, 47, 48] method based on the density functional theory (DFT) [22, 49].

Outline of this dissertations is as follows. Details of the first-principles computational methods and approaches are discussed in Section 2. In Section 3, the structural, electronic, and optical properties of the twelve undoped stoichiometric $RAMO_4$ materials are systematically investigated.

To understand how the chemical composition affects carrier generation in complex oxides, comparative investigations of non-stoichiometric $RAMO_4$ compounds were performed. In Section 4, the formation of oxygen vacancy and the resulting electronic properties are investigated both in the representative layered multicomponent oxides as well as in their corresponding binary oxide constituents. Further, in Section 5, formation of native point defects in layered multicomponent oxides are investigated.

We note that Sections 3–5 are either published or submitted (or in final preparation) for publication to a peer-reviewed journals. Thus, they have an abstract, introduction, and conclusion. In Section 6, we summarize the overall conclusions.

2. METHODS AND APPROACH

2.1. INTRODUCTION

First-principles calculations based on the density functional theory (DFT) [22, 49] have become one of the most powerful approaches that allow one not only to better understand but also to model and predict the properties of emerging complex and novel materials. In addition to the overwhelming success of the density-functional theory for the description of the ground-state properties of large material classes, the wide applicability and predictive power of the approach makes it the foundation of any modern electronic structure theory [50].

Many different DFT methods have been developed and used. The difference among these methods is mainly based on the type of basis set or the approximations for the exchange-correlation functional [22]. Both the robustness of these methods and the availability of high-performance computers allows us to choose either a specific, suitable method or combine several methods for the outcome of desired materials investigations [21].

In our investigations of the structural, optical, and electronic properties of undoped stoichiometric and nonstoichiometric multicomponent oxides, we employed the full-potential linearized augmented plane wave (FLAPW) method [20, 47, 48]. The FLAPW method is based on the DFT. In the following sections, both the DFT and the FLAPW method are briefly discussed.

2.2. DENSITY FUNCTIONAL THEORY

2.2.1. Overview. Density functional theory (DFT) is one of the most widely used quantum mechanical theories to investigate the ground state properties of many-body systems. DFT is among the most popular and successful methods available for

the electronic structure calculations of materials. Advantages of DFT include very good scaling of computational cost with the system size as well as the possibility of performing calculations on a large and complex systems [50].

The fundamental principle behind the DFT is that any property of an atomistic system can be expressed as a functional of its ground state electron density. This ground state electron density, in principle, can determine all of the information in the many-body wave-functions. For instance, the total energy of the atomistic system can be determined as a functional of its electron density.

Although the original idea of DFT was suggested by Thomas [51] and Fermi [52], the first observation and the proof of the functionals were achieved in the work of Hohenberg and Kohn [49]. For any system with more than one electron, however, the exact functionals as well as the construction of those functionals were neither known nor given by the Hohenberg and Kohn. It was the Kohn-Sham ansats [53] that made it possible to have approximations for the ground state functionals. These functionals made the DFT useful and practical. Therefore, the Hohenberg-Kohn [49] theorems and the Kohn-Sham [53] equations are the two primary core elements of the DFT.

The Hohenberg-Kohn [H-K] theorems have two important principles sets. The first H-K theorem illustrates that electron density, which depends only on three spatial coordinates, can determine the ground state properties of many-body systems. Through the use of electron density functionals, the H-K theorem reduces the many-body problem of N electrons with $3N$ spatial coordinates to three spatial coordinates. The second H-K theorem defines an energy functional for the system, proving that the correct ground state electron density minimizes this energy functional [22].

With the use of Kohn-Sham equations [53], the many-body problem of interacting electrons in a static external potential is reduced to a problem of non-interacting electrons moving in an effective potential, which makes it easier to solve. This effective potential includes the external potential and the effects of the Coulomb

interactions between the electrons, e.g., both the exchange and the correlation interactions. These interactions are difficult to model. For the many-body exchange and the correlation interactions, the actual expression is not known and approximations need to be made. The Kohn-Sham reformulation in terms of single-particle orbitals helped in the development of approximations. The basic approximation is the local-density approximation (LDA). This approximation is based on the exact exchange energy for a uniform electron gas [50].

2.2.2. Derivation and Formalism. To better understand the density functional theory, we begin with the elementary quantum mechanics. In quantum mechanics, a system's wave function Ψ contains all of the information we can possibly have about a given system. The nuclear degrees of freedom appear only in the form of a potential $v(\mathbf{r})$ acting on the electrons. As a result, the wave function depends only on the electronic coordinates which is the so-called Born-Oppenheimer approximation [54]. Non-relativistically, this wave function is calculated from Schrödinger's equation, which for a single electron moving in a potential $v(\mathbf{r})$ is

$$\left[-\frac{\hbar^2\nabla^2}{2m} + v(\mathbf{r})\right]\Psi(\mathbf{r}) = \epsilon\Psi(\mathbf{r}). \tag{2.1}$$

For a many-body problem, the Schrödinger's equation becomes

$$\left[\sum_i^N\left(-\frac{\hbar^2\nabla_i^2}{2m} + v(\mathbf{r}_i)\right) + \sum_{i<j}U(\mathbf{r}_i,\mathbf{r}_j)\right]\Psi(\mathbf{r}_1,\mathbf{r}_2\ldots,\mathbf{r}_N) = E\Psi(\mathbf{r}_1,\mathbf{r}_2\ldots,\mathbf{r}_N) \tag{2.2}$$

where N is the number of electrons and $U(\mathbf{r}_i,\mathbf{r}_j)$ is the electron-electron interaction. For a Coulomb system, electron-electron interaction energy is

$$\hat{U} = \sum_{i<j}U(\mathbf{r}_i,\mathbf{r}_j) \tag{2.3}$$

which is the same operator for any system of particles interacting via the Coulomb interaction. The kinetic energy operator is the same for any non-relativistic system:

$$\hat{T} = -\frac{\hbar^2}{2m}\sum_i \nabla_i^2.$$ (2.4)

Whether our system is an atom, a molecule, or a solid thus depends only on the potential $v(\mathbf{r})$.

$$\hat{V} = \sum_i v(\mathbf{r}_i).$$ (2.5)

A crucial note that only through the term $\hat{U}$ the single-body quantum mechanics of eq. (2.1) differ from the extremely complex many-body problem in eq. (2.2). Due to this term, the complex many-body problem equation is not separable into simpler single-particle equations.

In the usual quantum-mechanical approach to Schrödinger's equation, one first specifies the system by choosing the potential $v(\mathbf{r})$. Then plugs it into Schrödinger's equation which then solves that equation for the wave function Ψ, and calculates the observables, by taking the expectation values of operators with this wave function. Though many methods exist for solving the many-body Schrödinger's equation, these methods are very computationally resource demanding. In addition, they are very hard to apply to large and complex systems. This is where the DFT becomes practical. The DFT provides a way to systematically map the many-body problem, with $\hat{U}$, onto a single-body problem, without $\hat{U}$. This mapping leads to the point that the knowledge of particle density $n(\mathbf{r})$ implies the knowledge of the wave function and the potential, hence, all of other observables, making the particle density $n(\mathbf{r})$ the key variable in DFT.

$$n(\mathbf{r}) = N \int d^3r_2 \int d^3r_3 \ldots \int d^3r_N \Psi^*(\mathbf{r}, \mathbf{r}_2 \ldots, \mathbf{r}_N)\Psi(\mathbf{r}, \mathbf{r}_2 \ldots, \mathbf{r}_N).$$ (2.6)

The core element behind the DFT are the two remarkably powerful Hohenberg-Kohn[HK] theorems [49]. These theorems relate to any system consisting of electrons under some external potential $v(\mathbf{r})$. The first Hohenberg-Kohn theorem states that the external potential $v(\mathbf{r})$, and hence the total energy, is a unique functional of the electron density $n(\mathbf{r})$. The proof of this theorem is simple. Suppose there are two different external potentials $v_1(\mathbf{r})$ and $v_2(\mathbf{r})$ differing by more than a constant which lead to the same density $n(\mathbf{r})$. The corresponding different Hamiltonians $\hat{H}_1$ and $\hat{H}_2$ will have different ground state wavefunctions, Ψ_1 and Ψ_2, that each yield the same $n_0(\mathbf{r})$. Because Ψ_2 is not the ground state of $\hat{H}_1$ (and if the ground state is non-degenerate), using the variational principle, we can write

$$E_1 = \langle \Psi_1 | \hat{H}_1 | \Psi_1 \rangle < \langle \Psi_2 | \hat{H}_1 | \Psi_2 \rangle. \tag{2.7}$$

The last term of the above inequality can be written as

$$\langle \Psi_2 | \hat{H}_1 | \Psi_2 \rangle = \langle \Psi_2 | \hat{H}_2 | \Psi_2 \rangle + \langle \Psi_2 | \hat{H}_1 - \hat{H}_2 | \Psi_2 \rangle = E_2 + \int d^3 r [v_1(\mathbf{r}) - v_2(\mathbf{r})] n_0(\mathbf{r}) \tag{2.8}$$

so that

$$E_1 < E_2 + \int d^3 r [v_1(\mathbf{r}) - v_2(\mathbf{r})] n_0(\mathbf{r}). \tag{2.9}$$

Similarly, rewriting previous equations for the $\hat{E}_2$, gives

$$E_2 < E_1 + \int d^3 r [v_2(\mathbf{r}) - v_1(\mathbf{r})] n_0(\mathbf{r}). \tag{2.10}$$

Adding the equations 2.9 and 2.10, we get to the contradictory inequality

$$E_1 + E_2 < E_1 + E_2. \tag{2.11}$$

From Equation 2.11, it can be concluded that there cannot be two different external potentials differing by more than a constant which give rise to the same non-degenerate ground state charge density. The density uniquely determines the external potential to within a constant [50].

The second Hohenberg-Kohn theorem states that the ground state energy can be obtained variationally, where the density $n(\mathbf{r})$ that minimizes the total energy is the exact ground state density $n_0(\mathbf{r})$. For the proof of the second theorem, each property can be written as a functional of $n(\mathbf{r})$. Hence, the total energy functional is

$$E[n(\mathbf{r})] = F[n(\mathbf{r})] + \int d^3r v(\mathbf{r})n(\mathbf{r}). \qquad (2.12)$$

The Hamiltonian can be written as $\hat{H} = \hat{F} + \hat{V}$. The functional $F[n(\mathbf{r})]$ is a universal functional of the density. It includes the kinetic energy and the interaction energies:

$$F[n(\mathbf{r})] = T[n(\mathbf{r})] + U[n(\mathbf{r})]. \qquad (2.13)$$

Because the wave-function Ψ is a unique functional of the density $n(\mathbf{r})$, the expectation value of $\hat{F}$ is also a functional of $n(\mathbf{r})$. Thus,

$$F[n(\mathbf{r})] = \langle \Psi | \hat{F} | \Psi \rangle. \qquad (2.14)$$

A density that is the ground-state of some external potential is known as v-representable. Following from this, a v-representable energy functional $E_v[n(\mathbf{r})]$ can be defined in which the external potential $v(\mathbf{r})$ is unrelated to another density $n'(\mathbf{r})$,

$$E_v[n(\mathbf{r})] = F[n'(\mathbf{r})] + \int d^3r v(\mathbf{r})n'(\mathbf{r}). \qquad (2.15)$$

Using the variational principle, we can write

$$\langle \Psi' | \hat{F} | \Psi' \rangle + \langle \Psi' | \hat{V} | \Psi' \rangle > \langle \Psi | \hat{F} | \Psi \rangle + \langle \Psi | \hat{V} | \Psi \rangle \tag{2.16}$$

where Ψ is the wavefunction associated with the correct ground-state $n(\mathbf{r})$. Hence,

$$F[n'(\mathbf{r})] + \int d^3 r v(\mathbf{r}) n'(\mathbf{r}) > F[n(\mathbf{r})] + \int d^3 r v(\mathbf{r}) n(\mathbf{r}) \tag{2.17}$$

The variational principle of the second Hohenberg-Kohn theorem can then be:

$$E_v[n'(\mathbf{r})] > E_v[n(\mathbf{r})]. \tag{2.18}$$

Hohenberg-Kohn theorems do not offer a computation for the ground-state density of a system in practice. The Kohn-Sham [53] equations do offer a way to carry out the DFT calculations. To obtain the ground-state density, the variational principle is applied with respect to the one-particle wave functions. In particular, the Schrödinger equation of this auxiliary system

$$\left[-\frac{\hbar^2 \nabla^2}{2m} + V_{eff}(\mathbf{r}) \right] \Psi_i(\mathbf{r}) = \epsilon_{\mathbf{i}} \Psi_{\mathbf{i}}(\mathbf{r}) \tag{2.19}$$

yields orbitals that reproduce the density $n(\mathbf{r})$ of the original system. Then,

$$n(\mathbf{r}) = \sum_{\mathbf{i}} \mathbf{n_i} |\Psi_{\mathbf{i}}(\mathbf{r})|^{\mathbf{2}}, \tag{2.20}$$

where

$$V_{eff}(\mathbf{r}) = \mathbf{V_C}(\mathbf{r}) + \mu_{\mathbf{xc}}[\mathbf{n(\mathbf{r})}] \tag{2.21}$$

is the effective potential and ϵ_i the effective one-electron eigenvalues. Eqs. (2.19) and (2.20) are the Kohn-Sham (KS) equations and the solutions, $\psi_i(\mathbf{r})$, form an

orthonormal set. The Coulomb, or electrostatic potential, is given as

$$V_C(r) = -e^2 \sum_\alpha \frac{Z_\alpha}{|\mathbf{r} - \mathbf{R}_\alpha|} + e^2 \int dr' \frac{n(\mathbf{r}')}{\mathbf{r} - \mathbf{r}'}. \tag{2.22}$$

which can also be calculated using Poisson's equation,

$$\Delta^2 V_C(\mathbf{r}) = -4\pi \mathbf{e^2} \mathbf{q(r)} \tag{2.23}$$

where $q(\mathbf{r})$ represents both the electronic charge distribution and the positive point charges at position R_α. The exchange-correlation potential is given by

$$\mu_{xc} = \frac{\partial E_{xc}[n]}{\partial n}. \tag{2.24}$$

Because the exchange-correlation potential (and energy) are not known, approximations have to be made. The problem of solving the KS equations is a nonlinear one. The typical way of solving such problems includes beginning with an initial guess for $n(\mathbf{r})$, calculating the corresponding potential, and then solving the differential equation (2.19) for ψ_i. From these, one calculates a new density, using equation (2.20), and the process is repeated iteratively until it converges.

      2.2.3. Exchange-Correlation Functionals. The major problem with the DFT is that the exact functional for exchange and correlation are not known (except for the free electron gas). Many types of functionals exist, including local, semi-local, gradient dependent, and nonlocal functionals. The most important, widely used approximation for the exchange-correlation energy is the local-density approximation (LDA). For many decades, the LDA has been applied in calculations of band structures and total energies. In the LDA, the exchange-correlation energy is assumed to

depend only on the local electron density in each volume element $d\mathbf{r}$:

$$E_{xc}[n] \approx \int dr n(\mathbf{r}) \epsilon_{\mathbf{xc}}[\mathbf{n}(\mathbf{r})]. \qquad (2.25)$$

ϵ_{xc} is the exchange-correlation energy per electron of a homogeneous electron gas. It is expressed as an analytic function of the electron density, as is the exchange-correlation potential, μ_{xc}. The LDA is known to give less accurate geometries and predicts binding energies significantly too large [22].

Recently, the generalized gradient approximation (GGA) has been considered as a possible improvement over the LDA. The GGA has been found to improve the description of total energies, ionization energies, electron affinities of atoms, and atomization energies of molecules [55, 56]. The generic form of the GGA exchange-correlation energy may be written as

$$E_{xc}^{GGA}[n] = \int dr n(\mathbf{r}) \epsilon_{\mathbf{xc}}^{\mathbf{GGA}} \delta \mathbf{n}(\mathbf{r}) \qquad (2.26)$$

so that it depends locally on the electronic density $n(\mathbf{r})$ and its gradient.

2.2.4. Implementing the DFT. Major computational approaches have limitations, advantages, and disadvantages. One must have a thorough understanding of each methods capabilities and limitations for a better implementation. When choosing any computational approach, as suggested by Wimmer at al. [21], one must asses each computational approach in terms of at least six criteria: capabilities, generality, accuracy, accessible size of systems, accessible time scales, and computational efficiency. When assessed according to these criteria, the DFT have the most desirable characteristics needed for our investigations of complex multicomponent materials.

Because the primary results of the DFT calculations are the electron density, the total energy, and the one-particle wave functions, the important electrical and optical properties we generally investigate can be derived, such as band gaps and

density of states. In terms of its capability, the DFT does not just provide structural properties but also enables the prediction of the electrical and optical properties of materials. Generality of the DFT approach is vast when compared to other approaches (such as Hartree-Fock). As a result, the DFT is applicable to all elements of the periodic table and can be used for a variety of solids [21, 22].

With the inclusion of approximations beyond the LDA, the DFT becomes more superior when compared with other methods, giving a better estimation and more accurate results. One of the primary reasons we implement the DFT approach is its state-of-the-art high accuracy. For example, interatomic equilibrium distances for a great number of bonds can be predicted within approximately 0.02 Å of the experiment. Although the binding energies are overestimated within the LDA, nonlocal approximations improve the accuracy to within 0.1 eV of the experiment. Calculations with the system size in the order of up to 100 atoms is possible with the DFT [21]. The DFT calculations tend to be computationally efficient and do not result in strong deviations from the experiment, depending on the type of materials being investigated, the choice of computational parameters, and the basis functions [21].

Some of the major choices one has to make in a practical Kohn-Sham calculation are illustrated schematically in Fig. 2.1. This figure illustrates a rich spectrum of choices for different applications, geometries and symmetries, chemical elements, and materials requiring different approximations. The solutions of the Khon-Sham equations shown in Figure 2.1 allow one to have access to all the properties that can be derived using the DFT. The system can be defined by the terms inside the brackets. These terms consist of the kinetic energy, the coulomb potential, and the exchange-correlation potential. Every term in the equation plays a major role when making choices for DFT calculations. The role and importance of each term and its relevant significance to our research and the reasoning behind the choices we made for our DFT methods are discussed below.

all-electron full potential*

all-electron muffin-tin

pseudopotential

generalized gradient approx.(GGA)*

sX-LDA*

LDA+U*

self-interaction corrections (SIC)

GW

model GW*

beyond LDA

local density approximation (LDA)*

$$\left[-\frac{1}{2}\nabla^2 + V(r) + \mu_{xc}(r)\right]\Psi_i^k(r) = \varepsilon_i^k \Psi_i^k(r)$$

non-periodic*

periodic*

non-spin-polarized*

spin-polarized*

atomic orbitals

plane waves* (**FLAPW**)

spherical waves
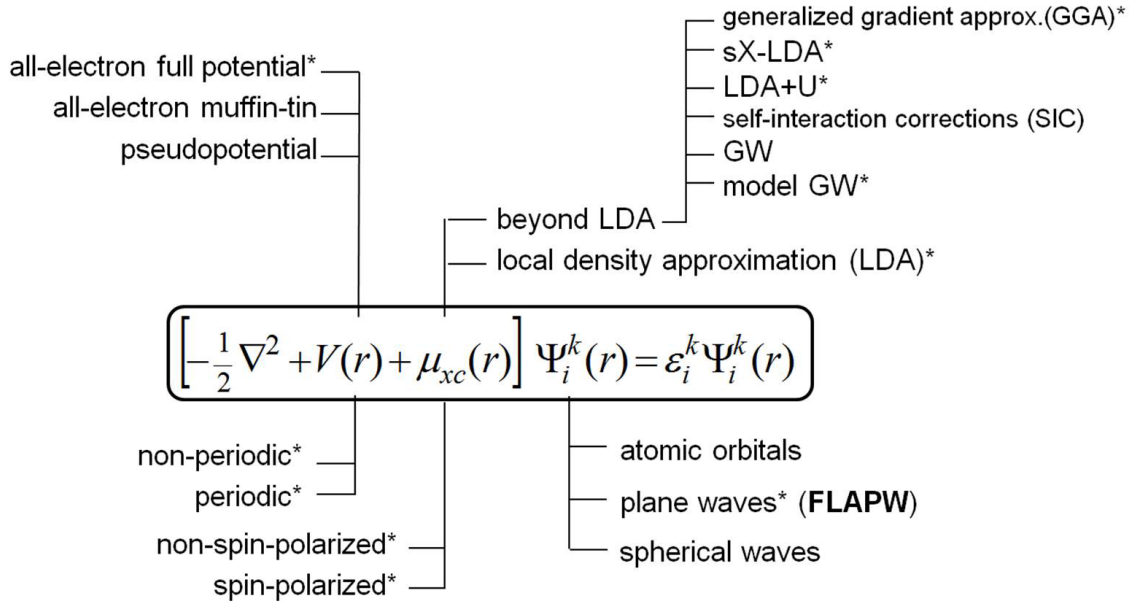
Figure 2.1: Computational choices that one can make based on the Kohn-Sham equations when using DFT methods [21]. The terms inside the brackets are the kinetic energy, the electrostatic potential, and the exchange-correlation potential. Ψ_i is the one electron wave function, where k is the wave vector. A star denotes the existence of the feature in FLAPW method.

The Coulomb potential term defines the chemical and structural properties of the system, offering the choice of calculations for either non-periodic systems or periodic systems. Moreover, one has the choice between all-electron full potential (where the coulomb singularities are considered without shape approximations) and all-electron muffin tin shaped potential (where potential around each atom is assumed to be spherical which generally works well for densely packed systems). Moreover, a choice exists between the different approximations for exchange-correlation potentials. The LDA underestimates the band gaps, as previously mentioned. One can overcome this problem by choosing approximations beyond the LDA, such as GGA or screened-exchange LDA [57, 58]. One of the important choices in Fig. 2.1 is the type of basis set. Generally, the names of DFT methods available are based on the type of basis set. They can be based on the plane waves and can be augmented. The accuracy of

the results from the DFT calculations depend strongly on the choice of both basis set and density functional.

Combinations of particular choices lead to different methods with different capability and limitations. Based on Fig. 2.1, the most desired choices we made that are critical for our first-principles calculations are present in the method known as the full potential linearized augmented plane wave method (FLAPW) [20, 47]. As previously mentioned, this method is named after its basis functions which are linearized augmented plane waves. The choices and the features included in the FLAPW method are considered to be the most accurate. Details regarding the FLAPW method are discussed in the following section.

2.3. FLAPW METHOD

2.3.1. Overview. The full-potential linearized augmented plane wave method (FLAPW) [20, 47], which employs density-functional theory, is considered as one of the most accurate electronic structure calculation schemes. It emerged as a highly-precise state-of-the-art ab-initio technique with a reasonable computational efficiency [48, 59]. This method has its origin in the augmented plane wave (APW) method proposed by Slater [60]. Computationally, the APW method is demanding since the basis functions are energy dependent and the eigenvalue problem is non-linear. An important development was presented by the subsequent linearization of the APW method (LAPW) [61, 62] where the energy dependence was removed by selecting a fixed set of suitable muffin-tin radial functions and their energy derivatives.

In the FLAPW approach, real space is partitioned into spherical regions around atoms and interstitial regions between spheres. In the spherical region, the basis functions are products of radial functions and spherical harmonics. In the interstitial region, plane waves are used. There is no shape approximation for either the charge density or the potential. All electrons are treated in the self-consistent

process. The core electrons are treated fully relativistically and the valence electrons are treated semi-relativistically [63]. Due to its all-electron algorithm, the advantage and power of the FLAPW method is its universal applicability to all atoms of the periodic table. In particular, its applicability to transition metals, rare-earths, and to multi-atomic systems with compact and open structures. Both three-dimensional and two-dimensional periodic boundary conditions can be used [59].

This program affords highly accurate calculations of the electronic structure, the total energy and the forces, for a wide range of materials. The capability of calculating atomic forces exerted on the atoms opens the path to structure optimization. These advantages elevate the FLAPW method as the method of choice for accurate electronic structure calculations for a broad spectrum of applications. Also, it is due to these advantages that we implement the FLAPW method in our investigations of complex multicomponent oxides.

As we mentioned previously, the exact functional for exchange and correlation in DFT are not known. Although, there are many types of functionals exist, the most widely used is the local density approximation (LDA), which is implemented in FLAPW. However, the LDA underestimates the band gap value in semiconductors and insulators. Because the valence and conduction band dispersions are less affected by the LDA feature, a so-called scissors operator is often used to push the conduction band up so that the band gap corresponds to the experimental value.

Moreover, besides the GGA, the screened-exchange LDA method (sX-LDA), recently proposed as an approach to obtain realistic excitation energies and improve band-gaps of insulators and semiconductors, has been implemented in the FLAPW. The sX-LDA method introduces part of the correlation effects in the exchange hole by screening the Hartree-Fock exchange integral. Essentially, the sX-LDA method is designed to find a better energy functional beyond the LDA by modeling the exchange-correlation hole within nonlocal density schemes. The sX-LDA eigenvalues

can describe the discontinuity of the exchange-correlation potential for the band gaps. In addition, it can realize accurate ground-state total energies, ground-state charge densities, and band gaps. The sX-LDA method has been found to yield an improved description of band gaps for semiconductors compared to the LDA and the GGA, hence, it agrees very well with the experiment results [29, 57]. In our work, the sX-LDA method is employed along with the conventional LDA.

2.3.2. FLAPW Method: Features and Demonstrations. The FLAPW method is fully parallelized with high efficiency and good stability. An efficient parallelization of this method by division among the processors of the plane-wave components for each state is demonstrated by Canning et al. [64]. Specific features relevant to our investigations that can be obtained using the FLAPW method include the band structure, density of states, charge density, total energy, formation energy, atomic forces, and the optimized geometry.

Taking ZnO as an example, the whole process of how we implement the FLAPW method, and the importance of relevant input parameters and resulting electronic and optical properties that we obtain are discussed and demonstrated here in detail. ZnO has a wurtzite crystal structure with known experimental lattice parameters of a=3.24 Å and c=5.21 Å as well as with internal parameter of u=0.3817.

The general procedure for our calculations of the properties begins with defining the single input file for the FLAPW method. The options and important input parameters in the FLAPW input file are as follows. The cell can be defined by setting the lattice vectors in terms of either cartesian or internal coordinates. Atomic positions for every atom need to be set with their respective x, y, and z components, whether it is primitive cell or super-cell. For the wurtzite ZnO, there are two zinc and two oxygen atoms in the cell and we input the atomic positions in terms of cartesian coordinates. One can define the input parameters of the cell according to the choice

of calculations between un-doped stoichiometric or doped nonstoichiometric materials. For example, one can investigate the formation of native point defects (such as cation/anion vacancies) or the substitutional doping (such as fluorine substituted in zinc site) in ZnO, by setting the necessary position and atom type in the supercell. In the case of wurtzite ZnO, a 84-atom supercell can be constructed with the lattice vectors $(\bar{2}\,\bar{2}1)$, $(\bar{1}31)$, and $(2\bar{3}1)$, given in the units of hexagonal primitive cell vectors. Due to its translational symmetry, the distances between the oxygen defects are ≈ 10 Å. Thus, the resulting defect concentration is approximately $1.7 \times 10^{21} \text{cm}^{-3}$ which is determined as the number of defect sites divided by the volume of the supercell [43]. After defining the cell accordingly, one important step is to perform geometry optimization. Internal positions can be optimized via total energy and atomic forces minimization such that the atomic positions are relaxed.

General options exist where one can enable necessary variables for desired calculations, including density of states and band structure. For the latter option, the special **k**-points can be provided in a separate file to carry out the $\epsilon(\text{k})$ calculations along the high-symmetry lines in the Brillouin zone. For ZnO calculations, cutoffs for the basis functions were 16.0 Ry. Summations over the Brillouin zone were carried out using 32 special **k**-points in the irreducible wedge. The muffin-tin radius for every different atom in the cell needs to be defined. The muffin-tin radii for ZnO is 2.1 a.u. for Zn and 1.6 a.u. for O atoms, respectively. One can set the mixing and the convergence options in the iterations toward self-consistency. The output charge density is constructed from the eigenvectors and then mixed with the input to yield a refined input for the next iteration. Mixing schemes such as the Broyden scheme [65], can be used. The Broyden scheme uses information from previous iterations to accelerate convergence. The value for convergence of the electron charge density and the maximum number of iterations allowed can be controlled and the program will terminate accordingly if convergence is reached before this value [59]. For example, for ZnO,

we have set the value of convergency to 0.02 e/Bohr^3 and the maximum number of iterations to 80. Typically, convergence is reached within 25 iterations. For un-doped wurtzite ZnO, it takes about 12 iterations to obtain the above convergence. The total energy of the system is obtained at every iteration of the optimization. Based on the total energies, we can obtain a great deal of useful information. Total energies can be used as a comparison tool between different carrier generation mechanisms i.e., calculating and comparing the resultant energies for each doping mechanism, where the corresponding minimum energy obtained is considered as the system of preference for the dopant. In addition, total energies of a system with a defect can be used to calculate the formation energy of the corresponding defect in that system. One can calculate the equilibrium defect concentrations since it depends on the formation energy of the defect, equation 1.3. We note that the properties (such as formation energy, carrier concentration, and conductivity) related to carrier generation in TCO hosts are discussed in great detail in Section 1.4.

Furthermore, band structures and (partial)density of states can be calculated after the geometry optimization by enabling the appropriate features in the input file (as mentioned before). We can obtain a great deal of information about the electronic or optical properties of the material by studying the electronic band structures. Bands in solids allow us to identify the material as either an insulator, a semiconductor, or a metal. Moreover, the width of the band gaps, band edges, and whether the band gaps are direct or indirect can provide useful information. For example, from Figure 2.2, we can tell that the ZnO is a wide band gap insulator with a direct band gap (resulting from metal s and oxygen p interactions) of 1.21 eV. We can also compare and study how the band structure changes for a different doping mechanism in ZnO. When doped, the dispersed parabolic conduction band (with a low density of states) of ZnO would provide a pronounced shift of Fermi level up into the conduction band as well as providing high mobility of electrons and low optical absorption.
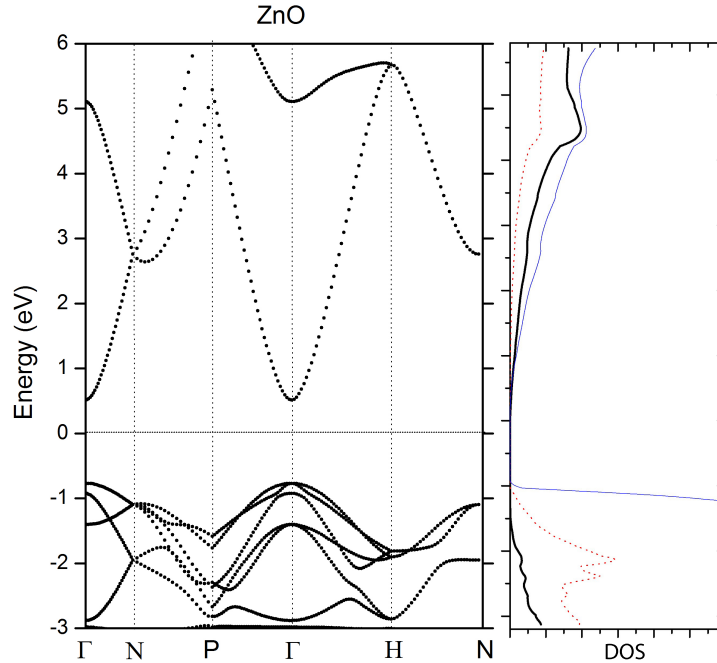
Figure 2.2: Band structure and DOS of un-doped ZnO calculated within the local density approximations (LDA). In the DOS plot, the thick/black, dashed/red and thin/blue lines represent metal s, metal p and oxygen p states, respectively.

Studying the density of states, we can determine which states are contributing to the conduction band or the valence band, which is critical for charge transport. From the partial density of states in Figure 2.2, it can be seen that both oxygen 2p and metal s states have a similar contribution to the conduction band of ZnO. Moreover, we can calculate the electron effective masses m_e, which is $0.35m_e$ and isotropic for ZnO. Finally, we can calculate the electron group velocities and estimate the conductivity factor which is the square of the electron velocity multiplied by the density of states, equation 4.12, within the vicinity of the Fermi level by choosing the specific band of interest.

3. ELECTRONIC PROPERTIES OF LAYERED MULTICOMPONENT WIDE-BAND-GAP OXIDES: A COMBINATORIAL APPROACH

Altynbek Murat[1] and Julia E. Medvedeva[1]

[1]*Department of Physics, Missouri University of Science & Technology,*

Rolla, MO 65409, USA

ABSTRACT[*]

The structural, electronic, and optical properties of 12 multicomponent oxides with layered structure $RAMO_4$, where R^{3+}=In or Sc, A^{3+}=Al or Ga, and M^{2+}=Ca, Cd, Mg, or Zn, are investigated using first-principles density functional approach. The compositional complexity of $RAMO_4$ leads to a wide range of band gap values varying from 2.45 eV for $InGaCdO_4$ to 6.29 eV for $ScAlMgO_4$ as obtained from our self-consistent screened-exchange local density approximation calculations. Strikingly, despite the different band gaps in the oxide constituents, namely, 2-4 eV in CdO, In_2O_3, or ZnO; 5-6 eV for Ga_2O_3 or Sc_2O_3; and 7-9 eV in CaO, MgO, or Al_2O_3, the bottom of the conduction band in the multicomponent oxides is formed from the *s* states of *all* cations and their neighboring oxygen *p* states. We show that the hybrid nature of the conduction band in multicomponent oxides originates from the unusual fivefold atomic coordination of A^{3+} and M^{2+} cations, which enables the interaction between the spatially spread *s* orbitals of adjacent cations via shared oxygen atoms. The effect of the local atomic coordination on the band gap, the electron effective mass, the orbital composition of the conduction band, and the expected (an)isotropic character of the electron transport in layered $RAMO_4$ is thoroughly discussed.

3.1. INTRODUCTION

Transparent conducting oxides (TCOs) are unique materials that exhibit both low optical absorption in the visible region and nearly metallic electrical conductivity. Serving as a contact and a window layer simultaneously, TCOs are a vital part of many optoelectronic devices including solar cells, smart windows, and flat panel displays, and they also find application as heating, antistatic, and optical coatings (for select reviews, see Refs. [1, 5, 6, 25, 66, 67, 68]).

Multicomponent TCOs – complex oxides which contain a combination of post-transition metals, In, Zn, Ga, Cd or Sn, as well as light main-group metals such as Al or Mg – have attracted wide attention due to a possibility to manipulate the optical, electronic, and thermal properties via the chemical composition and, thus, to significantly broaden the application range of TCO materials [1, 5, 6, 26, 31, 32, 68, 69, 70, 71, 72, 73]. To optimize the properties of a multicomponent TCOs, it is critical to understand the role played by each constituent oxide. For example, presence of lighter metals such as Ga, Al or Mg in multicomponent TCOs is attractive for achieving a broader optical transmission window associated with a wider band gap. At the same time, however, these cations are know to be detrimental for the electrical properties as they are believed to significantly suppress carrier concentration and transport.

Recent electronic band structure investigations of several main group metal oxides [15] reveal that the electronic configuration of the cations plays crucial role in the charge transport. It was shown that lighter metal cations (Ga, Ca, Al or Mg) have their empty p or d states near the conduction band bottom. The resulting strong (directional) hybridization of these anisotropic states with the p states of the neighbor oxygen atoms result in significant charge localization (trapping) when extra electrons are introduced. This is in marked contrast to the conventional TCOs, In_2O_3, ZnO, SnO_2, or CdO, where the cation's p states are deep in the conduction band (at about a few eV above the conduction band minimum [15]), and an extra charge is efficiently

transported via a uniform network of the spatially-spread and spherically-symmetric metal s orbitals connected by the oxygen p states.

In a multicomponent oxide containing the cations from both groups, i.e., post-transition metals and light main-group metals, the respective energy locations of the cations' states may not be the same as in single-oxide constituents due to the interaction between different cations via a shared oxygen neighbor. Indeed, it was found [19] that the bottom of the conduction band in $InGaZnO_4$ is governed by the states of *all* cations despite the fact that the band gaps in the corresponding basis oxides differ significantly (2.9 eV for In_2O_3, 3.4 eV for ZnO, and 4.9 eV for Ga_2O_3). Moreover, the electronic properties in a multicomponent oxide may significantly deviate from that expected from the electronic band structures of the single-cation (basis) oxides. This stems from the differences in the interatomic distances and the atomic coordination numbers in the complex oxide as compared to those in the bulk ground-state (lowest energy) structures of the constituent oxides.

In this work, we systematically investigate the structural, electronic and optical properties of 12 $RAMO_4$ compounds with R^{3+}=In or Sc; A^{3+}=Al or Ga; and M^{2+}=Ca, Cd, Mg, or Zn. These materials possess the same layered crystal structure as the member of the homologous series $InGaO_3(ZnO)_m$ [74, 75] with m=1, where the chemically and structurally distinct layers (the octahedrally coordinated $RO_{1.5}$ layer and wurtzite-like $AMO_{2.5}$ double-layer) alternate along the crystallographic z direction. By comparing the calculated electronic properties of the set of multicomponent oxides, we determine how the composition affects (i) the nature of the conduction band bottom; (ii) the electron effective masses in the ab plane (within the layers) and along the z direction (across the layers); and (iii) the location of the cation(s) p states with respect to the conduction band minimum. In addition to the local density approximation (LDA) which underestimates the oxide band gaps and may give incorrect energy location of the states of different cations in the conduction band of

multicomponent materials, we also employed self-consistent screened-exchange LDA (sX-LDA) method which models the exchange-correlation hole within a *nonlocal* density scheme [76].

The paper is organized as follows. First, details of the computational methods and approaches are given in Sec. 3.2. In Sec. 3.3, we discuss the structural peculiarities of the investigated multicomponent compounds and compare them to the structural properties of the basis single-cation oxides. Specifically, we compare the cation-anion distances and the atomic coordination numbers in multicomponent and single-cation oxides in various structures. Further, the electronic properties of the basis, single-cation oxides are discussed in Sec. 3.4. We demonstrate how the electronic properties of the oxides, e.g., band gaps and the electron effective masses, vary upon changes in the interatomic distances and/or oxygen coordination by considering both the ground state and hypothetical structures of oxides. In Sec. 3.5, the general electronic properties of multicomponent oxides are discussed first. Further, we thoroughly analyze the following: (a) how the atomic coordination affects the band gap formation in complex oxides; (b) what is the effect of chemical composition on (an)isotropy of conduction states in $RAMO_4$; (c) what is the orbital composition of the conduction band in $RAMO_4$ and the role the peculiar atomic coordination played in the respective energy location of cation's empty s, p, and d orbitals in the conduction band; and (d) the electron effective masses within and across the structural layers of different composition in $RAMO_4$. We give conclusions in Sec. 3.6.

3.2. METHODS AND APPROXIMATIONS

First-principles full-potential linearized augmented plane wave (FLAPW) [20, 47] method within the local density approximation is employed for the electronic band structure investigations of twelve $RAMO_4$ compounds, R^{3+}=In or Sc, A^{3+}=Al, Ga, M^{2+}=Ca, Cd, Mg, and/or Zn, [11] as well as their single-cation constituents, MgO,

CaO, ZnO, CdO, Sc_2O_3, In_2O_3, Al_2O_3, and Ga_2O_3. Cutoffs for the basis functions, 16.0 Ry, and the potential representation, 81.0 Ry, and expansion in terms of spherical harmonics with $\ell \leq 8$ inside the muffin-tin spheres were used. The muffin-tin radii of multi-cation and single-cation oxides are as follows: 2.3 to 2.6 a.u. for In, Sc, Cd, and Ca; 1.7 to 2.1 a.u. for Ga, Mg, Zn, and Al; and 1.6 to 1.8 a.u. for O atoms. Summations over the Brillouin zone were carried out using at least 23 special **k** points in the irreducible wedge.

Because LDA underestimates the oxide band gaps and may give incorrect energy location of the states of different cations in the conduction band of multi-component materials, we also employed the self-consistent screened-exchange LDA (sX-LDA) method [57, 76, 77, 78, 79] for more accurate description of the band gap values and the valence/conduction band states of the twelve complex oxides. For the sX-LDA calculations, cutoff for the plane wave basis was 10.2 Ry and summations over the Brillouin zone were carried out using at least 14 special **k** points in the irreducible wedge. Ga and Zn $3d^{10}$ states, which were treated as valence, were excluded from screening.

3.3. CRYSTAL STRUCTURE

The investigated multicomponent oxides have rhombohedral $R\bar{3}m$ layered crystal structure of $YbFe_2O_4$ type and belong to the homologous series $RAO_3(MO)_m$ with m=1 [74, 75, 80]. In these compounds, R^{3+} ions (In or Sc) have octahedral coordination with the oxygen atoms and reside in 3(a) position (Yb), whereas both A^{3+} (Al or Ga) and M^{2+} (Ca, Mg, Zn or Cd) ions reside in 6(c) position (Fe) and are distributed randomly [81]. To model a random distribution, specifically, to avoid planes or chains of the same type of atoms, a 49-atom supercell was constructed with the lattice vectors $(30\bar{2})$, $(\bar{1}12)$ and $(02\bar{1})$, given in the units of the rhombohedral primitive cell vectors [36]. Note, that the conventional rhombohedral unit cell of

YbFe$_2$O$_4$ contains 21 atoms (Z=3), and the primitive, i.e., the smallest volume, cell contains 7 atoms (Z=1).

Because of the different ionic radii and the valence state of the cations in RAMO$_4$ compounds, the A^{3+} and M^{2+} atoms have different z component of the internal site position 6(c). Since the exact internal positions of atoms are not known, we used those of the YbFe$_2$O$_4$ [74] as the starting values, and then optimized the internal positions of all atoms in the supercell via minimization of the total energy and the atomic forces. During the optimization the lattice parameters were fixed at the experimental values [11, 74, 75, 80] except for InAlCaO$_4$, InGaCaO$_4$, and InGaCdO$_4$ where a and c were optimized since the experimental values are unavailable. Our optimized structural parameters for the latter compounds as well as the optimized z values for every structure under consideration are given in Table 3.1.

Next, we compare the local atomic structure in multicomponent oxides to that of the constituent basis oxides. First, the following ground state (lowest energy) structures of single-cation oxides were considered: $Fm\bar{3}m$ (rocksalt) for MgO, CaO, and CdO; $Ia\bar{3}$ (bixbyite) for Sc$_2$O$_3$ and In$_2$O$_3$; $P6_3mc$ (wurtzite) for ZnO; $R\bar{3}c$ (corundum) for Al$_2$O$_3$; and $C2/m$ (monoclinic) for β-Ga$_2$O$_3$. For these structures, the lattice parameters were kept at the experimental values. The internal atomic positions for Sc$_2$O$_3$, In$_2$O$_3$, Al$_2$O$_3$, and Ga$_2$O$_3$ were optimized via the total energy and atomic forces minimization. Additional phases for oxides of A and M metals were also calculated as explained in details below.

Our results show that the optimized cation-anion distances in multicomponent oxides correlate with the ionic radii of the cations, c.f., Tables 3.1 and 3.2. For the octahedrally coordinated R^{3+} ions, i.e., In or Sc, the R-O distances in multicomponent oxides are close to those in the corresponding single-cation oxides, c.f., $\langle D_{R-O}\rangle$ in Table 3.1 and $\langle D\rangle$ in Table 3.2. The averaged In-O or Sc-O distance in RAMO$_4$ is only 0.03-0.04 Å larger than that in In$_2$O$_3$ or Sc$_2$O$_3$. The largest deviations for

Table 3.1: Lattice constants a and c, in Å; the range for the fractional z coordinates of A^{3+}=Al or Ga, and M^{2+}=Zn, Cd, Ca, or Mg atoms at the 6(c) positions of rhombohedral $YbFe_2O_4$ structure; and the average optimized cation-anion distances $\langle D_{R-O}\rangle$, the average planar $\langle D^{ab}_{A/M-O}\rangle$, nearest apical $D^c_{A/M-O}$, and next nearest apical distances $D^c_{A/M-O*}$ in Å, for twelve multicomponent oxides. When available, the experimental lattice constants were used (experimental values a, b, c, and d are used from references [11, 74, 75, 80], respectively), otherwise, the lattice parameters were obtained via the geometry optimization. The experimental data for the prototype structure $YbFe_2O_4$ is given for comparison.

$RAMO_4$	a	c	$\langle D_{R-O}\rangle$	$\langle D^{ab}_{A-O}\rangle$	D^c_{A-O}	D^c_{A-O*}	$\langle D^{ab}_{M-O}\rangle$	D^c_{M-O}	D^c_{M-O*}
$InAlCaO_4$	3.34	27.25	2.20	1.77	1.78	2.17	2.20	2.20	2.60
$InAlCdO_4$	3.32^a	27.50^a	2.20	1.78	1.79	2.05	2.17	2.20	2.63
$InAlMgO_4$	3.29^a	25.66^a	2.20	1.83	1.84	2.30	2.02	1.98	2.26
$InAlZnO_4$	3.31^b	26.33^b	2.21	1.84	1.84	2.14	2.05	2.00	2.38
$InGaCaO_4$	3.39	27.31	2.22	1.85	1.86	2.14	2.17	2.21	2.52
$InGaCdO_4$	3.38	27.16	2.21	1.86	1.89	2.31	2.15	2.17	2.61
$InGaMgO_4$	3.30^c	25.81^c	2.19	1.88	1.91	2.35	1.98	1.98	2.26
$InGaZnO_4$	3.29^c	26.07^c	2.21	1.88	1.92	2.35	1.98	1.97	2.38
$ScAlMgO_4$	3.24^a	25.15^a	2.15	1.81	1.80	2.28	1.98	1.98	2.32
$ScAlZnO_4$	3.24^b	25.54^b	2.13	1.82	1.82	2.17	1.99	1.98	2.38
$ScGaMgO_4$	3.27^a	25.62^a	2.14	1.87	1.89	2.32	1.96	1.99	2.33
$ScGaZnO_4$	3.26^c	25.91^c	2.13	1.87	1.90	2.35	1.96	1.98	2.29
$YbFe_2O_4$	3.45^d	25.05^d	2.24	2.01	1.94	2.15			

one of the six In-O distances in the InO_6 octahedra (5-7%) are found for Ca and Cd-containing compounds (i.e., $InGaMO_4$ and $InAlMO_4$ with M=Ca or Cd). These compounds represent the case of a large mismatch of the ionic radii of the A and M ions, which affects the In-O distances in the neighboring $InO_{1.5}$ layer. In other compounds, the In-O distances differ by only 1-2% as compared to those in the bulk In_2O_3.

The most important observation concerning the crystal structure in $RAMO_4$ compounds is that all A and M atoms are in fivefold coordination (bipyramid) with

Table 3.2: The cation-anion distances average, $\langle D \rangle$, and their ranges, in Å in single-cation oxides as compared to the corresponding average cation-anion distances and ranges in multicomponent oxides. Also, the deviation in the ranges of distances in multicomponent oxides with respect to the distances in the corresponding single-cation oxide, in percent.

		Basis oxide		RAMO$_4$		
		$\langle D \rangle$	Range	$\langle D \rangle$	Range	Deviation, %
R$_2$O$_3$	In–O	2.17	2.12-2.21	2.21	2.13-2.37	—/+7
	Sc–O	2.11	2.08-2.16	2.14	2.05-2.22	–1/+3
A$_2$O$_3$	Al–O	1.91	1.86-1.97	1.85	1.71-2.30	–8/+17
	Ga–O	1.93	1.83-2.07	1.93	1.79-2.35	–2/+14
MO	Zn–O	1.98	1.97-1.99	2.02	1.92-2.38	–3/+20
	Mg–O	2.08	2.08	2.04	1.92-2.33	–8/+12
	Ca–O	2.37	2.37	2.25	2.10-2.59	–11/+9
	Cd–O	2.35	2.35	2.38	2.09-2.63	–11/+12

oxygen atoms, Fig. 3.1, and not in fourfold (tetrahedral) as it was previously assumed for decades. As one can see from Table 3.1, the A-O or M-O distance to the fifth atom (also called the second apical atom hereafter), denoted as $\langle D^c_{A/M-O*} \rangle$, is only $\sim$0.3-0.5 Å longer than the distance to the nearest apical oxygen atom, denoted as $\langle D^c_{A/M-O} \rangle$. For comparison, in wurtzite ZnO, the Zn-O distance to the next nearest oxygen atom (second apical O) is 3.22 Å which is 1.23 Å longer than the Zn-O distance to the nearest apical oxygen atom which belongs to the ZnO$_4$ tetrahedra, Fig. 3.2(a).

The fact that Zn has fivefold oxygen coordination in RAZnO$_4$ is illustrated in Fig. 3.3 where we compare the calculated charge density distribution for InGaZnO$_4$ and wurtzite ZnO plotted in the (011) plane to include O-Zn-O bonds along the [0001] direction for both compounds. The strong bonding between Zn (as well as Ga)
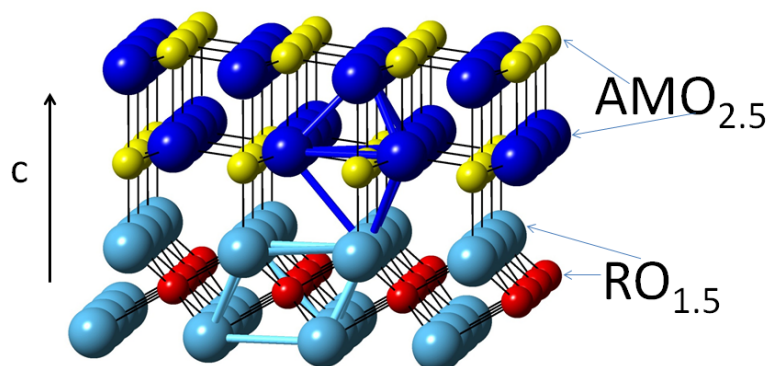
Figure 3.1: (Color online)Oxygen coordination of R=In or Sc (octahedra) and A=Al or Ga, and M=Zn, Cd, Ca, or Mg (bipyramid) in the single block of the unit cell of $RAMO_4$ compounds. The conventional unit cell of $RAMO_4$ consists of three similar blocks stacked along the c direction.
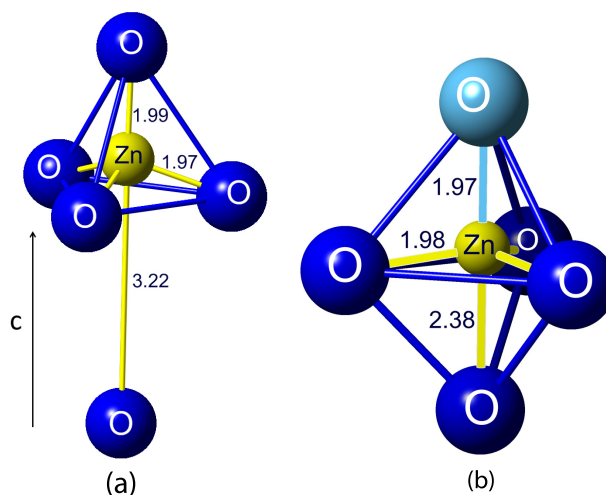
Figure 3.2: (Color online)Fourfold vs fivefold coordination of Zn with oxygen atoms in wurtzite ZnO (a) vs $InGaZnO_4$ (b). The cation-anion apical and planar distances are shown (in Å). The corresponding charge densities are shown in Fig. 3.3.
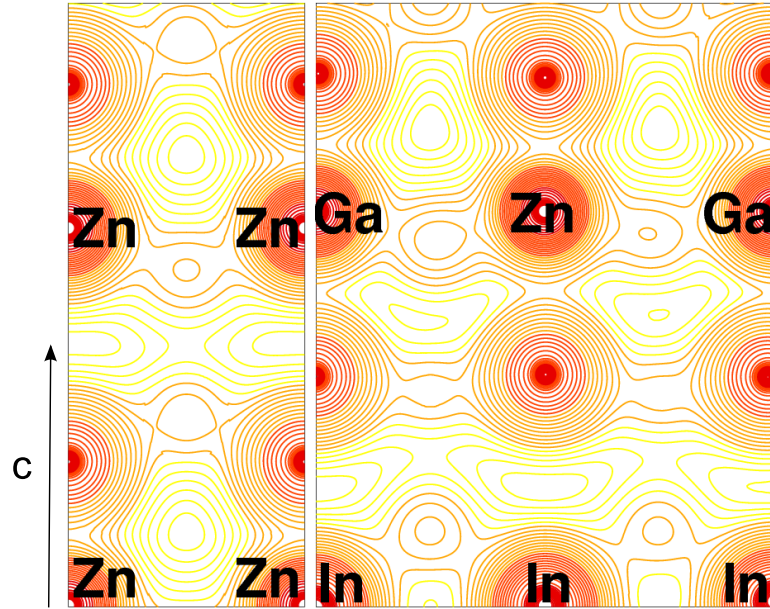
Figure 3.3: (Color online)Calculated total charge density distribution contour plots for wurtzite ZnO [left-(a)] and InGaZnO$_4$ [right-(b)]. Zn as well as Ga have strong bonds with both apical oxygen atoms making them fivefold coordinated cations in the multicomponent oxide, in marked contrast to wurtzite ZnO with fourfold oxygen coordination.

atom and the second apical oxygen atom in the multicomponent oxide is clearly seen from the charge density plot, Fig. 3.3(b). In contrast, there is no overlap between Zn atom and its second apical oxygen atom in wurtzite ZnO, Fig. 3.3(a). Thus, Zn atoms form five bonds with neighboring oxygen atoms in InGaZnO$_4$, whereas Zn has four bonds in the basis ZnO.

Similar to Zn, all other M^{2+} and all A^{3+} cations in RAMO$_4$ compounds are fivefold coordinated with oxygen atoms. Strikingly, none of the A or M atoms possess fivefold coordination in the basis, single-cation oxides. The Ca, Cd, or Mg metals form rocksalt structure ($Fm\bar{3}m$) with octahedral oxygen coordination, whereas Al or Ga ions are in either fourfold or sixfold coordinations in corundum ($R\bar{3}c$) or monoclinic ($C2/m$) phases, respectively. (Other known phases of Al$_2$O$_3$, i.e., θ- and κ-Al$_2$O$_3$ with $C2/m$ and $Pna2_1$ structures, respectively, also have four- and six-coordinated

Al ions; α-Ga_2O_3 has corundum structure, space group $R\bar{3}c$, with sixfold oxygen coordination of Ga.)

The unusual fivefold coordination of A and M ions stabilized in $RAMO_4$ compounds is expected to manifest itself in the electronic properties of the complex oxides that differ from those for the basis oxides. Specifically, because the main features of the electronic band structure of oxides, such as the band gap value and the electron effective mass, are determined by the strong metal-oxygen interactions, direct comparison between the (averaged) values obtained for multicomponent oxides with those in the basis oxides in the ground state structures is invalid.

We stress here that the fivefold coordination of A and M atoms with the neighbor O atoms in the $RAMO_4$ compounds does not fall out of the fundamental principles governing the structure formation of multicomponent oxide systems. As shown in the extensive works of Walsh et al. [31] (and references therein), the coordination environment is determined by satisfying the electronic octet rule for local charge neutrality as well as the material stoichiometry. The octahedral structure in the $RO_{1.5}$ layer which maximizes the atomic separation between the negatively charged O atoms, serves as a disruptive stacking fault to the wurtzite-like $AMO_{2.5}$ layer. At the same time, the A atoms, such as Al or Ga, do not have a strong preference for octahedral sites [31]. Hence, while trying to accommodate the A and M atoms and obey the electronic octet rule, changes must occur in the $AMO_{2.5}$ layer leading to the formation of fivefold trigonal bipyramid structures [31].

To determine how the local atomic coordination affects the electronic properties of oxides, we performed calculations for the hypothetical phases with fivefold oxygen coordination of A and M cations. Moreover, we set the lattice parameters as well as the internal atomic positions in the hypothetical phases so that the metal-oxygen distances are similar to those in the corresponding multicomponent $RAMO_4$ oxides (given in Table 3.1). This will allow us to compare the band gap value calculated for

each RAMO$_4$ compound with the value obtained via averaging over the band gaps in the corresponding single-cation oxides with the same local atomic coordination and bond-lengths. For ZnO, MgO, CdO, and MgO, i.e., for $M^{2+}O^{2-}$ compounds, we performed calculations for wurtzite-based structures where the second nearest apical oxygen atom is located close enough to the metal ion to make it a fivefold coordination, Table 3.3. Similarly, for Al_2O_3 and Ga_2O_3, we used Al_2S_3-type structure, space group $P6_1$, and modified the lattice parameters and the internal atomic positions to obtain A-O distances similar to those in the corresponding RAlMO$_4$ or RGaMO$_4$ compounds, Table 3.4. Note, that the In and Sc are octahedrally coordinated with oxygen atoms both in the basis oxides and in RAMO$_4$. The In-O or Sc-O distances in the multicomponent oxides are slightly larger than those in the basis oxides, c.f., Tables 3.1 and 3.2.

Table 3.3: Structural parameters for wurtzite-based hypothetical structures of $M^{2+}O^{2-}$ where metal-oxygen distances correspond to the average distances obtained for RAMO$_4$, Table 3.1. Lattice constants a and c, internal paramater u in Å, as well as planar D^{ab}_{M-O}, nearest apical D^c_{M-O}, and next nearest apical distances D^c_{M-O*} in Å. To compare, in ground state wurtzite ZnO, a=3.25 Å, c=5.21 Å, u=0.3817: D^{ab}_{Zn-O}=1.97 Å; D^c_{Zn-O}=1.99 Å; D^c_{Zn-O*}=3.22 Å.

	a	c	u	D^{ab}_{M-O}	D^c_{M-O}	D^c_{M-O*}
ZnO	3.44	4.34	0.4570	2.00	1.98	2.36
MgO	3.43	4.28	0.4639	1.98	1.98	2.29
CaO	3.77	4.76	0.4625	2.19	2.20	2.56
CdO	3.73	4.81	0.4557	2.16	2.19	2.62

In the next section, we begin our discussions with the electronic properties of single-cation oxides and how the atomic coordination affects their electronic band structure.

Table 3.4: Structural parameters for hypothetical phases of Al_2O_3 and Ga_2O_3 in Al_2S_3-type (space group $P6_1$). The Ga-O and Al-O distances correspond to the average distances obtained in RAMO$_4$. Lattice constants a and c in Å, planar D^{ab}_{A-O}, nearest apical D^c_{A-O}, and next nearest apical distances D^c_{A-O*} in Å for different sites.

	a	c	D^{ab}_{A-O}				D^c_{A-O}	D^c_{A-O*}
Al_2O_3	5.30	12.59	Al(1)	1.78	1.81	1.82	1.79	2.30
			Al(2)	1.79	1.85	1.89	1.83	2.31
Ga_2O_3	5.38	12.85	Ga(1)	1.80	1.83	1.85	1.89	2.35
			Ga(2)	1.82	1.88	1.92	1.87	2.38

3.4. ELECTRONIC PROPERTIES OF SINGLE-CATION OXIDES

3.4.1. Ground State Structures. The investigated basis oxides of post-transition and light main-group metals possess qualitatively similar electronic band structure: the valence band is formed from non-bonding and bonding $2p$ states of oxygen, whereas the highly dispersed conduction band arises from the metal s states and the anti-bonding O-$2p$ states. Strong metal-oxygen interaction is responsible for wide band gaps and small electron effective masses in these oxides, Table 3.5. Note that, as expected, LDA underestimates the band gap values as well as the electron effective masses. The nonlocal density scheme of the sX-LDA method corrects the LDA failure and gives an excellent agreement between the calculated, Table 3.5, and experimental band gaps for both the semiconductor-like materials with band gap of ~2.3-3.4 eV (CdO, In_2O_3, ZnO) and the insulators with band gaps of ~6-9 eV (CaO, MgO, Al_2O_3, Sc_2O_3).

The sX-LDA calculated electronic band structures and partial density of states of all single-cation oxides studied in this work have been published earlier, [15, 19] except for Sc_2O_3. The bottom of the conduction band in scandium oxide is governed

Table 3.5: The averaged electron effective mass in m_e, for single-cation oxides within both LDA and sX-LDA are given for the basis oxides in the ground state phase, $\langle m^g \rangle$, and in the hypothetical phase, $\langle m^h \rangle$. The effective mass anisotropy δ, which is defined as $\delta = (m^{[100]} + m^{[010]})/2m^{[001]}$. Also, the band gap values (in eV) obtained within both LDA and sX-LDA are given for the basis oxides in the ground state phase, E_g^g, and in the hypothetical phase, E_g^h, with the bond lengths and oxygen coordination resembling those in the corresponding $RAMO_4$ compounds. The fundamental band gaps as well as optical, i.e., direct, band gaps (in parenthesis) are given.

		LDA				sX-LDA			
		$\langle m^g \rangle$	δ	E_g^g	E_g^h	$\langle m^g \rangle$	E_g^g	$\langle m^h \rangle$	E_g^h
R_2O_3	In_2O_3	0.18	1.00	1.16	0.85	0.28	2.90(3.38)	0.28	2.61(3.07)
	Sc_2O_3	1.12	1.00	3.66	3.61	1.19	6.06	1.19	5.98
A_2O_3	Al_2O_3	0.39	1.00	6.27	3.86	0.45	9.08	0.52	6.80
	Ga_2O_3	0.26	1.17	2.32	2.42	0.34	4.86(4.91)	0.43	4.82
MO	ZnO	0.17	1.09	0.81	1.14	0.35	3.41	0.36	3.63
	MgO	0.38	1.00	4.76	3.44	0.46	7.55	0.52	6.50
	CaO	0.37	1.00	3.45(4.42)	3.52	0.42	5.95(7.15)	0.53	6.51
	CdO	0.15	1.00	-0.51(0.92)	0.00	0.23	0.50(2.29)	0.31	1.01

by the localized Sc d states, Fig. 3.4, and, as a result of the low dispersion of the conduction band, the electron effective mass in Sc_2O_3 is the largest among the oxides and is greater than the mass of the free electron, Table 3.5.

Recent comparative investigations of main group metal oxides [15, 19] have revealed that the fundamental differences in the electronic properties of the conventional TCO hosts (In_2O_3, ZnO and CdO) and the light metal oxides (Al_2O_3, CaO and MgO) originate from the different energy location of the cation's empty p or d states with respect to the conduction band bottom. In the former oxides, the cation p band is well above its s band, which is a prerogative for a good charge transport via a uniform network formed by the spherically symmetric metal s orbitals and the
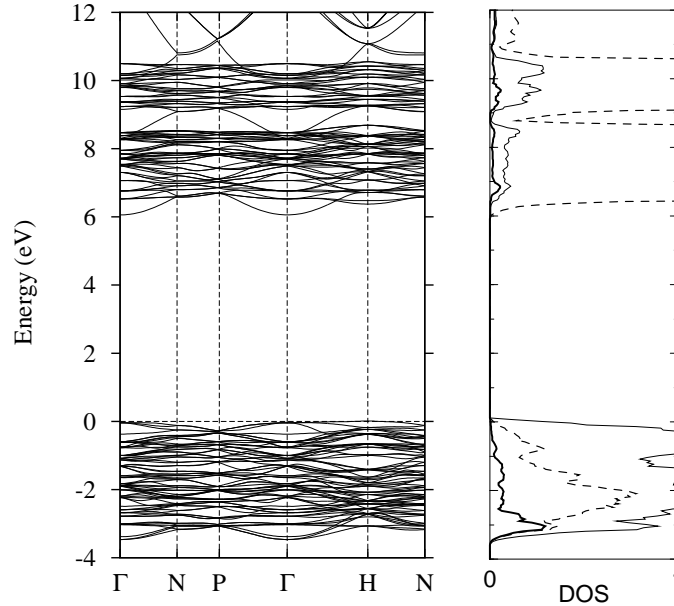
Figure 3.4: Band structure and partial DOS of Sc_2O_3. The thin, dashed, and thick lines in the partial DOS plots represent the metal d, oxygen p, and metal s states, respectively.

neighboring oxygen p orbitals in degenerately doped materials. In striking contrast to the post-transition metal oxides, the light metal p or d band almost coincides (as in Al_2O_3 or MgO) or is even below its s band (as in CaO or Sc_2O_3) in the classical insulators. The proximity of the p or d states to the bottom of the conduction band and the resulting strong directional interaction of these anisotropic orbitals with the p orbitals of the neighboring oxygen atoms have three consequences: (1) wide band gaps of 6-9 eV; (2) the electron effective masses which are at least twice larger than those in the conventional TCO hosts, Table 3.5; and (3) charge localization (widely known as an F center or color center) of extra electrons near an electron-donor defect. The deep defect states are unable to produce electrical conductivity in these oxides.

We note here that Ga_2O_3 does not belong to either of the two groups of oxides, but rather represents an intermediate case, c.f., Table 3.5, illustrating that, naturally, the transition between the oxide groups is not abrupt. The Ga p band is located relatively close to the metal s band but does not coincide with it as, for example,

in Al_2O_3 or MgO. This leads to a considerable but not dominant contributions from the Ga p states near the bottom of the conduction band. Consequently, in oxygen deficient Ga_2O_3, extra electrons induced by the oxygen vacancy are not fully localized near the defect as in light metal oxides, yet, the electron group velocity is nearly an order of magnitude smaller than that in TCOs, e.g., In_2O_3 [19]. This explains why Ga_2O_3 is not a viable TCO itself, nonetheless, Ga-containing multicomponent TCOs are common.

In Sec. 3.5.2, we will come back to the discussion of the proximity of the cation's p or d states to the conduction band in multicomponent oxides.

3.4.2. Hypothetical Phases With Fivefold Coordination. As mentioned above, the main features in the electronic band structure of oxides are determined by the nature and degree of the metal-oxygen interaction. Here we discuss how the electronic properties, in particular, the band gap values of single-cation oxides vary when the metal-oxygen distances and oxygen coordination are changed to resemble those in the $RAMO_4$ multicomponent oxides.

First, we note that In and Sc are octahedrally coordinated with oxygen atoms both in the basis oxides and in $RAMO_4$. The In-O or Sc-O distances in the basis oxides are slightly smaller than those in the multicomponent oxides, c.f., Tables 3.1 and 3.2. To reproduce the R-O distances found in the multicomponent oxides, we increased the lattice parameter a from 10.12 to 10.26 Å and from 9.81 to 9.90 Å for cubic In_2O_3 and Sc_2O_3, respectively. As expected from a smaller nearest neighbor orbital overlap associated with longer metal-oxygen distances, we obtained smaller band gaps for indium and scandium oxides, cf., Table 3.5.

For A_2O_3 and MO oxides, we considered hypothetical structures with fivefold coordination and metal-oxygen distances that resemble those obtained in multicomponent oxides (see Sec. 3.3 for details). The band gap values calculated within both LDA and sX-LDA methods for the hypothetical structures are given in Table 3.5.

For Al_2O_3 and MgO with fivefold-coordinated Al and Mg cations, the gap becomes smaller by 2.2 eV and 1.0 eV, respectively, as compared to the ground state phases (corundum and rocksalt, respectively) with sixfold coordination. In the hypothetical CaO and CdO with fivefold coordinated Ca and Cd, the band gap becomes direct and its value decreases by 0.6 eV and 1.3 eV, respectively, as compared to the optical, direct band gap of rocksalt CaO and CdO with octahedral coordination of cations, Tabel 3.5. (Note, the case of Cd represents the largest coordination-induced change in the band gap, namely, 56%). Accordingly, the band gap in hypothetical ZnO with fivefold coordinated Zn slightly increases (by $\sim$0.2 eV) with respect to four-coordinated Zn in wurtzite ZnO. Finally, there is a negligible change in the band gap of β-Ga_2O_3 which has fourfold and sixfold coordinated Ga atoms in the ground state monoclinic phase as opposed to the fivefold coordination of Ga in the hypothetical Al_2S_3-type structure.

Thus, we find that lower coordination number leads to a smaller band gap. We must stress here that this conclusion should not be generalized to other coordinations. For example, we do not expect the band gap to increase further for structures with 8fold coordination (e.g., as in CsCl-type structure) with respect to the sixfold coordination. We believe that octahedral coordination provides a largest band gap because it corresponds to the largest overlap between the metal orbitals and the p_x, p_y, and p_z orbitals of the neighboring oxygen atoms [15]. Therefore, with respect to the sixfold-coordinated case, higher- and lower-coordinated structures are expected to produce a smaller band gap. Variations in the metal-oxygen distances (c.f., ranges in Table 3.2) may further affect the orbital overlap and, hence, the band gap values, but perhaps to a lesser extent compared to the changes caused by the different atomic coordination.

In the next section, we will demonstrate that the band gap values of multi-component $RAMO_4$ compounds can be reproduced via averaging over those obtained

for the single-cation oxides in the hypothetical structures, i.e., with the corresponding atomic coordination and interatomic distances.

3.5. ELECTRONIC PROPERTIES OF MULTICOMPONENT OXIDES

3.5.1. Role of Atomic Coordination in Band Gap Formation. The electronic band structure of 12 multicomponent oxides, $RAMO_4$, is similar to that of the single-cation oxides: the valence band is formed from the oxygen $2p$ states, whereas the conduction band arises from the antibonding oxygen $2p$ states and the metal s, p or d states(see Figs. 3.5 and 3.6).

The average width of the valence band is about 6.4 eV for all compounds with the largest value of 7.5 eV obtained for $ScGaZnO_4$. In the valence band, both types of the oxygen atoms, O(1) and O(2), give comparable contributions. However, at the very top of the valence band, the contributions from O(2), i.e., the oxygen that belongs to the $AMO_{2.5}$ double layer, are at least two times larger except for $ScAlMgO_4$ and $ScGaMgO_4$ where the oxygen contributions are similar.

Metal-oxygen interactions result in a band gap between the valence and the conduction bands which varies significantly with composition. From the sX-LDA calculations, the smallest gap of 2.45 eV is found for $InGaCdO_4$, and the largest, 6.29 eV, for $ScAlMgO_4$, Table 3.6. We note that independent of the composition of the complex oxides, the sX-LDA band gap values are larger by about 2 eV (more precisely, by 1.7–2.5 eV) than the LDA values for all compounds investigated, Table 3.6.

The band gaps of multicomponent oxides seem to follow the general trend expected from the band gap values of the basis oxide constituents, i.e., the incorporation of ligher metals results in a band gap increase. However, the increase is not the same in otherwise similar compounds: for example, when Ga is replaced by Al in $InAMO_4$ compounds, the gap does not increase by the same amount for the four compounds,
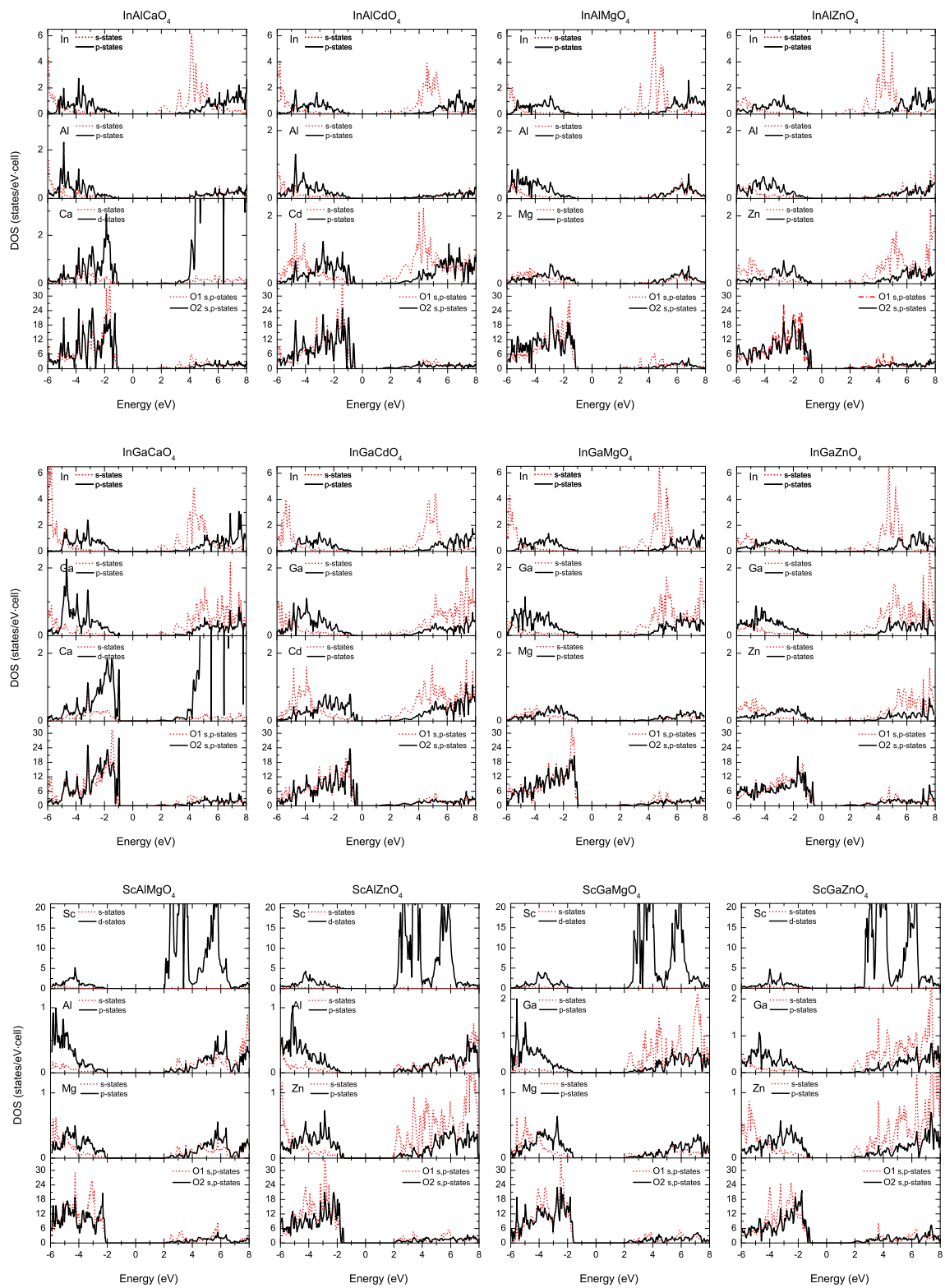
Figure 3.5: (Color online)Partial density of states in multicomponent RAMO$_4$ compounds as obtained from LDA calculations.
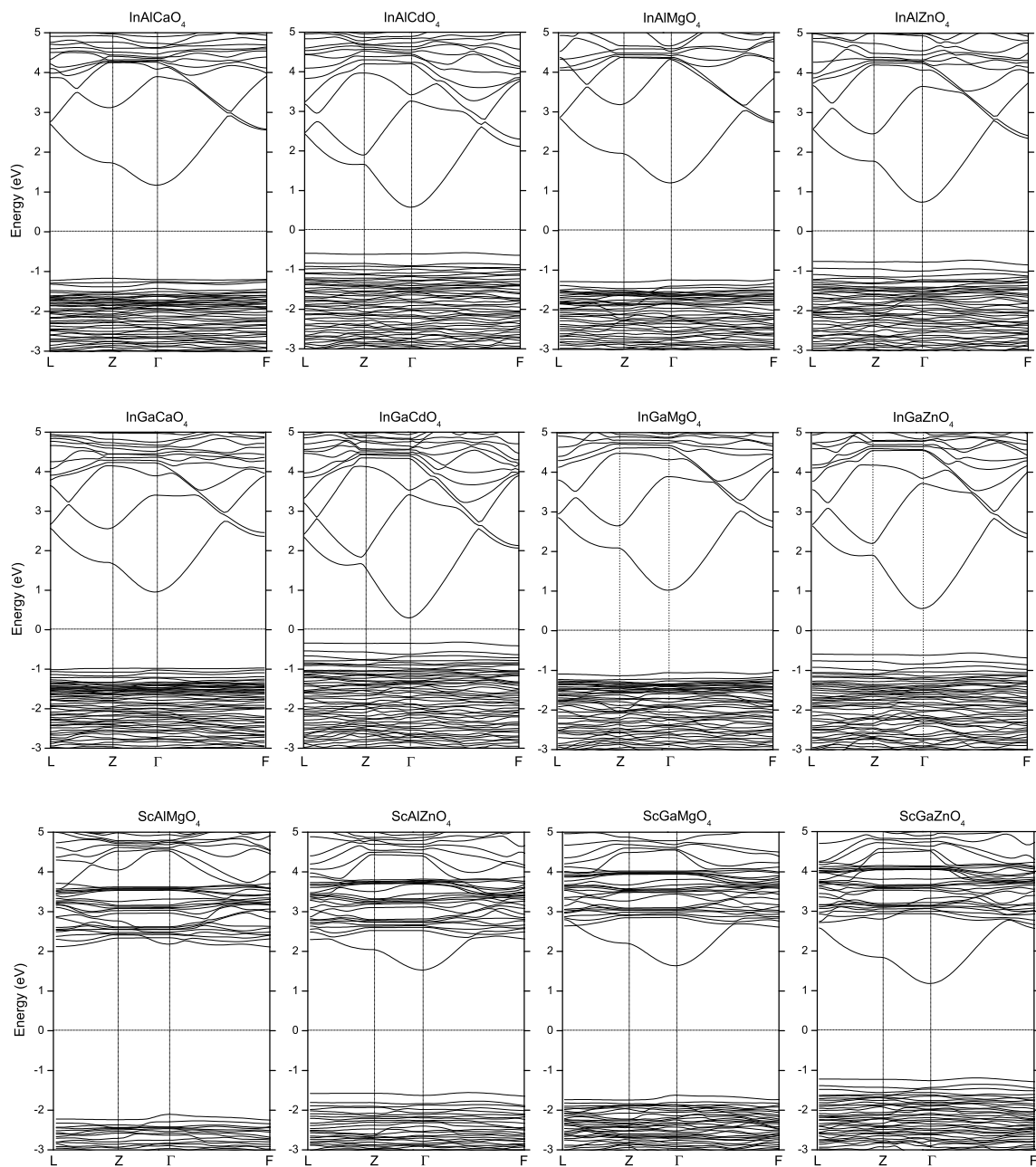
Figure 3.6: Electronic band structure of 12 multicomponent $RAMO_4$ compounds as obtained from LDA calculations.

Table 3.6: LDA and sX-LDA calculated band gaps E_g (in eV) in $RAMO_4$ compounds and the band gap averages obtained using the band gaps of the corresponding single-cation oxides in the ground state, $\langle E_g^g \rangle$, or the hypothetical phases, $\langle E_g^h \rangle$, cf., Table 3.5, with equal weights. In addition, weighted averages, $\langle E_g^g \rangle^w$ and $\langle E_g^h \rangle^w$, calculated based on the respective contributions of the cations to the bottom of the conduction band, Fig. 3.7, are given.

	LDA					sX-LDA				
$RAMO_4$	E_g	$\langle E_g^g \rangle$	$\langle E_g^g \rangle^w$	$\langle E_g^h \rangle$	$\langle E_g^h \rangle^w$	E_g	$\langle E_g^g \rangle$	$\langle E_g^g \rangle^w$	$\langle E_g^h \rangle$	$\langle E_g^h \rangle^w$
$InAlZnO_4$	1.51	2.75	2.41	1.95	1.73	3.48	5.13	4.68	4.35	4.01
$InAlCaO_4$	2.37	3.63	3.02	2.74	2.21	4.87	5.98	5.21	5.31	4.54
$InAlMgO_4$	2.45	4.06	3.20	2.72	2.15	4.62	6.51	5.43	5.30	4.47
$InAlCdO_4$	1.18	2.31	1.88	1.57	1.32	2.87	4.16	3.62	3.47	3.11
$InGaZnO_4$	1.18	1.43	1.41	1.47	1.43	3.29	3.72	3.67	3.69	3.62
$InGaCaO_4$	1.93	2.31	2.10	2.26	2.02	4.08	4.57	4.28	4.65	4.29
$InGaMgO_4$	2.08	2.75	2.54	2.24	2.07	4.31	5.10	4.83	4.64	4.40
$InGaCdO_4$	0.64	0.99	0.85	1.09	0.99	2.45	2.75	2.54	2.81	2.65
$ScGaZnO_4$	2.44	2.26	1.93	2.39	2.10	4.45	4.78	4.47	4.81	4.53
$ScAlZnO_4$	3.16	3.58	3.00	2.87	2.49	5.52	6.18	5.61	5.47	5.08
$ScGaMgO_4$	3.26	3.58	3.55	3.16	3.09	5.76	6.16	6.15	5.77	5.73
$ScAlMgO_4$	4.35	4.90	4.12	3.64	3.64	6.29	7.56	6.60	6.43	6.13

i.e., those with M=Zn, Ca, Mg, or Cd. Rather, the increase is about 0.2 eV, 0.8 eV, 0.3 eV, or 0.4 eV, respectively, Table 3.6, as obtained within sX-LDA calculations. A thorough analysis of the obtained trends in the band gap values and a comparison with those in the corresponding basis oxides allow us to make the following important conclusions:

(i) The band gap in a multicomponent oxide is not governed by the smallest-gap basis oxide constituent. For example, for two Cd-containing complex oxides, the sX-LDA band gaps are 2.5 eV and 2.9 eV which are larger than the CdO band gap,

Table 3.5. For InAMO$_4$ compounds excluding those with Cd, the band gap values vary from 3.3 eV to 4.9 eV, Table 3.6 – despite the fact that In$_2$O$_3$ has the band gap of 2.90 eV (from sX-LDA), Table 3.5.

(ii) The band gap in the multicomponent oxides is affected by the presence of *all* oxide constituents disregarding the differences in the band gaps of the basis oxides. In other words, not only the post-transition metal oxides (smaller-gap constituents) but also the light metal oxides (large-gap constituents) contribute to the formation of the band gap (for example, compare the band gaps of InGaMO$_4$ with M=Cd, Zn, Ca or Mg, or other sets of compounds). This arises from the close interaction between the alternating cations via shared oxygen atoms in mixed A and M or neighbor R-layers, and points to a hybrid nature of the conduction band, as discussed in the next section.

(iii) An equal-weight average, $\langle E_g^g \rangle$, over the band gaps of the basis oxides in their ground state phases (c.f., Table 3.5) correlates with the calculated band gaps for corresponding multicomponent oxides but gives significantly overestimated values in most cases, Table 3.6.

(iv) An equal-weight average, $\langle E_g^h \rangle$, over the band gaps of the basis oxides in the hypothetical phases (c.f., Table 3.5) provides a better guess but still overestimates the value of the band gap in multicomponent oxides, Table 3.6.

(v) Weighted average over the band gaps of the basis oxides (in either the ground state phase or the hypothetical phase) with weights taken as the percent contributions from the cations states to the lowest conduction band wave-function at the Γ point yields underestimated band gap values with respect to those calculated for multicomponent oxides (these values are not given in the Table 3.6). For the RAMO$_4$ compounds with two or more light metal oxide constituents, the underestimation is significant, of $\sim 30\%$. This suggests that the states located above the conduction

band minimum (such as the states of the light metals) play an important role and must be taken into account.

(vi) Weighted average, $\langle E_g^h \rangle^w$, over the band gaps of the basis oxides in the hypothetical phase with weights taken as the relative cation contributions to the conduction band within an energy range, Fig. 3.7, provides a closest match to the calculated band gap values in multicomponent oxides, Table 3.6. The energy range at the bottom of the conduction band which is used to determine the cations contributions, represents the Fermi energy displacement, or the so-called Burstein-Moss (BM) shift, which corresponds to an extra electron concentration of 1×10^{21} cm^{-3} in each compound. Due to the high energy dispersion of the conduction band in InAMO$_4$ compounds, the BM shift is large, of 1.0-1.5 eV. In ScAMO$_4$, the presence of the Sc d states near the bottom of the conduction band result in a high density of states, and hence, the BM shift is significantly smaller, e.g., 0.05 eV for ScAlMgO$_4$ and $\sim$0.7 eV for ScAlZnO$_4$ and ScGaMgO$_4$. Thus, the local atomic structure in multicomponent
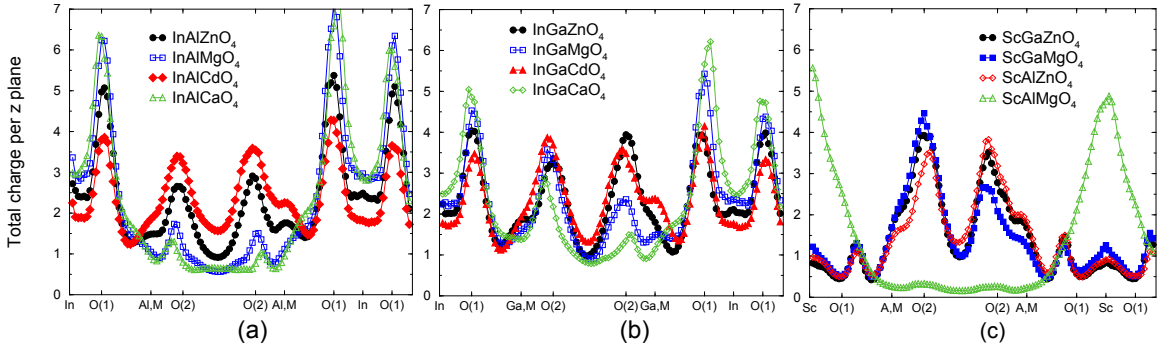
Figure 3.7: (Color online) Total charge densities calculated within one unit cell and at the bottom of the conduction band for the energy window that represents $\sim$1x10^{21} cm^{-3} extra electrons in each RAMO$_4$.

oxides, which differs from that of the basis oxides in the ground state (see Secs. 3.3 and 3.4), plays an important role in determining the resulting electronic properties and must be taken into account for accurate predictions. We note here that an improved agreement between the calculated and the averaged band gaps is expected when the metal-oxygen distances in the hypothetical oxide phases closely correspond

to the distances in particular multicomponent oxide, Table 3.1. In our calculations for the hypothetical single-cation phases, we used the metal-oxygen distances averaged over all RAMO$_4$ for each particular metal, $\langle D \rangle$ in Table 3.2, while the actual distances in each RAMO$_4$ may differ essentially, c.f., deviations of the ranges in Table 3.2. For example, the 15 % overestimation of the band gap average in InAlZnO$_4$ is due to the fact that the Al-O and Zn-O distances in this compound, $\langle D_{Zn-O}^{ab} \rangle = 2.05$ Å, $\langle D_{Zn-O}^{c} \rangle = 2.00$ Å, $\langle D_{Al-O}^{ab} \rangle = 1.84$ Å and $\langle D_{Al-O}^{c} \rangle = 1.84$ Å, Table 3.1, are larger than those in the hypothetical ZnO phase, $\langle D_{Al-O}^{ab} \rangle = 2.00$ Å and $\langle D_{Zn-O}^{c} \rangle = 1.98$ Å, Table 3.3, and the hypothetical $P6_1$ phase of Al$_2$O$_3$, $\langle D_{Al-O}^{ab} \rangle = 1.825$ Å and $\langle D_{Al-O}^{c} \rangle = 1.81$ Å, Table 3.4. Increased distances in the hypothetical oxide phases will result in smaller band gaps for these compounds, bringing the average band gap closer to the calculated one in InAlZnO$_4$. Conversely, the 7% underestimation of the band gap average in InAlCaO$_4$ is due to the smaller Al-O distances in the multicomponent oxide ($\langle D_{Al-O}^{ab} \rangle = 1.77$ Å and $\langle D_{Al-O}^{c} \rangle = 1.78$ Å, Table 3.1) as compared to those in the hypothetical Al$_2$O$_3$, Table 3.4.

3.5.2. Nature of the Conduction Band in RAMO$_4$. The nature of the conduction band in a complex TCO host is of primary interest since the charge transport in degenerately doped material will occur through the states which form the conduction band. One of the reasons that the oxides of homologues series (In,Ga)$_2$O$_3$(ZnO)$_m$, m=integer, have attracted wide attention was a common assumption that the conduction band in these complex oxides is formed from the In s states. Based on this assumption it was suggested that these layered materials offer a possibility to spatially separate carrier donors located within non-conducting layers and the conducting layers which transfer the carriers effectively, i.e., without charge scattering on the impurities, that would lead to an increased conductivity [72].

From the density of states (DOS) plots, c.f., Fig. 3.5, it may appear that the In states solely govern the conduction band in all InAMO$_4$ compounds. However,

analysis of the DOS plots alone may provide a misleading picture of the nature of the conduction bands for three reasons. First, due to the high energy dispersion at the bottom of the conduction band in the oxides under consideration, the corresponding density of states is small. This tail in the DOS should not be neglected. Second, one should compare the relative contributions from different atoms within a rather narrow energy range at the bottom of the conduction band which corresponds to a Fermi level displacement associated with introduction of a particular electron concentration upon degenerate doping of the material. Usually, the extra electron concentrations are of the order of $10^{19}-10^{21}$ cm^{-3}. Third, the partial DOS is commonly calculated within thse muffin-tin spheres and, therefore, the interstitial region which may give a significant contribution owing to the spatial distribution of the metal s-orbitals, is not taken into account.

To obtain a more reliable description of the conduction states in multicomponent oxides, we calculated the charge density distribution within an energy range at the bottom of the conduction band. For each RAMO$_4$ compound, the energy range was chosen to correspond to an extra electron concentration of 1.0-1.3$\times10^{21}$ cm^{-3}. The resulting Fermi energy displacement depends on the density of states at the bottom of the conduction band: a small density of states (i.e., high energy dispersion of the conduction band bottom) leads to a pronounced E$_F$ shift, while the Fermi level rises slow with electron concentration in the case of a large density of states. Specifically, we find that in InAMO$_4$ compounds the E$_F$ shift is large: it is 1.5 eV for InAlCdO$_4$, 0.9-1.0 eV for InACaO$_4$, and 1.1-1.3 eV for all other InAMO$_4$ compounds. In ScAMO$_4$, the presence of the Sc d states near the bottom of the conduction band result in a high density of states, and hence, the E$_F$ shift is significantly smaller, namely, 0.05 eV for ScAlMgO$_4$, $\sim$0.7 eV for ScAlZnO$_4$ and ScGaMgO$_4$, and 0.9 for ScGaZnO$_4$.

The charge density distributions calculated within the specified energy ranges are obtained for the full conventional unit cell of $RAMO_4$ to include both layers, $RO_{1.5}$ and $AMO_{2.5}$, and the interstitial region between the layers. We summed up the charge within each [0001] plane, Fig. 3.7, in order to compare the contributions from the two structurally and chemically different layers. We found that:

(1) Different layer contributions to the conduction band are nearly identical in $InGaZnO_4$, $InGaCdO_4$, and $InAlCdO_4$. Hence, both layers, $InO_{1.5}$ and $AMO_{2.5}$, are expected to participate in the charge transport once degenerate doping is achieved.

(2) In $InAlZnO_4$, $InGaMgO_4$, and $InGaCaO_4$, contributions from the In-O layer are larger, yet comparable to those from the A-M-O layers. Together with the compounds in the above case (1), these oxides possess two post-transition metals (In, Zn, Cd and/or Ga) and one light metal cation (Al, Mg or Ca). These results suggest that the $AMO_{2.5}$ layers where post-transition and light metals are mixed, will serve as conducting path for extra electrons in degenerately doped materials.

(3) If the $AMO_{2.5}$ layer consists of two light metal cations, as in $InAlMgO_4$ or $InAlCaO_4$, its contribution to the charge density is low, yet it is not zero as, for example, in $ScAlMgO_4$, Fig. 3.7(c). Similarly, the Sc-O layer contributions are negligible if the $AMO_{2.5}$ layer contains one or two post-transition metals, as in $ScGaZnO_4$, $ScGaMgO_4$, or $ScAlZnO_4$.

(4) In $ScAlMgO_4$, the Al-Mg-O layers have zero contributions, while the charge is localized within the Sc-O layer. Hence, if extra electrons are introduced, the $AMO_{2.5}$ layers would be non-conducting.

Thus, despite well-defined crystal lattice anisotropy and presence of a light metal cation in the $AMO_{2.5}$ layer, several $RAMO_4$ compounds are capable of giving rise to a nearly isotropic conductivity (i.e., within and across the structural layers) when properly doped. The role of light metal cations in carrier generation in these

multicomponent oxides, i.e., the effect of these cations on the formation of native electron-donor and electron-"killer" defects, should be investigated further.

3.5.3. Role of Atomic Coordination on the Conduction States. As mentioned in the introduction, the proximity of the cations empty p- or d states to the bottom of the conduction band may help predict the degree of electron localization in the oxides upon doping. Specifically, it was found [15] that in oxides of light metals, such as Ga_2O_3, CaO, Al_2O_3, or MgO, the Ga, Mg or Al p states or Ca d states are energetically compatible with the s states of cations in the conduction band. Upon electron doping, extra charge becomes trapped on the anisotropic p or d-orbitals which form strong covalent metal-oxygen bonds around defect, leading to the charge confinement (known as a color or F center). Now, we want to determine the energy location of the detrimental p- or d states of cations in the conduction band of multicomponent oxides. Our goal is to understand how the p- or d states location with respect to the conduction band bottom is affected by the local atomic coordination, i.e., the fivefold coordination in $RAMO_4$ versus the fourfold- or sixfold coordinations in the ground state structures of basis oxides.

First, we find that the local structural variations significantly affect the conduction bands of oxides – in addition to the band gap value discussed in the Sec. 3.5.1 above. Specifically, in rocksalt CaO with sixfold atomic coordination, the charge-trapping d states of Ca govern the bottom of the conduction band, being about 1.2 eV below the Ca s states, Fig. 3.8(a). In marked contrast to the ground-state CaO, we find that in hypothetical wurtzite CaO with fivefold coordinated Ca, the Ca d states are pushed into the conduction band and are *above* the s states, resulting in a direct band gap, Fig. 3.8(b). This occurs since the octahedral symmetry favors strong directional interaction between the d states of Ca and the p states of oxygen neighbors, whereas the s-p interaction is preferred when the symmetry is broken, as in fivefold coordinated Ca. Therefore, low-symmetry coordination helps diminish the
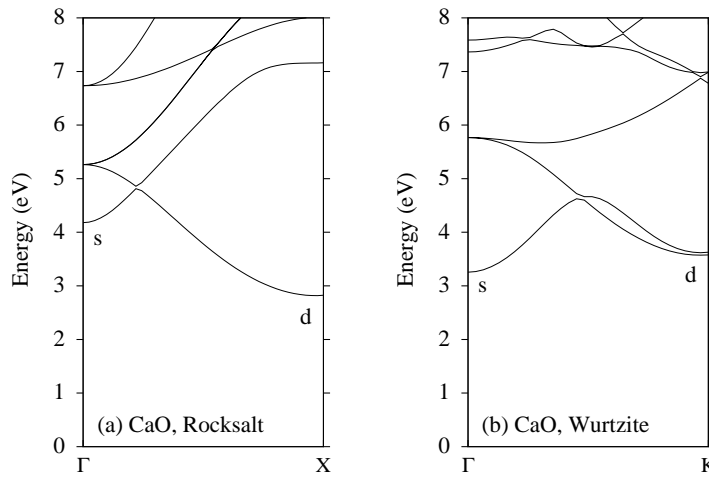
Figure 3.8: Electronic band structure of (a) rocksalt CaO, and (b) hypothetical wurtzite CaO with the interatomic distances matching those in $RACaO_4$. Only the bottom of the conduction band is shown. The calculations are performed within sX-LDA.

detrimental effect of the anisotropic d states on the oxide transport properties by promoting the s-character of the bottom of the conduction band. Further, from the calculated density of states for $InAlCaO_4$ or $InGaCaO_4$, Fig. 3.5, we find that the Ca d states are well above the bottom of the conduction band formed from the s states of the constituent cations. Similarly, the empty p band of Al, Mg, or Ga in $RAMO_4$ are located at a higher energy, i.e., deep inside the conduction band. We conclude that not only the unusual fivefold coordination of the A and M cations but also the hybridization between the spatially extended s states of the cations (via shared oxygen atoms) are the reasons for a deeper cation's p and d bands in $RAMO_4$. Because of the interaction of cations (e.g., in the mixed $AMO_{2.5}$ layers) and due to the difference in the band gaps of the constituent oxides, namely, 2.3-3.4 eV in CdO, In_2O_3, or ZnO, and 7-9 eV in CaO, MgO, or Al_2O_3, the bottom of the hybrid s-like conduction band of complex oxides is *driven away* from the Ga, Al, and Mg p states or Ca d states. The fact that the Ga, Al, Mg, or Ca atoms do contribute their states

(which are the s states) to the conduction band bottom is clearly illustrated by the calculated charge densities within different layers, Fig. 3.7. Hence, those atoms are expected to participate in change transport upon degenerate doping.

Here, we stress the importance of the fivefold coordination in the formation of the hybrid s-like conduction band in all considered $RAMO_4$ except those containing Sc. Because the Sc coordination is the same in $ScAMO_4$ and Sc_2O_3, i.e., octahedral, the Sc d states remain below its s states in all the oxides. As a result, the interaction between the Sc and other cations in a Sc-containing multicomponent oxide is very weak, and the bottom of the conduction band is formed by the states of the basis oxides with smaller band gap, i.e., Sc d states in $ScAlMgO_4$ or the s states of A and M atoms in $ScGaZnO_4$, $ScGaMgO_4$, or $ScAlZnO_4$. This leads to a clear separation of the particular layers (Sc-O layers in the former case and $AMO_{2.5}$ layers in the latter cases) into potentially conducting and non-conducting, Fig. 3.7.

3.5.4. Electron Effective Mass in $RAMO_4$. The electron effective masses calculated along the [100], [010], and [001] crystallographic directions in the multicomponent oxides $RAMO_4$ are given in Table 3.7. LDA underestimates the effective mass values which are in the range of 0.2-0.5 m_e, and the sX-LDA gives larger values – as expected from larger band gaps, Table 3.6. Within the sX-LDA, the smallest electron effective mass, 0.33 m_e, is found in $InGaCdO_4$, and the largest, 0.78 m_e, are in $ScAlMgO_4$. The trend in the effective mass values of $RAMO_4$ compounds follows the one in the calculated band gaps, c.f., Table 3.6. Significantly, we find that both LDA and sX-LDA yield isotropic electron effective masses, i.e., the m values along and across the structural layers are nearly identical in every $RAMO_4$ compound except for $ScAlMgO_4$. This is in agreement with the hybrid nature of the conduction band and the similar contributions from the R-O and A-M-O layers to the electron density, as discussed in sections 3.5.2 and 3.5.3

Table 3.7: Electron effective masses m, in m_e, calculated within sX-LDA along the specified crystallographic directions in RAMO$_4$ compounds. The components of the electron effective-mass tensor, $m_{a,b}$, m_z, and weighted $m_{a,b}^w$, m_z^w, calculated for both the ground state and hypothetical phases using the effective masses of the corresponding single-cation oxides from Table 3.5.

RAMO$_4$	Calculated			Predicted							
	$m_{[100]}$	$m_{[010]}$	$m_{[001]}$	m_{ab}^g	m_z^g	$(m_{ab}^g)^w$	$(m_z^g)^w$	m_{ab}^h	m_z^h	$(m_{ab}^h)^w$	$(m_z^h)^w$
InAlZnO$_4$	0.39	0.38	0.38	0.35	0.36	0.34	0.34	0.37	0.39	0.35	0.37
InAlCaO$_4$	0.49	0.50	0.46	0.37	0.38	0.34	0.35	0.41	0.44	0.36	0.40
InAlMgO$_4$	0.46	0.47	0.44	0.38	0.40	0.34	0.36	0.40	0.44	0.36	0.39
InAlCdO$_4$	0.38	0.38	0.38	0.32	0.32	0.32	0.31	0.36	0.37	0.35	0.36
InGaZnO$_4$	0.34	0.34	0.34	0.32	0.32	0.32	0.32	0.35	0.36	0.34	0.35
InGaCaO$_4$	0.43	0.44	0.42	0.34	0.35	0.33	0.33	0.39	0.41	0.37	0.39
InGaMgO$_4$	0.41	0.41	0.40	0.35	0.36	0.34	0.35	0.39	0.41	0.37	0.39
InGaCdO$_4$	0.33	0.34	0.33	0.28	0.28	0.28	0.28	0.33	0.34	0.34	0.34
ScGaZnO$_4$	0.44	0.45	0.43	0.45	0.63	0.39	0.49	0.51	0.66	0.45	0.53
ScAlZnO$_4$	0.48	0.51	0.48	0.51	0.66	0.48	0.59	0.56	0.69	0.52	0.61
ScGaMgO$_4$	0.53	0.54	0.52	0.51	0.66	0.48	0.59	0.59	0.71	0.56	0.65
ScAlMgO$_4$	0.78	0.69	0.64	0.57	0.70	0.90	1.04	0.64	0.74	0.95	1.06

In section 3.5.1, we demonstrated that the band gap in RAMO$_4$ compounds can be predicted via averaging over the values obtained for the single-cation oxide constituents with corresponding local atomic structure. Here, we perform similar analysis for the electron effective masses. The results are given in Table 3.7, where the LDA and sX-LDA values calculated for RAMO$_4$ compounds are given along with those obtained via averaging over the masses of the bases sinlge-cation oxides. The ab and z components of the average effective-mass tensors are found according to [36]. We find that:

1) Equal-weight or weighted averaging over the electron effective masses of the single-cation oxides in their ground state structures, c.f., m^g and $(m^g)^w$, underestimates the calculated mass values.

2) Averaging over the effective mass values of single-cation oxides in hypothetical phases with fivefold coordination gives better agreement with the calculated values. This may appear to be counterintuitive: since the band gap in hypothetical oxides is smaller compared to that calculated for the oxides in the ground state phases, Table 3.5, one may expect a smaller electron effective mass, and hence, a worse agreement between the calculated and predicted masses than in the case (1) above. However, according to the $\mathbf{k}\cdot\mathbf{p}$ theory, the electron effective mass depends not only on the band gap value, but also on the orbital overlap of the neighboring atoms:

$$\frac{m_e}{m_{ii}^{(c)}} = 1 + \frac{2}{m_e} \sum_{v \neq c} \frac{|\langle u^{(c)}|\hat{p}_i|u^{(v)}\rangle|^2}{E^{(c)} - E^{(v)}}, \tag{3.1}$$

where $\hat{\mathbf{p}}$ is the momentum operator, $|u^{(l)}\rangle$ is the Bloch wave function of the l's band at the Γ point (wave vector $\mathbf{k}$=0) and $E^{(l)}$ is its energy. Band labels v and c represent the valence and conduction bands, respectively. The smallest denominator corresponds to $E^{(c)} - E^{(v)} \approx E_g$, and thus, the smaller the band gap, the smaller the electron effective mass. The numerator represents the overlap between the orbitals in the valence band (oxygen p states) and in the conduction band (metal states). Because the overlap is greater in the higher-symmetry phases (with octahedral coordination for CaO, CdO, MgO, tetrahedral for ZnO, etc), the effective mass is smaller in the ground state phases as compared to the hypothetical structures.

3) With the exception for Sc-containing compounds, the equal-weight average provides a better match between the predicted and calculated mass values than the weighted average. For the latter, the respective weights are obtained based on the contributions to the charge density in an energy range at the bottom of the conduction band (see section 3.5.2 and Fig. 3.7). The energy range corresponds to a Fermi level

shift of 0.7 eV - 1.5 eV (see Sec. 3.5.2) However, it appears to be insufficient, and the states which are located deep in the conduction band – such as the states of lighter metals – play an important role in determining the electron effective mass of multicomponent oxides. Therefore, the corresponding light metal oxide constituents should be given a greater weight.

The above results suggest that the electron effective mass in multicomponent oxides is highly sensitive to the presence of all oxide constituents independent of their band gap value, i.e., both the semiconductor-like post-transition metal oxides and the insulator light-metal oxides play an equal role in the formation of the conduction band curvature. The local structural peculiarities, i.e., the fivefold coordination of A and M atoms, are of less significance here because of the opposite effect of a reduced orbital overlap and a smaller band gap associated with low symmetry of oxygen polyhedra on the resulting electron effective mass of multicomponent oxides.

3.6. CONCLUSIONS

In conclusion, the structural and compositional complexity of the considered multicomponent oxides with layered structure $RAMO_4$ allowed us to address two fundamental questions: (1) how the local atomic coordination affects their electronic properties such as the band gap, the electron effective mass and the nature of the conduction band; and (2) how the optical properties and the electron conduction paths of layered multicomponent oxide hosts vary with the chemical composition.

Most significantly, we demonstrate that the unusual fivefold coordination of the A^{3+} and M^{2+} metal atoms stabilized in $RAMO_4$ compounds, results in the electronic band structure of the complex oxides that differs from the one expected based on the electronic properties of the single-cation oxide constituents in their lowest-energy (ground state) phases. In particular, we find:

– The band gap in oxides shows strong dependence on the atomic coordination. High-symmetry octahedral (sixfold) coordination provides the largest overlap between the metal and oxygen orbitals giving rise to a large band gap. Other coordinations result in a smaller orbital overlap and, hence, the optical band gap is reduced. In multicomponent oxides, the band gap is determined not only by the oxide constituent with the smallest band gap but by *all* constituent oxides, although those of lighter metals (Al, Ca, Mg) have smaller contribution to the band gap average compared to the oxides of post-transition metals (In, Cd, Zn). The respective weights of the oxide constituents to the band gap average correlate with the calculated percent atomic contributions to the charge density in the conduction band.

– The electron effective mass in oxides does not follow the trend expected from the variation in the band gap: we find that the structures with five-coordinated metals exhibit smaller band gaps but larger electron effective masses as compared to their six-coordinated counterparts. This finding is explained based on the $\mathbf{k \cdot p}$ theory. In multicomponent oxides, all oxide constituents give equal contributions to the electron effective mass average.

– The unusual fivefold coordination of the A and M atoms in $InAMO_4$ compounds promotes a hybrid s-like conduction band making isotropic charge transport possible in this layered materials. The calculated charge density distribution shows that the light metal elements, such as Al, Ca, and Mg, contribute their s states to the hybrid conduction band of complex oxides whereas the contributions from their p or d states which are known to cause electron localization in the corresponding single-cation oxides, are significantly reduced.

- Although all compounds exhibit n-type asymmetry of the electronic band structure, a high carrier concentration is likely to be achieved only in $InGaCdO_4$, Fig. 3.9. Nevertheless, we believe that the oxides that contain light-metal constituents
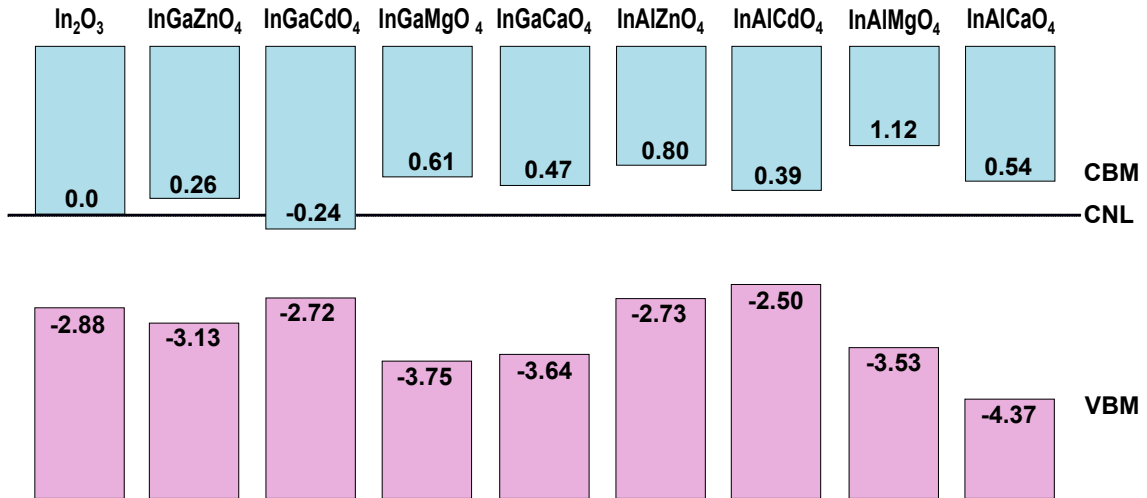
Figure 3.9: (Color online) The alignment of the valence and conduction band edges of InAMO$_4$ with respect to the charge neutrality level (CNL) calculated based on our sX-LDA results.

(Al, Mg or Ca) may hold promise for applications in which carrier densities must be kept low while the carrier mobilities are preserved.

Thus, the above results highlight the advantages of incorporating light main group metals in multicomponent oxides, which is highly attractive for lighter-weight, less-expensive, and environmentally-friendly devices. Further investigations of how the structural peculiarities and composition affect the formation of native defects in complex oxides are warrant in order to understand their role in carrier generation and transport in doped and/or non-stoichiometric oxides.

Acknowledgements

4. COMPOSITION-DEPENDENT OXYGEN VACANCY FORMATION IN MULTICOMPONENT WIDE-BAND-GAP OXIDES

Altynbek Murat[1] and Julia E. Medvedeva[1]

[1] *Department of Physics, Missouri University of Science & Technology,*

Rolla, MO 65409, USA

ABSTRACT[*]

The formation of oxygen vacancy in layered multicomponent InAMO$_4$ oxides with A^{3+}=Al or Ga, and M^{2+}=Ca or Zn, and in the corresponding binary oxide constituents is investigated using first-principles density functional calculations. Comparing the formation energies of the oxygen defect at six different site locations within the structurally and chemically distinct layers of InAMO$_4$ oxides, we find that the vacancy distribution is significantly affected not only by the strength of the metal-oxygen bonding, but also by the cation's ability to adjust to anisotropic oxygen environment created by the vacancy. In particular, the tendency of Zn, Ga, and Al atoms to form stable structures with lower oxygen coordination, results in nearly identical vacancy concentrations in the InO$_{1.5}$ and GaZnO$_{2.5}$ layers in InGaZnO$_4$, and only an order of magnitude lower concentration in the AlZnO$_{2.5}$ layer as compared to the one in the InO$_{1.5}$ layer in InAlZnO$_4$. The presence of two light metal constituents in the InAlCaO$_4$ along with Ca failure to form a stable fourfold coordination as revealed by its negligible relaxation near the defect, leads to a strong preference of the oxygen vacancy to be in the InO$_{1.5}$ layer. Based on the results obtained, we propose several oxides as potential constituents of multicomponent functional materials with tunable properties.

[*]Submitted for publication in Physical Review B.

4.1. INTRODUCTION

The presence of light main-group metals such as Al, Mg or Ca in multicomponent transparent conducting and semiconducting oxides [1, 5, 31, 37, 68] is highly attractive since these cations help stabilize the multi-cation structure, allow for a broader optical transmission window due to a larger band gap, and also help control the carrier content while preserving the carrier mobility.

Recent systematic electronic band structure investigations [30] of undoped stoichiometric $InAMO_4$ compounds with A^{3+}=Al or Ga, and M^{2+}=Ca or Zn, [11] showed that the electronic properties of these layered-structured multicomponent oxides resemble those in the conventional binary transparent conductive oxides (TCOs): both exhibit a dispersed s-like conduction band and possess a small (0.3–0.5 m_e), isotropic electron effective mass. Strikingly, it was found that despite the different band gaps of the constituent basis binary oxides (2–4 eV In_2O_3 or ZnO; 5 eV for Ga_2O_3; and 7–9 eV in CaO or Al_2O_3), the states of *all* cations contribute to the bottom of the conduction band of the multicomponent oxide. Such a hybrid conduction band can be expected to provide a uniform network for the carrier transport within and across the chemically and structurally distinct layers of the $InAMO_4$ materials.

To understand how the chemical composition affects carrier generation in complex oxides, comparative investigations of non-stoichiometric $InAMO_4$ compounds are required. In this work, we study the electronic properties of oxygen deficient $InGaZnO_4$, $InAlZnO_4$, and $InAlCaO_4$. We determine the distribution of oxygen vacancies within the layered structure of the $InAMO_4$ compounds by comparing the calculated formation energies of the oxygen vacancy defects at various locations within the $InO_{1.5}$ and $AMO_{2.5}$ layers, Fig. 4.1(a). We find that the location preference of the oxygen vacancy correlates with the defect formation energies obtained for the corresponding single-cation oxide constituents. At the same time, we show that the vacancy formation energies in $InAMO_4$ are strongly affected by the highly anisotropic
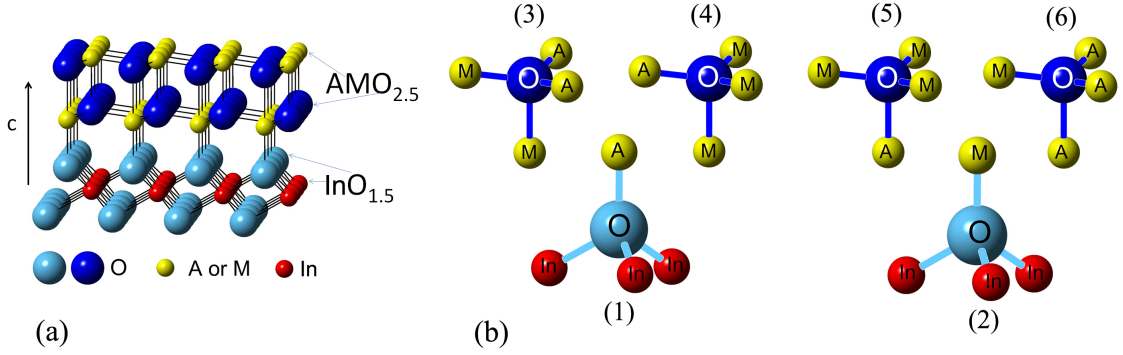
Figure 4.1: (a) (Color online) Crystal structure of InAMO$_4$, specifically, one of the three similar blocks which construct the conventional unit cell when stacked along the z direction, is shown. (b) Six structurally different possible sites for the oxygen vacancy defect with different nearest-neighboring atoms in the layered multicomponent InAMO$_4$ oxides.

atomic relaxation near the defect associated with the presence of several cations of different valence, ionic radius, and strength of their interaction with the neighbor oxygen atoms.

4.2. APPROACH

First-principles full-potential linearized augmented plane wave (FLAPW) [20, 47] method within the local density approximation is employed for the investigation of the defect formation energies and the electronic properties of InAMO$_4$ oxides (A^{3+}=Al or Ga and M^{2+}=Ca or Zn), as well as their single-cation constituents, CaO, ZnO, In$_2$O$_3$, Al$_2$O$_3$, and Ga$_2$O$_3$. Cutoffs for the basis functions, 16.0 Ry, and the potential representation, 81.0 Ry, and expansion in terms of spherical harmonics with $\ell \leq 8$ inside the muffin-tin spheres were used. The muffin-tin radii of multicomponent and single-cation oxides are as follows: 2.3 to 2.6 a.u. for In and Ca; 1.7 to 2.1 a.u. for Ga, Zn, and Al; and 1.45 to 1.8 a.u. for O atoms. Summations over the Brillouin zone were carried out using at least 23 special $\mathbf{k}$ points in the irreducible wedge.

The investigated InAMO$_4$ oxides have rhombohedral $R\bar{3}m$ layered crystal structure of YbFe$_2$O$_4$ type, Fig. 4.1(a) [74, 75, 80]. In these compounds, In^{3+} ions have octahedral coordination with the oxygen atoms and reside in 3(a) position (Yb), whereas both A^{3+} (Al or Ga) and M^{2+} (Ca or Zn) ions reside in 6(c) position (Fe), Fig. 4.1, and are distributed randomly [81]. Because of the different ionic radii and the valence state of the cations in the AMO$_{2.5}$ double layer, the A^{3+} and M^{2+} atoms have different z component of the internal site position 6(c). The optimized structural parameters for every structure under consideration can be found in our previous work [30].

To model isolated point defects in the InAMO$_4$ compounds, a 49-atom supercell was used with the lattice vectors $(30\bar{2})$, $(\bar{1}12)$, and $(02\bar{1})$, given in the units of the rhombohedral primitive cell vectors [36]. Note that the conventional rhombohedral unit cell of YbFe$_2$O$_4$ contains 21 atoms (Z=3), and the primitive, i.e., the smallest volume, cell contains 7 atoms (Z=1). For the binary basis oxides, the following supercells were constructed: a 80-atom supercell for bixbyite In$_2$O$_3$ and corundum Al$_2$O$_3$; a 120-atom supercell for monoclinic β-Ga$_2$O$_3$; a 84-atom supercell for wurtzite ZnO; and a 128-atom supercell for rocksalt CaO. These supercells result in similar defect concentrations, namely, 1.6–1.8$\times 10^{21}$cm^{-3}, and, hence, similar distances between the oxygen defects $\sim$ 10Å. We stress that such high concentrations may not be experimentally feasible in all materials under consideration. However, our goal is to determine the role played by the chemical composition in the defect formation, hence, the properties must be compared under the same conditions. The values of the defect formation energies calculated for the given supercells, can be used to predict the temperature-dependent defect densities in each compound, and are known to provide reasonable results [42, 44].

As mentioned above, the layered crystal structure of InAMO$_4$ oxides has two chemically and structurally distinct layers, AMO$_{2.5}$ and InO$_{1.5}$, which alternate

along the [0001] direction. Depending on the layer and the different nearest-neighbor cations, there are several structurally different sites for the oxygen vacancy defect. Figure 4.1(b) shows the six possible defect sites considered for the InAMO$_4$ oxides. During the discussions that follow, we identify the defect sites by their nearest-neighbor atoms, specifically, by their planar and apical cations. For example, as one can see from Fig. 4.1(b), the sites 4 and 5 both have three neighbors of atom type M (Zn or Ca) and one neighbor of type A (Ga or Al). However, the sites are different due to the different set of the planar atoms versus the apical atom resulting in a different total energies for these sites, as it will be shown below.

The formation energy of the oxygen vacancy in three charge states, i.e., neutral V$_O^0$ and ionized V$_O^+$ or V$_O^{2+}$, modeled using a corresponding background charge, can be calculated as a function of the Fermi level and the corresponding chemical potential:

$$\Delta H(E_F, \mu) = E_{defect} - E_{host} + \mu_O + q(E_F) \tag{4.1}$$

where E_{defect} and E_{host} are the total energies for the oxygen deficient oxide and the stoichiometric oxide in the same-size supercell, respectively; μ is the chemical potential for an oxygen atom removed from the lattice; q is the defect charge state, E_F is the Fermi energy taken with respect to the top of the valence band.

The chemical potential $\mu_O = \mu_O^0 + \Delta\mu_O$ is taken with respect to the chemical potential μ^0 of the O$_2$ molecule, whereas $\Delta\mu_O$ is the deviation from the elemental chemical potential. In this work, with the purpose of reasonable comparison between the quaternary and binary oxides, we consider two extreme cases of the growth conditions. In the extreme oxygen-rich conditions, $\Delta\mu_O$=0. In the oxygen-poor, i.e., metal-rich conditions, $\Delta\mu_O$ depends on the respective values of the heat of formation, ΔH_f[InAMO], as well as on $\Delta\mu_{In}$, $\Delta\mu_A$, and $\Delta\mu_M$ which are calculated from the following thermodynamic stability conditions:

(1) In order to maintain a stable $InAMO_4$ host, the elemental chemical potentials should have the values that require

$$\Delta\mu_{In} + \Delta\mu_A + \Delta\mu_M + 4\Delta\mu_O = \Delta H_f[InAMO_4] \tag{4.2}$$

(2) To avoid the precipitation of the elements In, A, M, and O, the following conditions must be satisfied:

$$\Delta\mu_{In} \leq 0; \Delta\mu_A \leq 0; \Delta\mu_M \leq 0; \Delta\mu_O \leq 0 \tag{4.3}$$

(3) To avoid the formation of the binary compounds, such as In_2O_3, A_2O_3, or MO, the following conditions must be fulfilled:

$$2\Delta\mu_{In} + 3\Delta\mu_O \leq \Delta H_f(In_2O_3) \tag{4.4}$$

$$2\Delta\mu_A + 3\Delta\mu_O \leq \Delta H_f(A_2O_3) \tag{4.5}$$

$$\Delta\mu_M + \Delta\mu_O \leq \Delta H_f(MO) \tag{4.6}$$

Thus, the available range for the elemental chemical potentials in the case of quaternary $InAMO_4$ materials is a three-dimensional volume determined by the above stability conditions (equations 5.3– 5.6), projected onto the corresponding $InAMO_4$ plot (equation 5.2).

The heat of formation, ΔH_f, for the oxides is calculated with respect to the bulk orthorhombic Ga, tetragonal In, hexagonal Zn, and cubic Al or Ca. Our obtained ΔH_f values for the three representative $InGaZnO_4$, $InAlZnO_4$, and $InAlCaO_4$ compounds are –11.28 eV, –14.60 eV, and –15.40 eV, respectively. Calculating the corresponding heat of formation for the binary constituents [c.f., Table 4.1], we find

that:

$$2\Delta H_f[InGaZnO_4] > \Delta H_f(In_2O_3) + \Delta H_f(Ga_2O_3) + 2\Delta H_f(ZnO) \quad (4.7)$$

$$2\Delta H_f[InAlCaO_4] > \Delta H_f(In_2O_3) + \Delta H_f(Al_2O_3) + 2\Delta H_f(CaO) \quad (4.8)$$

$$2\Delta H_f[InAlZnO_4] < \Delta H_f(In_2O_3) + \Delta H_f(Al_2O_3) + 2\Delta H_f(ZnO) \quad (4.9)$$

The equations 5.7 and 5.8 suggest that at zero temperature, the formation of $InGaZnO_4$ or $InAlCaO_4$ is impossible without the formation of the corresponding binary phases. This also means that there is no available elemental chemical potentials which would allow the formation of the corresponding multicomponent oxides. Since the latter are stable above 1000 K [74, 75, 80], the entropy term $T\Delta S$ must be taken into consideration. Similar arguments were reported for $In_2O_3(ZnO)_k$ compounds [82]. The entropy term can be estimated based on the corresponding equilibrium solid state reactions which involve the binary constituents as follows:

$$\Delta H_f[InGaZnO_4] - 1/2[\Delta H_f(In_2O_3) + \Delta H_f(Ga_2O_3) +$$
$$2\Delta H_f(ZnO)] = T_{InGaZnO_4} \times \delta S_{InGaZnO_4} \quad (4.10)$$

$$\Delta H_f[InAlCaO_4] - 1/2[\Delta H_f(In_2O_3) + \Delta H_f(Al_2O_3) +$$
$$2\Delta H_f(CaO)] = T_{InAlCaO_4} \times \delta S_{InAlCaO_4} \quad (4.11)$$

We then replace the ΔH_f for InGaZnO$_4$ and InAlCaO$_4$ with the corresponding $[\Delta H_f - T \times \delta S]$, in the equation 5.2 above. As a result, the available chemical potentials for metals in InGaZnO$_4$, InAlZnO$_4$, and InAlCaO$_4$, plotted in Fig. 4.2, correspond to a very narrow range along the crossing line of the three planes, eqs. 5.4-5.6. This is in accord with the results for Ga-free layered multicomponent In$_2$O$_3$(ZnO)$_3$ which was shown to exist without the occurrence of the secondary phases only for a constant ratio between indium and zinc [82]. For the extreme metal-rich conditions,
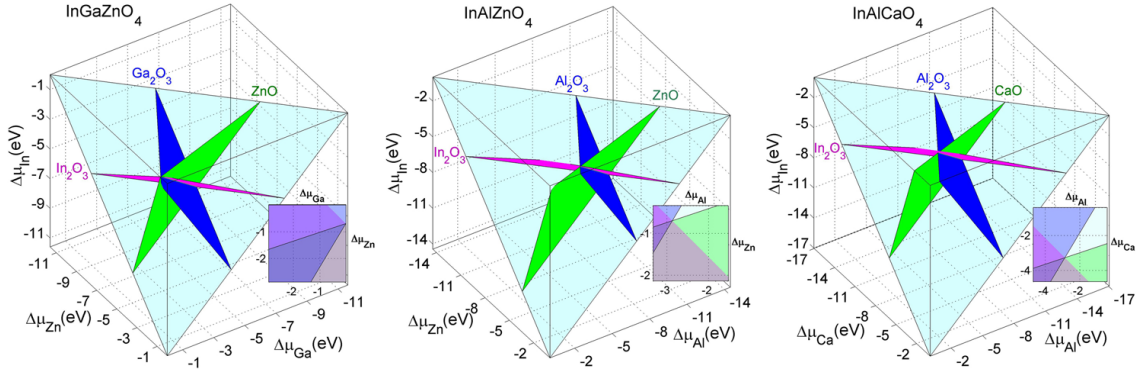
Figure 4.2: (Color online) Available elemental chemical potentials for InGaZnO$_4$, InAlZnO$_4$, and InAlCaO$_4$. Shaded planes represent the stability of constituent binary phases. The inserts show the extreme metal-rich values ($\Delta\mu_{In}$=0).

we obtain:

(a) InGaZnO$_4$: $\Delta\mu_{In}=\Delta\mu_{Ga}=0$, $\Delta\mu_{Zn}=$–0.70 eV;

(b) InAlZnO$_4$: $\Delta\mu_{In}=0$, $\Delta\mu_{Zn}=$–0.61 eV, $\Delta\mu_{Al}=$–2.75 eV; and

(c) InAlCaO$_4$: $\Delta\mu_{In}=0$, $\Delta\mu_{Al}=$–2.9 eV, $\Delta\mu_{Ca}=$–3.3 eV.

We stress again that for the clarity of this paper, we do not consider intermediate oxygen pressures, i.e., $1/4[\Delta H_f[InAMO_4] - \sum \Delta\mu_{metal}^{M-rich}] < \Delta\mu_O < 0$. Investigations of possible charge compensation mechanisms (e.g., formation of metal vacancies) are also beyond the scope of this work, and will be discussed elsewhere [83].

4.3. RESULTS AND DISCUSSION

4.3.1. Oxygen Vacancy in Binary Oxides. The first step to understand the effect of the chemical composition on the formation and distribution of an oxygen vacancy in layered multicomponent InAMO_4 oxides, is to compare the formation energies of the oxygen defect in the corresponding binary oxides. Our calculated formation energies of the neutral oxygen defect, V$_O^0$, are shown in Table 4.1, for both oxygen-poor and oxygen-rich conditions. It can be seen that the difference

Table 4.1: Calculated and experimental heat of formation of binary oxides, ΔH_f per oxygen in eV, and the calculated formation energy of a neutral oxygen vacancy, $\Delta H[V_O^0]$, in eV, for both oxygen-poor and oxygen-rich conditions.

| | ΔH_f per oxygen | | $\Delta H[V_O^0]$ | |
	Calc	Exp	O-poor	O-rich
CaO	-6.00	-6.57	0.87	7.02
Al_2O_3	-4.64	-5.78	1.82	7.10
Ga_2O_3	-2.74	-3.73	0.69	3.92
ZnO	-3.42	-3.60	0.69	4.10
In_2O_3	-2.72	-3.21	1.10	3.82

in the defect formation energies for the post-transition and the light-metal oxides is about 3 eV or higher in the oxygen-rich conditions ($\Delta\mu_O$=0). The trend in the defect formation energies correlates with the heat of formation of the binary oxides, Table 4.1: the low heat of formation of post-transition metal oxides signifies that the oxygen vacancies are abundant in these oxides.

Under the *extreme* metal-rich conditions, i.e., when $\Delta\mu_{metal}$=0, and $\Delta\mu_O$ is determined by ΔH_f^{calc} according to the equations 5.4-5.6, the differences in the defect formation energies in the binary oxides become less obvious. As it was mentioned above, with the purpose of fair comparison between the oxides, we do not consider intermediate oxygen pressures. For each particular compound, the pressure ranges may be limited by the experimental characteristics, e.g., the annealing temperature which also affects the value of $\Delta\mu_O$, as well as by the formation of undesired intrinsic defects. In particular, studies of the charge compensation, e.g., due to a low formation energy of the metal vacancy in Al_2O_3 and CaO which are necessary to explain the insulating behavior in these light-metal oxides, are beyond the scope of this work and will be presented elsewhere [83].

Our calculated formation energies of the neutral oxygen defect, V_O^0, Table 4.1, are in a good agreement with prior reported formation energies for neutral oxygen defect in the binary oxides, such as 0.6 eV for O-poor and 6.6 eV for O-rich in CaO, 7.5 eV for O-rich in Al_2O_3, 1.2 eV for O-poor and 3.8 eV for O-rich in ZnO, 1.0 eV for O-poor and 3.7 eV for O-rich in In_2O_3 [42, 44, 84].

The fact that it is easier to create an oxygen vacancy in the post-transition metal oxides, i.e., In_2O_3 or ZnO, as compared to the light main-group metal oxides, i.e., Al_2O_3 or CaO, is in accord with the calculated degree of the electron localization around the oxygen defect [15]. A more uniform charge distribution at the bottom of the conduction band was found in the oxygen deficient post-transition metal oxides. In contrast, the light-metal oxides exhibit a strong charge confinement near the oxygen vacancy (an F-like center). It was shown that the electron localization in the latter oxides is associated with the formation of the strong directional metal p – oxygen p bonds around the defect [19].

We note here that Ga_2O_3 should be placed at the far end of the conventional TCO hosts such as In_2O_3 and ZnO which have low formation energy of the oxygen vacancy. In Ga_2O_3, there are 3 non-equivalent oxygen sites, which we label as site 1, 2, or 3, with 3, 4, or 6 Ga neighbor atoms at the average distance of 1.90 Å, 2.00 Å, or 1.87 Å, respectively. Consequently, the formation energies of the oxygen vacancy in those sites are different and correlate with the average Ga-O distances for each site: we obtained 1.09 eV, 1.31 eV, or 0.69 eV under the metal-rich conditions, and 4.32 eV, 4.55 eV, or 3.92 eV under the oxygen-rich conditions, for the sites 1, 2, or 3, respectively. Note that only the lowest values are given in the Table 4.1. Since the concentration of a defect is proportional to the number of the sites available for the defect, only a third of the oxygen atoms in Ga_2O_3 may produce a vacancy defect with the formation energy similar to that in ZnO, i.e., 0.69 eV under the O-poor conditions, Table 4.1. The higher formation energy of the V_O at the other oxygen sites (i.e., sites

1 and 2) sets Ga_2O_3 somewhat in between the two oxide groups considered above. Again, this finding is consistent with the obtained degree of the electron localization near the oxygen vacancy defect, $In_2O_3 < ZnO < Ga_2O_3 < CaO < Al_2O_3$ [15]. The Ga_2O_3 results above also reveal that the oxygen vacancy formation energy depends strongly on the coordination and the metal-oxygen distances.

4.3.2. Distribution of Oxygen Vacancies in InAMO$_4$. In this section, we investigate how the presence of light-metal cations (Ca and/or Al) affects the distribution of the oxygen vacancies within the structurally and chemically distinct layers of multicomponent oxides. The chosen three InAMO$_4$ compounds, namely $InGaZnO_4$, $InAlZnO_4$, and $InAlCaO_4$, represent the systems with none, one, and two light-metal constituents, respectively. We believe that the trends obtained for these three oxides may help us understand the role played by the composition in the defect formation and make reasonable predictions for other multicomponent oxides.

First, to determine the most energetically favorable location of the oxygen vacancy in $InGaZnO_4$, $InAlZnO_4$, and $InAlCaO_4$, we calculate the formation energies of the oxygen vacancy defect in the six structurally different oxygen sites which were discussed above and shown in Fig. 4.1(b). The results are given in Table 4.2. Our comparative analysis of the defect formation energies shows that the oxygen vacancy prefers to be within the $InO_{1.5}$ layer for all three representative compounds. There are two oxygen site positions within the $InO_{1.5}$ layer, site-1 and site-2, which differ by the type of the apical atom, i.e., A or M, respectively, Fig. 4.1(b). Comparing the formation energies of the oxygen vacancies at these two sites, we find that in the case of $InGaZnO_4$ and $InAlZnO_4$, the oxygen vacancy defects prefer to be in the site-2 position with three In atoms and one Zn (apical) atom as their nearest-neighbors. In contrast, in $InAlCaO_4$, the lowest formation energy corresponds to the defect in site-1 with three In and one apical Al as the defect nearest-neighbors. We note here, that similar trends in the formation energies of the oxygen vacancy at different site

Table 4.2: Formation energies of neutral oxygen vacancy located at 6 different defect sites in InGaZnO$_4$, InAlZnO$_4$, and InAlCaO$_4$ for oxygen-poor and oxygen-rich conditions. NN denotes the nearest-neighbor atoms and "a" stands for an apical atom. The lowest formation energy values are given in bold.

Site	NNs	InGaZnO$_4$		InAlZnO$_4$		InAlCaO$_4$	
		O-poor	O-rich	O-poor	O-rich	O-poor	O-rich
1	3R, 1A-a	1.51	4.24	1.43	4.24	**1.27**	**3.98**
2	3R, 1M-a	**1.32**	**4.05**	**1.34**	**4.15**	1.39	4.10
3	2A, 2M-a	1.61	4.34	2.95	5.76	3.26	5.97
4	1A, 3M-a	1.38	4.12	2.00	4.81	2.97	5.68
5	1A-a, 3M	1.35	4.09	1.57	4.38	2.67	5.38
6	3A-a, 1M	1.68	4.42	3.14	5.95	3.08	5.79

positions are obtained for the ionized vacancy defect with the exception for InGaZnO$_4$ where the lowest formation energy of V$_O^+$ is for the defect at site-5 while the defect at site-2 is higher in energy by only 0.02 eV.

For the considered three compounds, the defect preferred site location correlates well with the experimental heat of formation of the corresponding binary oxides, and, accordingly, with the oxygen vacancy formation energy, c.f., Tables 4.1 and 4.2. For example, in InGaZnO$_4$ or InAlZnO$_4$, In$_2$O$_3$ has the lowest heat of formation per oxygen (–3.21 eV) followed by ZnO (–3.60 eV) and Ga$_2$O$_3$ (–3.73 eV) or Al$_2$O$_3$ (–5.78 eV). Hence, the site-2 in the InO$_{1.5}$ layer corresponds to the set of the metal-oxygen bonds – three In-O bonds and one Zn-O bond – that would be easiest to break in order to create an oxygen vacancy defect. Accordingly, for the InAlCaO$_4$ oxide, the oxygen vacancy prefers to be in the site-1 with three In and one Al neighbor atoms rather than in the site-2 with three In and one Ca neighbors, since CaO has stronger metal-oxygen bonds than Al$_2$O$_3$.

The above results suggest that the oxygen vacancy has a preference to form within the $InO_{1.5}$ layer, independent of the chemical composition of the three compounds. However, the preference for the octahedral $InO_{1.5}$ layer is strong only for $InAlCaO_4$: the vacancy formation energy in the $AlCaO_{2.5}$ layer is higher by at least 1.3 eV than that for the oxygen vacancy defect in the $InO_{1.5}$ layer, Table 4.2. In marked contrast to $InAlCaO_4$ with two light-metal constituents, the oxygen vacancy distribution is likely to be more uniform throughout the layered structure of $InGaZnO_4$ and $InAlZnO_4$. In $InGaZnO_4$, the difference in the defect formation energies between site-2 (three In and one Zn) and sites 4 and 5 (three Zn and one Ga) is negligible. Therefore, one can expect the vacancy concentrations to be comparable in the $InO_{1.5}$ and $GaZnO_{2.5}$ layers of $InGaZnO_4$. In $InAlZnO_4$, the difference in the defect formation energies between site-2 and site-5 is larger, about 0.2 eV. In this case, we can estimate that the resulting defect concentrations will differ by about an order of magnitude at 1000 K (which is a typical annealing temperature in oxides).

Figure 4.3 shows the estimated concentrations of the oxygen vacancy defect in the neutral charge state in the $InO_{1.5}$ and $AMO_{2.5}$ layers as a function of growth temperature. The figure clearly illustrates that the presence of one light-metal constituent in the mixed $AMO_{2.5}$ layer reduces the concentration of the electron donor defect in that layer, but does not suppress it completely as in the case when both A and M atoms are light metals. We note, that other charge states of the oxygen vacancy may contribute to the overall V_O concentration if acceptor defects such as cation vacancies, oxygen interstitials, and/or antisite defects, become abundant pushing the equilibrium Fermi level away from the conduction band.

4.3.3. Formation of Stable Fourfold Structures in Oxygen Deficient InAMO$_4$. Comparing the energetics for the six different defect sites, we find another trend that can be explained based on the heat of formation of the constituent binary oxides. Specifically, in $InAlZnO_4$, the defect formation energy, $\Delta H(V_O)$, increases as
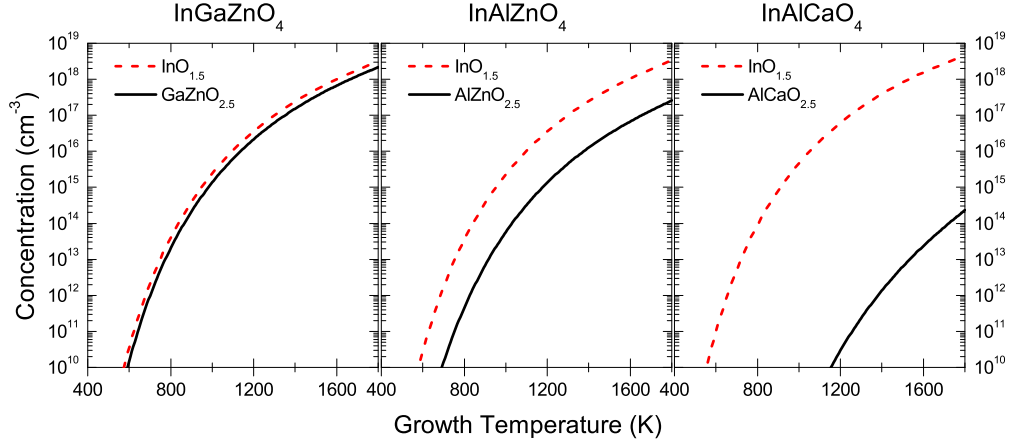
Figure 4.3: (Color online) Concentrations of the oxygen vacancy defect in the neutral charge state in the $InO_{1.5}$ and $AMO_{2.5}$ layers as a function of growth temperature calculated under the extreme oxygen-poor conditions.

the number of the Al atoms around the oxygen defect increases: site-1 (one apical Al and three In) < site-5 (one apical Al and three Zn) < site-4 (one planar Al) < site-3 (two planar Al) < site-6 (two planar and one apical Al). Therefore, the oxygen vacancy in $InAlZnO_4$ "avoids" having Al as a neighbor cation. Indeed, the Al-O bond is the strongest compared to the In-O and Zn-O bonds in $InAlZnO_4$, and the oxygen vacancy defect is least likely to be formed near the Al atoms. This tendency is stronger when the Al is a planar neighbor rather than the apical one simply because the planar metal-oxygen distances are generally shorter than the apical ones in the layered $InAMO_4$ compounds.

Similar to $InAlZnO_4$, the oxygen vacancy distribution exhibits a trend with respect to Ga in $InGaZnO_4$, where the formation energy of the defect in the sites with one Ga neighbor (sites 1, 4, and 5) is lower than that in the site-3 (two Ga neighbors) or site-6 (three Ga neighbors). However, simple arguments based on the comparison of the heat of formation of the binary oxides do not explain all the results obtained. In particular, in $InGaZnO_4$ the formation energy of the oxygen vacancy at site-5 (three Zn and one Ga neighbor) is lower than the one at site-1 (three In

and one Ga) although the heat of formation of In_2O_3 is lower as compared to that of ZnO, Table 4.1. We believe that one of the possible explanations involves the cation preference for a particular oxygen coordination. For instance, in the ground-state phase of ZnO, the wurtzite structure, Zn has fourfold coordination with O atoms. In bixbyite In_2O_3, as well as in other available phases for indium oxide, In is always sixfold coordinated with O atoms. In $InGaZnO_4$ compound, all Zn (and Ga) atoms are in fivefold coordination with oxygen atoms whereas In atoms remain in the sixfold coordination. After removal of the oxygen atom in site-5, three Zn atoms become fourfold coordinated with oxygen. Owing to the preference of Zn atoms to be in the fourfold coordination, the defect in site-5 (or site-4) become energetically more favorable compared to the site-1 defect where three In atoms lose one oxygen neighbor to become fivefold coordinated. (As it will be shown in the next section below, Zn atoms near the defect experience much stronger relaxation, with the Zn-V_O^0 distances reduced by 8 % for the site-5 case, Table 4.2, whereas the In-V_O^0 distances change only by 1-2 %.)

Accordingly, the most stable configuration of the oxygen defect in the $AlZnO_{2.5}$ layer of $InAlZnO_4$ corresponds to the structure with three fourfold coordinated Zn (site-5). The formation energy in this case is higher by only 0.14 eV as compared to the defect at site-1, Table 4.3. (As it will be discussed below, Zn relaxation is restricted due to the presence of the strong Al-O bonds that limits the ability of Zn to form a more stable fourfold coordinated structure.)

In marked contrast to Zn, Ca does not exhibit a preference for fourfold coordination being sixfold-coordinated with oxygen in the ground state (rocksalt structure) as well as in most CaO-Al_2O_3 structures [85]. Thus, in $InAlCaO_4$, the difference between the formation energies in site-1 and site-5 is large, 1.4 eV, which is mainly determined by the differences in the metal-oxygen binding in binary oxides, Table 4.1. In other words, there is no additional energy gain associated with the formation of a

stable fourfold structure similar to the one observed in the case of Zn, since Ca is indifferent to the formation of such structure and, as it will be shown below, experience negligible relaxation upon oxygen removal – in marked contrast to Zn in $InGaZnO_4$ and $InAlZnO_4$.

While Zn shows a strong preference for the fourfold coordination, Al and Ga can exist in either sixfold or fourfold oxygen coordination. The corundum Al_2O_3 has octahedrally coordinated Al atoms, but there are many phases where Al is in fourfold coordination with oxygen [85]. In the ground-state monoclinic phase, Ga_2O_3 has two nonequivalent Ga atoms – one being fourfold coordinated and the other in sixfold coordination. Therefore, we believe that both Al and Ga can form a stable fourfold structure when losing one oxygen atom upon introduction of an oxygen vacancy in the $InAMO_4$ compounds. The formation of such structures is illustrated below based on the atomic relaxation near the oxygen defect.

4.3.4. Structural Relaxation in Oxygen Deficient InAMO$_4$. The role of oxygen coordination in the vacancy formation and distribution in $InAMO_4$ can be further understood by considering the structural relaxation caused by the defect. For this, we compared the changes in the positions of the metal and oxygen atoms near the vacancy defect. Table 4.3 shows how much the metal atoms nearest to the oxygen vacancy shift with respect to their original positions in the stoichiometric oxide. First of all, we note that in all three multicomponent oxides, the apical atoms move away from the defect (positive ΔD-a) and the values are generally larger compared to the change in the planar distances, $\Delta D^{A/M}$, some of which are positive (cations move away from the defect), while others are negative (cations get closer to the defect). The larger relaxation of the apical atoms is inherent to the layered structure of $InAMO_4$ compounds: stacking the cations of different ionic radius, valence, and metal-oxygen

Table 4.3: Upon the atomic relaxation caused by the oxygen defect, the change in the distance between the vacancy and its nearest apical metal atom, ΔD-a, and the average change in the distances between the vacancy and the planar A or M atoms, ΔD^A or ΔD^M, in percent, are given.

	InGaZnO$_4$			InAlZnO$_4$			InAlCaO$_4$		
Site	ΔD-a	ΔD^A	ΔD^M	ΔD-a	ΔD^A	ΔD^M	ΔD-a	ΔD^A	ΔD^M
1	+10			+16			+14		
2	+8			+9			0		
3	+3	−5	0	+1	+3	−1	+3	−3	−1
4	+5	−5	−3	+3	+6	−4	+3	−1	−1
5	+9		−8	+13		−7	+14		−1
6	+6	−6	+1	+3	+1	−1	+1	−4	−1

bond strength along the c direction leads to larger deviations from the regular metal-oxygen distances in the corresponding binary oxides [30], and hence allows more freedom for relaxation.

Comparing the apical atom's shifts, ΔD-a, for InGaZnO$_4$ and InAlCaO$_4$, we find that the shifts are large for both Ga and Zn apical atoms in the former oxide, whereas in the two-light-metal compound, apical Al atoms exhibit more significant changes, 14%, compared to the apical Ca atoms, 0-3%. Accordingly, the Ca planar atoms exhibit only a small relaxation, $\Delta D^{Ca} \sim 1\%$ for all vacancy sites, as compared to the planar Zn, Al and Ga atoms shifts. The negligible relaxation of Ca as compared to the relaxation of Zn, Al, or Ga, can be explained by several factors: (i) the large ionic radius of Ca ion as compared to those of Zn, Ga and Al (given in the order of decreasing ionic radii); (ii) the stronger bonds between Ca and its nearest O neighbors with respect to the oxygen bonds with Zn, Ga and Al, as determined by the heat of formation of the binary oxides, Table 4.1; as well as (iii) Ca indifference to losing one oxygen neighbor to become a fourfold coordinated cation. All the factors above

limit the motion of Ca in the lattice with oxygen defect. In contrast to Ca atoms, the smaller ionic radius, weaker metal-oxygen bonds, and a possibility to form a fourfold structure make it easier for Al, Zn, and Ga to adjust to the new electronic environment created by the oxygen defect and, hence, those atoms experience greater relaxation (Table 4.3).

Further confirmation of our observations above can be obtained based on the optimized distances between the metal atoms which surround the defect and their oxygen neighbors. We find that in $InGaZnO_4$, the atomic relaxation results in slightly increased planar Zn-O distances (from $\sim$1.98 Å to $\sim$2.05 Å) and notably decreased apical Zn-O distance (from 2.41 Å to $\sim$2.20 Å) making all four Zn-O distances more alike to resemble the fourfold coordination. Similarly, the apical Ga atoms near the vacancy pull their oxygen neighbors to become four-coordinated with oxygen: all four Ga-O distances are found to be within 1.86–1.89 Å, which is close to the distances between the fourfold coordinated Ga and oxygen atoms in monoclinic Ga_2O_3, 1.83–1.86 Å (for comparison, the distances between the sixfold coordinated Ga and oxygen atoms in monoclinic Ga_2O_3 are 1.93–2.07 Å).

Significantly, we find that Zn propensity to become fourfold-coordinated upon losing an oxygen neighbor decreases in $InAlZnO_4$ as compared to $InGaZnO_4$, i.e., when Ga atoms in the A sublattice are changed to Al. We obtain that the distances between the Zn atoms nearest to the oxygen defect (in site-5) and their oxygen apical neighbors reduce by only 0-2 %, from $\sim$2.44 Å to $\sim$2.38 Å, whereas the corresponding changes of the Zn-O distances in $InGaZnO_4$ are 3-4 %. The planar Zn-O distances in $InAlZnO_4$ (2.02–2.21 Å) are also larger than the corresponding Zn-O distances in $InGaZnO_4$ (1.99–2.13 Å) or the planar Zn-O distances in wurtzite ZnO (1.97 Å). We believe that the motion of Zn atoms in oxygen deficient $InAlZnO_4$ is restricted due to the stronger Al-O bonds present in the $AlZnO_{2.5}$ layer.

Comparing the relaxation of Al atoms in $InAlZnO_4$ and $InAlCaO_4$ with the oxygen vacancy at site-1, we observe a similar tendency: in the former, the Al pulls its nearest oxygen atoms closer to itself so that all four Al-O distances become nearly identical (changing from 1.87–1.96 Å to 1.80–1.82 Å) with the largest distance change of 8 %, whereas in $InAlCaO_4$, all four Al-O distances are essentially unchanged upon introduction of the defect having the largest relaxation of only 0.4 %. Therefore, we can conclude that the presence of the metal atoms which form stronger bonds with the oxygen neighbors restricts the motion of the metals with weaker oxygen bonds. As a result, the latter cations are unable to form a preferred coordination and/or relax to the desired metal-oxygen distances and are forced to remain in a highly anisotropic oxygen environment upon introduction of a oxygen vacancy. This leads to a high formation energy of the defect. Indeed, the formation of strong directional bonds due to significant contribution from the metal p orbitals near the oxygen vacancy defect in Al_2O_3, CaO, and MgO, [19] was shown to be the reason for the strong electron localization near the vacancy in these binary light-metal oxides. In contrast, when the multicomponent oxide consists of a low-formation oxide constituents, as in the case of $InGaZnO_4$, the weakly-bonded lattice may allow for a significant atomic relaxation, hence, leading to an energy gain due to the formation of more stable structures, and thus a more uniform defect distribution throughout the lattice (c.f., Fig. 4.3).

4.3.5. Conductivity Estimates in Oxygen Deficient InAMO$_4$. In Section 4.3.2 above, we showed that under the extreme metal-rich conditions, the considered three representative InAMO$_4$ compounds have nearly identical formation energy of the oxygen vacancy in the $InO_{1.5}$ layer, Table 4.2, suggesting that similar concentrations of the oxygen defect may be achieved in these compounds, Fig. 4.3. However, apart from the formation of other possible acceptor and donor defects to be discussed elsewhere [83], one also needs to take into account the electron mobility which determines the resulting conductivity along with the carrier concentration. Specifically,

the conductivity σ depends on both, the electron group velocity and the density of states near the Fermi level, according to:

$$\sigma = \frac{2e^2}{\Omega} \sum_{k\lambda} |v_{k\lambda}|^2 \tau_{k\lambda} \delta(E_{k\lambda} - E_F).$$ (4.12)

Here e is the electron charge, Ω – the volume of the Brillouin zone, k – the wave vector, λ – the band index, v – the electron group velocity, $\tau(\epsilon)$ – the relaxation time, and E_F is the Fermi energy. Based on our calculations, we can estimate the band-structure conductivity factor – the square of the electron velocity multiplied by the density of states in the vicinity of the Fermi level – and compare the results for the three compounds under consideration, Table. 4.4 . The electron relaxation time can be roughly assumed to be of the same order for the oxides with similar defect concentrations.

Table 4.4: Electronic properties of InAMO$_4$ compounds with ionized oxygen vacancy, V$_O^+$, which corresponds to the conducting state: Defect carrier concentrations used in the supercell calculations; the electron group velocities calculated at the Fermi level for the [001] crystallographic direction; density of states (DOS) at the Fermi level; and normalized band-structure conductivity factor calculated as the square of the electron velocity multiplied by the density of states at the Fermi level.

	InGaZnO$_4$	InAlZnO$_4$	InAlCaO$_4$
Defect concentration, 10^{21}cm^{-3}	1.75	1.72	1.63
Electron velocity, v$^{[001]}$, 10^5 m/s	6.47	4.09	3.46
Density of states at E$_F$, states/eV·cell	3.7	7.0	7.6
Normalized σ-factor, v^2·DOS(E$_F$)	1.00	0.76	0.59

The electron group velocities and density of states (DOS) are calculated for the oxygen deficient InAMO$_4$ with ionized oxygen vacancy, V_O^+ which corresponds to the conducting state, Table. 4.4 [19, 44]. We find that the electron velocities differ for the three compounds: we obtain 6.47×10^5 m/s, 4.09×10^5 m/s, and 3.46×10^5

m/s in InGaZnO$_4$, InAlZnO$_4$, and InAlCaO$_4$, respectively, with the oxygen vacancy located at the most preferred site. However, the density of states near the Fermi level increases in the same order, i.e., as the number of the light metal constituents increases. The larger DOS(E$_F$) indicates a decrease in the energy dispersion of the conduction band associated with stronger electron localization, as expected from the comparative investigations of oxygen deficient binary oxides, Table. 4.4 [15].

As a result, despite a possibility for similar defect concentrations in InAMO$_4$ compounds with oxygen vacancies assumed to be the major donor defects, the conductivity estimated from the electronic band structure is expected to be two times smaller in InAlCaO$_4$ as compared to InGaZnO$_4$, whereas InAlZnO$_4$ falls in between the values of the two oxides above.

4.4. CONCLUSIONS

We have investigated the oxygen vacancy formation in three representative multicomponent InAMO$_4$ compounds with none, one and two light metal constituents. Although we find that the oxygen defect prefers to be located in the InO$_{1.5}$ layer for all three InAMO$_4$ materials which correlates well with the heat of formation of the corresponding binary oxides, we obtain a significant reduction in the defect formation energy due to a large atomic relaxation near the defect and the formation of stable fourfold structures for Zn, Al, and Ga atoms. This additional energy gain results in a more uniform distribution of the oxygen defect throughout the layered structure of InGaZnO$_4$ and InAlZnO$_4$. We believe that a similar behavior may be expected for the multicomponent oxides which consist of the cations with relatively weak metal-oxygen bonds, e.g., CdO with the heat of formation of ΔH_f=–2.69 eV, SnO$_2$ with ΔH_f=–6.02 eV, and GeO$_2$ with ΔH_f=–5.59 eV, to allow for an appreciable atomic relaxation in the lattice in order to achieve the desired local structure characteristics (i.e., metal-oxygen distances and coordination). The latter two oxides are also

appealing because the Ge and Sn cations can exist in both fourfold and sixfold coordinations, therefore, they are more likely to adjust to anisotropic oxygen environment associated with the formation of oxygen defects.

Acknowledgements

5. NATIVE POINT DEFECTS IN MULTICOMPONENT TRANSPARENT CONDUCTING OXIDE HOSTS

Altynbek Murat[1] and Julia E. Medvedeva[1]

[1]*Department of Physics, Missouri University of Science & Technology,*

Rolla, MO 65409, USA

ABSTRACT[*]

The formation of native point defects in layered multicomponent InAMO$_4$ oxides with A^{3+}=Al or Ga, and M^{2+}=Ca or Zn, is investigated using first-principles density functional calculations. We calculated the formation energy of acceptor (cation vacancies, acceptor antisites) and donor (oxygen vacancies, donor antisites) defects within the structurally and chemically distinct layers of InAMO$_4$ oxides. We find that the antisite defects, in particular, the A atom substituted on M atom site (A_M) in InAMO$_4$ oxides, have lower formation energies, hence, higher concentrations, as compared to those of the oxygen vacancies (V_O) which are major donor defects in binary constituent oxides. Furthermore, the cation vacancies (V_{In}, V_A, and V_M) have low formation energies in InAMO$_4$ oxides associated with the large structural relaxations around the defect. As a result, the equilibrium Fermi level is pushed away from the conduction band bottom deeper into the band gap. The results not only agree with the observed dependence of the conductivity on the oxygen partial pressure in InGaZnO$_4$, but also explain why the InAlZnO$_4$ samples were unstable under a wide range of growing conditions.

---

[*]In final preparation for submission to Physical Review B.

5.1. INTRODUCTION

Multicomponent transparent conducting oxides (TCOs) [1, 5, 31, 37, 68] with the composition of both post-transition metals (In, Ga, and Zn) and main-group light-metals (Al, Mg, and Ca) are highly attractive since the presence of main-group light-metal cations help stabilize the multi-cation structure, allow for a broader optical transmission window due to a larger band gap, and also help control the carrier content while preserving the carrier mobility [3].

The carrier generation mechanism in multicomponent TCOs is a subject of active debates [9, 19, 26, 35]. For example, the free carriers in $InGaO_3(ZnO)$ are believed to be due to the formation of oxygen vacancy defects [9, 35]. However, based on the first-principles investigations, it was shown that the oxygen vacancies are deep donors and can not explain the observed conductivities in these materials [19, 46].

Recently, electronic band structure of undoped stoichiometric as well as oxygen deficient $InAMO_4$ compounds with A^{3+}=Al or Ga, and M^{2+}=Ca or Zn, [11] have been systematically investigated from first-principles [16, 30]. The results of undoped stoichiometric materials showed that the electronic properties of these layered-structured multicomponent oxides resemble those in the conventional binary TCOs: both exhibit a dispersed s-like conduction band and possess a small (0.3–0.5 m_e), isotropic electron effective mass. Strikingly, it was found that despite the different band gaps of the constituent binary oxides (2–4 eV In_2O_3 or ZnO; 5 eV for Ga_2O_3; and 7–9 eV in CaO or Al_2O_3), the s-states of *all* cations contribute to the bottom of the conduction band of the multicomponent oxide. Such a hybrid conduction band can be expected to provide a uniform network for the carrier transport within and across the chemically and structurally distinct layers of the $InAMO_4$ materials [30]. Moreover, the results of oxygen deficient $InAMO_4$ oxides showed that the chemical composition, the local atomic coordination, the atomic relaxation, and the metal-oxygen bond strengths strongly affect the formation and distribution of the oxygen

vacancy defects [16]. In fact, it was found that the concentration of the oxygen va-
cancy defect is suppressed due to the presence of the light-metal oxide constituents.

In order to understand the carrier generation mechanisms in multicomponent
oxides and make conclusions about the origins of the conductivity, other possible
native point defects in InAMO_4 must be studied. In this work, we systematically
calculate and compare the formation energies of possible native point defects at var-
ious locations within the $InO_{1.5}$ and $AMO_{2.5}$ layers of InAMO_4, Fig. 5.1. Structural
and chemical complexity of InAMO_4 compounds lead to several intrinsic donor and
acceptor defects which can coexist. Thus, our investigation of native point defects
include both the donor (anion vacancies, donor antisites) defects and acceptor (cation
vacancies, acceptor antisites) defects. By taking into account the compensation mech-
anism involved within these native defects, we compare the formation energies of
electron donors as well as electron killers, to predict and calculate the most stable
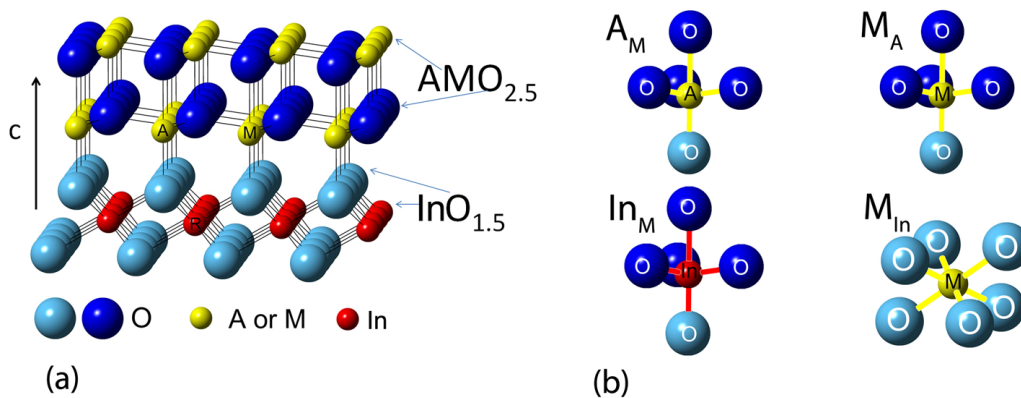donor defect which can produce free carriers.

Figure 5.1: (a) (Color online) Crystal structure of InAMO_4, specifically, one of the
three similar blocks which construct the conventional unit cell when
stacked along the z direction, is shown. (b) Four structurally different
possible antisite defects with different nearest-neighboring atoms in the
layered multicomponent InAMO_4 oxides.

5.2. APPROACH

Ab-initio full-potential linearized augmented plane wave method (FLAPW) [20, 47] within the local density approximation is employed for the investigation of the defect formation energies and the electronic properties of InAMO$_4$ oxides (A^{3+}=Al or Ga and M^{2+}=Ca or Zn). Cutoffs for the basis functions, 16.0 Ry, and the potential representation, 81.0 Ry, and expansion in terms of spherical harmonics with $\ell \leq$ 8 inside the muffin-tin spheres were used. The muffin-tin radii of multicomponent oxides are as follows: 2.3 to 2.6 a.u. for In and Ca; 1.7 to 2.1 a.u. for Ga, Zn, and Al; and 1.45 to 1.8 a.u. for O atoms. Summations over the Brillouin zone were carried out using at least 23 special $\mathbf{k}$ points in the irreducible wedge.

The investigated InAMO$_4$ oxides have rhombohedral $R\bar{3}m$ layered crystal structure of YbFe$_2$O$_4$ type, Fig. 5.1(a) [74, 75, 80]. In these compounds, In^{3+} ions have octahedral coordination with the oxygen atoms and reside in 3(a) position (Yb), whereas both A^{3+} (Al or Ga) and M^{2+} (Ca or Zn) ions reside in 6(c) position (Fe), Fig. 5.1, and are distributed randomly [81]. Because of the different ionic radii and the valence state of the cations in the AMO$_{2.5}$ double layer, the A^{3+} and M^{2+} atoms have different z component of the internal site position 6(c). The optimized structural parameters for every structure under consideration can be found in our previous work [30].

To model isolated point defects in the InAMO$_4$ compounds, a 49-atom super-cell was used with the lattice vectors $(30\bar{2})$, $(\bar{1}12)$, and $(02\bar{1})$, given in the units of the rhombohedral primitive cell vectors [36]. Note that the conventional rhombohedral unit cell of YbFe$_2$O$_4$ contains 21 atoms (Z=3), and the primitive, i.e., the smallest volume, cell contains 7 atoms (Z=1). These supercells result in similar defect concentrations, namely, 1.6–1.8×10^{21}cm^{-3}, and, hence, similar distances between the defects $\sim$ 10Å. We stress that such high concentrations may not be experimentally feasible in all materials under consideration. However, our goal is to determine and

compare the properties of defect formations under the same conditions. The values of the defect formation energies calculated for the given supercells, can be used to predict the temperature-dependent defect densities in each compound, and are known to provide reasonable results [42, 44].

As mentioned above, the layered crystal structure of $InAMO_4$ oxides has two chemically and structurally distinct layers, $AMO_{2.5}$ and $InO_{1.5}$, which alternate along the [0001] direction. In particular, depending on the layer and the different nearest-neighbor coordination, there are several structurally different sites for the native point defects. As an example, Figure 5.1-(b) shows four possible antisite defect locations (A_M, In_M, M_A, and M_{In}), considered for the $InAMO_4$ oxides. Here, A_M means A replacing the M lattice site.

The formation energy of a defect in any charge state modeled using a corresponding background charge, can be calculated as a function of the Fermi level and the corresponding chemical potential:

$$\Delta H(E_F, \mu) = E_{defect} - E_{host} \pm \mu_\alpha + q(E_F) \qquad (5.1)$$

where E_{defect} and E_{host} are the total energies for the oxide with the defect and the stoichiometric oxide in the same-size supercell, respectively; μ_α is the chemical potential of atom α ($\alpha = In$, A, M, and O) added to (−) or removed from (+) the lattice; q is the defect charge state, E_F is the Fermi energy taken with respect to the top of the valence band. The chemical potential $\mu_\alpha = \mu_\alpha^0 + \Delta\mu_\alpha$ is taken with respect to the chemical potential μ_α^0 of the elementary metals or the O_2 molecule, whereas $\Delta\mu_\alpha$ is the deviation from the elemental chemical potential which is determined by the specific growth conditions which depend on the temperature and oxygen partial pressure [42].

In this work, with the purpose of reasonable comparison with the experimental growth conditions, we consider two different oxygen partial pressures, oxygen-rich and

oxygen-poor. In the oxygen-rich conditions, the oxygen partial pressure pO_2 is set to 1 atm whereas for the oxygen-poor conditions, $pO_2=0.0001$ atm. For both of these O-rich and O-poor conditions, $\Delta\mu_\alpha$ depends on the respective values of the heat of formation, $\Delta H_f[InAMO]$, as well as on $\Delta\mu_{In}$, $\Delta\mu_A$, $\Delta\mu_M$, and $\Delta\mu_O$, which are calculated from the following thermodynamic stability conditions:

(1) In order to maintain a stable $InAMO_4$ host, the elemental chemical potentials should have the values that require

$$\Delta\mu_{In} + \Delta\mu_A + \Delta\mu_M + 4\Delta\mu_O = \Delta H_f[InAMO_4] \tag{5.2}$$

(2) To avoid the precipitation of the elements In, A, M, and O, the following conditions must be satisfied:

$$\Delta\mu_{In} \leq 0; \Delta\mu_A \leq 0; \Delta\mu_M \leq 0; \Delta\mu_O \leq 0 \tag{5.3}$$

(3) To avoid the formation of the binary compounds, such as In_2O_3, A_2O_3, or MO, the following conditions must be fulfilled:

$$2\Delta\mu_{In} + 3\Delta\mu_O \leq \Delta H_f(In_2O_3) \tag{5.4}$$

$$2\Delta\mu_A + 3\Delta\mu_O \leq \Delta H_f(A_2O_3) \tag{5.5}$$

$$\Delta\mu_M + \Delta\mu_O \leq \Delta H_f(MO) \tag{5.6}$$

Thus, the available range for the elemental chemical potentials in the case of quaternary $InAMO_4$ materials is a three-dimensional volume determined by the above stability conditions (equations 5.3– 5.6), projected onto the corresponding $InAMO_4$ surface plane (equation 5.2).

The heat of formation, ΔH_f, for the oxides is calculated with respect to the bulk orthorhombic Ga, tetragonal In, hexagonal Zn, and cubic Al or Ca. Our obtained ΔH_f values for the three representative $InGaZnO_4$, $InAlZnO_4$, and $InAlCaO_4$ compounds are –11.28 eV, –14.60 eV, and –15.40 eV, respectively. Calculating the corresponding heat of formation for the binary constituents, we find that:

$$2\Delta H_f[InGaZnO_4] > \Delta H_f(In_2O_3) + \Delta H_f(Ga_2O_3) + 2\Delta H_f(ZnO) \tag{5.7}$$

$$2\Delta H_f[InAlCaO_4] > \Delta H_f(In_2O_3) + \Delta H_f(Al_2O_3) + 2\Delta H_f(CaO) \tag{5.8}$$

$$2\Delta H_f[InAlZnO_4] < \Delta H_f(In_2O_3) + \Delta H_f(Al_2O_3) + 2\Delta H_f(ZnO) \tag{5.9}$$

The equations 5.7 and 5.8 suggest that at zero temperature, the formation of $InGaZnO_4$ or $InAlCaO_4$ is impossible without the formation of the corresponding binary phases. This also means that there is no available elemental chemical potentials which would allow the formation of the corresponding multicomponent oxides. Since the latter are stable above 1000 K [74, 75, 80], the entropy term $T\Delta S$ must be taken into consideration. Similar arguments were reported for $In_2O_3(ZnO)_k$ compounds [82]. The entropy term can be estimated based on the corresponding equilibrium solid state reactions which involve the binary constituents as follows:

$$\Delta H_f[InGaZnO_4] - 1/2[\Delta H_f(In_2O_3) + \Delta H_f(Ga_2O_3) + 2\Delta H_f(ZnO)]$$
$$= T_{InGaZnO_4} \times \delta S_{InGaZnO_4} \tag{5.10}$$

$$\Delta H_f[InAlCaO_4] - 1/2[\Delta H_f(In_2O_3) + \Delta H_f(Al_2O_3) + 2\Delta H_f(CaO)]$$
$$= T_{InAlCaO_4} \times \delta S_{InAlCaO_4} \tag{5.11}$$

We then replace the ΔH_f for $InGaZnO_4$ and $InAlCaO_4$ with the corresponding $[\Delta H_f - T \times \delta S]$, in the equation 5.2 above. As a result, as we have shown before [16], the available chemical potentials for metals in $InGaZnO_4$, $InAlZnO_4$, and

InAlCaO$_4$, correspond to a very narrow range along the crossing line of the three planes, eqs. 5.4-5.6. This is in accord with the results for Ga-free layered multicomponent In$_2$O$_3$(ZnO)$_3$ which was shown to exist without the occurrence of the secondary phases only for a constant ratio between indium and zinc [82].

Our obtained chemical potential values for the three representative InGaZnO$_4$, InAlZnO$_4$, and InAlCaO$_4$ compounds in oxygen-rich (pO_2=1 atm) and oxygen-poor (pO_2=0.0001 atm) conditions are shown in Table 5.1.

Table 5.1: Calculated chemical potential values ($\Delta\mu$) for the O-rich (pO_2=1 atm) and O-poor/M-rich (pO_2=0.0001 atm) conditions for the InAMO$_4$ oxides, in eV.

InAMO$_4$	Oxygen-rich				Oxygen-poor			
	$\Delta\mu_{In}$	$\Delta\mu_A$	$\Delta\mu_M$	$\Delta\mu_O$	$\Delta\mu_{In}$	$\Delta\mu_A$	$\Delta\mu_M$	$\Delta\mu_O$
InGaZnO$_4$	-2.4	-2.5	-2.3	-1.1	-1.8	-1.9	-1.9	-1.5
InAlZnO$_4$	-2.2	-5.1	-2.2	-1.2	-1.5	-4.4	-1.7	-1.7
InAlCaO$_4$	-2.0	-4.9	-4.6	-1.4	-1.3	-4.2	-4.1	-1.9

5.3. RESULTS AND DISCUSSION

The formation of native point defects is investigated in the three representative multicomponent InAMO$_4$ compounds with none, one, and two light-metal constituents. In the following sections, we discuss the role of chemical compositions, atomic coordinations, and metal-oxygen bond strengths in the formation and stability of native point defects in InAMO$_4$.

5.3.1. Formation of Antisite Defects in InAMO$_4$. First, we investigate the formation of antisite defects (cation disorder) in the three representative InAMO$_4$ oxides, i.e., InGaZnO$_4$, InAlZnO$_4$, and InAlCaO$_4$. In addition to the intrinsic cation/anion vacancies, there are several possible antisite defects including

both the n-type (donor) and the p-type (acceptor) defects within the layered structure of InAMO$_4$ with In^{3+}, A^{3+}, and M^{2+}. We consider 4 possible antisites which are In_M, A_M (donor antisites) and M_{In}, M_A (acceptor antisites), Fig. 5.1. Our calculated formation energies for the considered antisite defects in InAMO$_4$ oxides, for both oxygen-rich and oxygen-poor conditions are plotted in Fig. 5.2, as a function of the Fermi level. It should be noted that the oxygen vacancy formations which were reported earlier (see Section 4) are included in these plots to show the similar oxygen vacancy formation energies, hence, similar concentration levels among the InAMO$_4$ oxides.

In InGaZnO$_4$, under the oxygen-rich (metal-poor) conditions as shown in Figure 5.2-(a), the donor antisites Ga$_{Zn}$ and In$_{Zn}$ have lower formation energies than the acceptor antisites Zn$_{Ga}$ and Zn$_{In}$ and oxygen vacancy V$_O$. In particular, among the antisites, when the Fermi level is lower than 2.6 eV, the donor Ga$_{Zn}$ antisite defect has the lowest formation energy among all other defects considered, and, hence, is expected to be the major electron donor defect. However, when the Fermi level is above 2.6 eV, the acceptor antisites become more stable with lower formation energies than the donor antisites. Thus, in O-rich conditions, when the Fermi level is above 2.6 eV, the acceptor antisites (electron killers) compensate the donor antisites, hence no free carriers will be produced. One way to control this compensation of electron donor antisites is by controlling the oxygen partial pressure which will change the chemical potential of the oxygen, hence the chemical potentials of the cations, based on the equation 5.2. In Figure 5.2-(b), we decrease the oxygen partial pressure from 1 atm (O-rich) to 0.0001 atm (O-poor), which decreases the chemical potential of oxygen while increasing the chemical potentials of metals, equation. 5.2. The obtained chemical potential values for the different oxygen partial pressures are presented in Table 5.1. We note that if the oxygen partial pressure is decreased below 0.0001 atm, the formation energy of donor antisites becomes unphysically negative, which
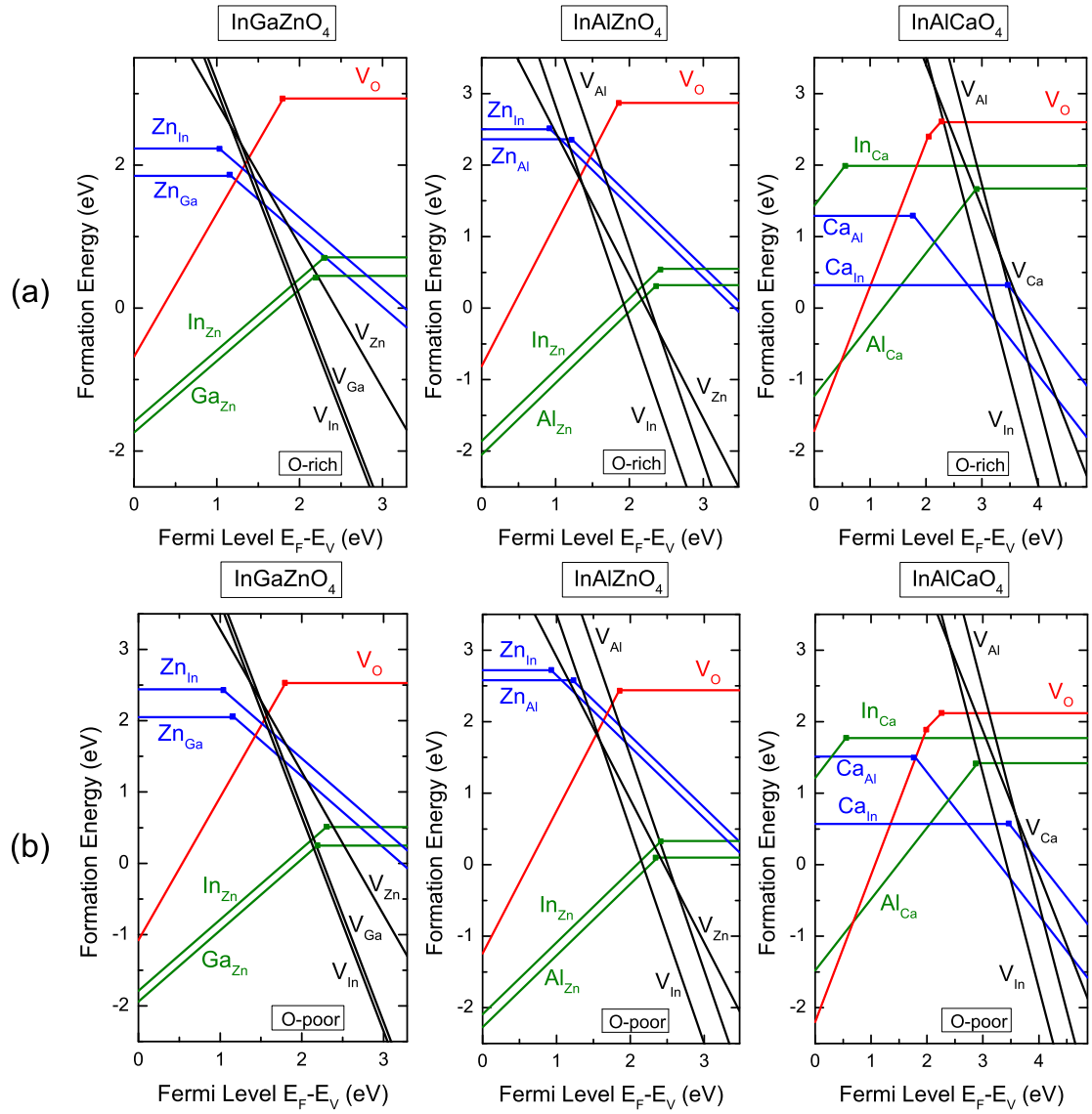
Figure 5.2: (Color online) (**a**) Formation energies of native point defects in InGaZnO$_4$, InAlZnO$_4$, and InAlCaO$_4$ for O-rich condition, i.e., pO$_2$=1 atm. (**b**) Formation energies of native point defects for O-poor conditions, i.e., pO$_2$=0.0001 atm, in InGaZnO$_4$, InAlZnO$_4$, and InAlCaO$_4$. Calculated band gaps [30] are used which are 3.29 eV, 3.48 eV, and 4.87 eV, for InGaZnO$_4$, InAlZnO$_4$, and InAlCaO$_4$, respectively. The temperatures used are 1023 K, 1123 K, and 1223 K for InGaZnO$_4$, InAlZnO$_4$, and InAlCaO$_4$, respectively. The solid squares represent the transition points in each defect.

may indicate that the compound becomes unstable under this conditions (pressure of 0.0001 atm and temperature of $\approx$1000 K) due to the abundance of antisite defects. As a result of decreasing the oxygen partial pressure, the order of the formation energies of antisite defects do not change, the lowest donor antisite is still Ga$_{Zn}$. However, it can be seen from Figure 5.2-(b), the formation energies of the acceptor antisites have increased whereas the formation energies of the donor antisites have decreased. Thus, in O-poor conditions, the Fermi level where the acceptor antisites compensate the donor antisites has increased from 2.6 eV to 3 eV, hence, increasing the dopability range, Figure 5.2-(b). This also means that the equilibrium Fermi level is more closer to the conduction band minimum in O-poor conditions (note, that the band gap of InGaZnO$_4$ is 3.3 eV at room temperature and about 3.1 eV at T=1000 K). However, this equilibrium Fermi level will be changed when the cation vacancies are introduced (as discussed below).

Similarly, in InAlZnO$_4$, the donor antisites Al$_{Zn}$ and In$_{Zn}$ have lower formation energies than the acceptor antisites Zn$_{Al}$ and Zn$_{In}$. The most stable defect with the lowest formation energy is the donor Al$_{Zn}$ antisite defect whereas the acceptor antisite defect Zn_{In} has the highest formation energy. In O-rich condition, the donor antisite defect Al$_{Zn}$ is only stable when the Fermi level lies below 3.1 eV, otherwise it is compensated by the acceptor antisites Zn$_{In}$ or Zn$_{Al}$, Fig. 5.2-(a). Similar to InGaZnO$_4$, to avoid compensation, we have decreased the oxygen partial pressure to 0.0001 atm, Fig. 5.2-(b). As a result, the formation energies of acceptor defects have increased while the formation energy of the donor antisite Al$_{Zn}$ has decreased. Thus, it can be seen from Fig. 5.2-(b), the Al$_{Zn}$ donor antisite is the most stable defect with the lowest formation energy up to the conduction band edge, i.e., no charge compensation of the donor antisite Al$_{Zn}$ by acceptor antisites will occur under the O-poor conditions at T=1123 K.

In the case of InAlCaO$_4$, the formation of antisite defects differs significantly from those in InGaZnO$_4$ and InAlZnO$_4$. We find that the donor antisite In_{Ca} has higher formation energy than both acceptor antisites Ca_{Al} and Ca_{In}. The donor antisite Al_{Ca} is the most stable defect with the lowest formation energy when the Fermi level lies below 1.55 eV, in O-rich condition. When the Fermi level is higher than 1.55 eV, the donor Al_{Ca} is compensated by the acceptor antisites. As we did for InGaZnO$_4$ and InAlZnO$_4$, to increase the formation energies of acceptor antisites, we have decreased the oxygen partial pressure to 0.0001 atm. Again, no change in the trend of the formation energies of the antisites occur. As expected, the formation energies of the acceptor antisite defects have increased while the formation energies of the donor antisites have decreased in the O-poor condition. This change increased the Fermi level where Al_{Ca} is compensated by the acceptor defects, to 2.1 eV, Fig. 5.2-(b). Unlike the case of InGaZnO$_4$ and InAlZnO$_4$ where the formation energy of the most stable donor antisites get very close to zero, the formation energies of antisites in InAlCaO$_4$ are higher by at least 1.5 eV. Hence, the partial pressure could be decreased below 0.0001 atm, which might increase the formation energies of the acceptor defects further. However, even at extreme possible O-poor conditions (with oxygen partial pressure of $pO_2 = 1 \times 10^{-11} atm$) as shown in Figure 5.3, the compensation of the donor antisite Al_{Ca} by the acceptor antisites still occurs when the Fermi level lies above 2.8 eV which is 2 eV below the conduction band minimum in InAlCaO$_4$.

The donor antisite defects produce free carriers at their neutral charge states, the horizontal lines in Figure 5.2. Thus, it can be seen that the most stable donor antisite defects Ga_{Zn} and Al_{Zn} in InGaZnO$_4$ and InAlZnO$_4$, respectively, expected to result in similar high defect concentrations due to their similar formation energies, both in O-poor and O-rich conditions. In contrast, due to the high formation energy of the most stable donor antisite Al_{Ca} in InAlCaO$_4$, the defect concentrations are expected to be much lower. We stress again that, in addition to the acceptor antisites,
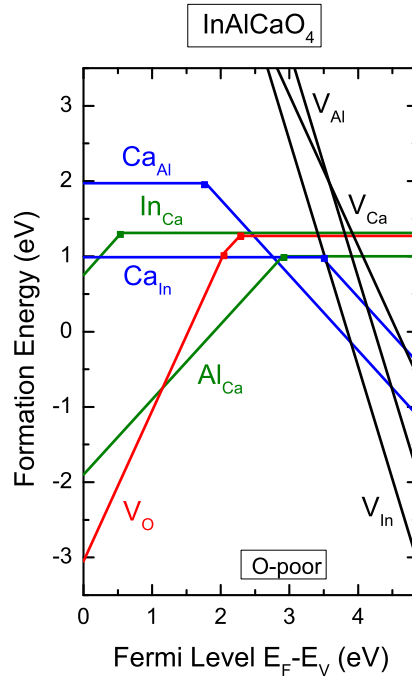
Figure 5.3: (Color online) Formation energies of native point defects for extreme O-poor condition, i.e., $\Delta\mu_O = 1/4[\Delta H_f[InAMO_4] - \sum \Delta\mu_{metal}^{M-rich}] = -2.71$ eV, in InAlCaO$_4$. $\Delta\mu_O = -2.71$ eV is equivalent to oxygen pressure of $pO_2 = 1 \times 10^{-11} atm$.

the cation vacancies also contribute to the charge compensation mechanism as well as to the equilibrium defect concentrations, and will be discussed in Section 5.3.3.

5.3.2. The Trend of Antisite Defect Formation Energies in InAMO_4. Here, we discuss the trend of formation energies of the antisite defects within and among the three representative InAMO_4 oxides. We find that the formation energies of the antisite defects correlate well with the experimental heat of formation of the corresponding constituent binary oxides.

The experimental heat of formation of binary oxides per oxygen are in the following order: In$_2$O$_3$ (–3.21 eV) >ZnO (–3.60 eV) >Ga$_2$O$_3$ (–3.73 eV) >Al$_2$O$_3$ (–5.78 eV) >CaO (–6.57 eV), i.e., In-O bonds correspond to the set of the metal-oxygen bonds that would be the easiest to break compared to Ca-O bonds. Table 5.2 shows how the metal-oxygen distances change upon the creation of the corresponding

Table 5.2: The average distance between the defect site and its nearest planar O atoms, $\langle D_{ab}\rangle$, the distances between the defect site and the nearest apical O atom, D_c, and the next nearest apical O atom, D_c^*, in Å, are given for stoichiometric InAMO$_4$ and those with antisite defects specified.

		InGaZnO$_4$			InAlZnO$_4$			InAlCaO$_4$		
		$\langle D_{ab}\rangle$	D_c	D_c^*	$\langle D_{ab}\rangle$	D_c	D_c^*	$\langle D_{ab}\rangle$	D_c	D_c^*
No defect	In-O	2.21			2.21			2.20		
	A-O	1.88	1.92	2.35	1.84	1.84	2.14	1.77	1.78	2.17
	M-O	1.98	1.97	2.38	2.05	2.00	2.38	2.20	2.20	2.60
In_M	In-O	2.05	2.09	2.29	2.11	2.09	2.29	2.18	2.13	2.48
A_M	A-O	1.90	1.97	2.14	1.88	1.86	2.30	1.85	1.80	2.80
M_A	M-O	1.97	2.04	2.25	2.03	2.12	2.05	2.17	2.25	2.24
M_{In}	M-O	2.17			2.21			2.33		

antisite defect. For example, we compare the original Ga-O distances to the respective ones when In occupies the Ga site to study how the distances changed. As expected, we find upon introduction of the antisite, the original metal-oxygen distances change to those that resemble the metal-oxygen distances of the cation that replaces the original site. For example, for the donor antisite In_{Zn}, the original Zn-O distances were 1.98Å($\langle D_{ab}\rangle$- average planar distances), 1.97Å(D_c-nearest apical distance), and 2.38Å(D_c^*-next nearest apical distance). At the same time the original average In-O distances were 2.21Å. When In replaces the Zn site, we found two behaviors. First, as expected, the In_{Zn}-O distances increase to resemble the original In-O distances. As a result, the new In_{Zn}-O distances are 2.05Å, 2.09Å, and 2.29Å. As we can see, the average planar distances and nearest apical distances are very close, i.e., they have decreased from 2.21 to 2.05 and 2.09Å. However, the opposite has happened to the next nearest apical distances. The next nearest apical distances have increased rather than decreased. Second, we find that, for the oxides that are in fourfold coordination with oxygen in their ground state, when the 3 planar and 1 nearest

apical distances become very close to their distances in ground state, they prefer to form fourfold coordination with O. This can be seen in the percent change in distances as summarized in Table 5.3.

Table 5.3: Upon the atomic relaxation caused by the corresponding antisite defects, the average change in the distance between the defect site and its nearest planar O atoms, $\langle D_{ab} \rangle$, the nearest apical O atom, D_c, and the next nearest apical O atom, D_c^*, in percent, are given.

$\mathrm{In}AMO_4$	InGaZnO$_4$			InAlZnO$_4$			InAlCaO$_4$		
	$\langle D_{ab} \rangle$	D_c	D_c^*	$\langle D_{ab} \rangle$	D_c	D_c^*	$\langle D_{ab} \rangle$	D_c	D_c^*
In_M	+5	+4	-4	+3	+4	-4	-3	-5	+2
A_M	-0.1	-0.2	+0.4	-8	-7	-4	-17	-20	+15
M_A	+4	+3	+5	+8	+8	+4	+17	+19	+12
M_{In}	-1			-0.4			+6		

Now, the trend of formation energies of antisite defects can be explained based on both the experimental heat of formation of binary oxides as well as the change in the metal-oxygen distances. The trends can be clearly seen from Tables 5.2 and 5.3. For example, in InGaZnO$_4$, the reason why the donor antisite Ga$_{Zn}$ has lower formation energy compared to In$_{Zn}$ is that the creation of stronger bond such as Ga-O is preferred over the In-O one, as follows from the relative heat of formation of the corresponding binary oxides, and also due to the Ga preference to have fourfold oxygen coordination. The reason why Zn_{In} have higher formation energy as compared to Zn$_{Ga}$ is due to the fact that the structure with six-coordinated Zn (rocksalt ZnO) is unstable. Similarly, in InAlZnO$_4$ and InAlCaO$_4$, the antisites Al$_M$ are more likely to form as compared to In$_M$ antisites due to the energy gain associated with the formation of strong Al-O bonds. The formation energy of Zn$_{In}$ is higher than the one for Zn$_{Al}$ due to the aforementioned preference of Zn for five rather than six-coordinated

sites, whereas for Ca this trend is reversed: in the ground state phase, CaO is octahedrally coordinated (rocksalt structure), hence, Ca_{In} is more likely to occur than Ca_{Al}.

Moreover, it can be seen from Table 5.3, in addition to the cations preference to form stable structures, the relaxation due to the change in the distances between the defect and nearest atoms increase with the number of light-metal constituents. For example, the average percent change in the distances for M_A antisite defect in InAlCaO$_4$ is twice larger than the average change in distances in InAlZnO$_4$ and almost three times larger than the ones in InGaZnO$_4$, Table 5.3.

5.3.3. Formation of Cation Vacancies in InAMO$_4$. In addition to the acceptor antisites, the cation vacancies also contribute to the charge compensation of the donor defects, thus, affecting the equilibrium Fermi level and the total defect concentrations. Here, we discuss the formation energies of the cation vacancies in InGaZnO$_4$, InAlZnO$_4$, and InAlCaO$_4$. In InAMO$_4$ oxides, V$_{In}$, V_A, and V_M vacancies can occur. Our calculated formation energies for the respective vacancies are shown in Figure 5.2. First, we note that the formation energies of the cation vacancies show some correlation with the experimental heat of formation of the constituent binary oxides, i.e., with the metal-oxygen bond strengths. Indeed, the formation of V$_{In}$ is more likely than that of V$_{Al}$ (especially, in InAlCaO$_4$), and the formation of V$_{Zn}$ is lower than that of V$_{Ca}$. However, the respective formation energies are significantly affected by the large structural relaxation around the vacancy defects. The latter appears due to the presence of several cations of different ionic size, valence, metal-oxygen bond strength, and oxygen coordination near each defect. Indeed, a larger atomic relaxation around V$_{In}$ is found in InGaZnO$_4$ (10–17%) as compared to that in In$_2$O$_3$ (5–12%).

As a result, the cation vacancies in InAMO$_4$ result in much lower formation energies than the formation of cation vacancies in the constituent binary oxides [44].

These lead to the charge compensation of the donor antisites at the Fermi levels lower than the acceptor antisites. Figure 5.2 shows the formation energies of the cation vacancies for the O-rich and O-poor conditions. As it can be seen from Figure 5.2-(b), the cation vacancies are pushed up slightly as the oxygen pressure is decreased. The presence of cation vacancies will push the equilibrium Fermi level away from the conduction band bottom and into the band gap. This shows that the larger the number of the light-metal constituents, the harder it is to achieve a shallow donor.

5.3.4. Defect Concentrations in InAMO_4. Figure 5.4 shows the equilibrium defect concentrations plotted as a function of the oxygen partial pressures. The concentrations are calculated within the extreme possible oxygen partial pressure ranges. The highest defect concentrations in $InGaZnO_4$ is for Ga_{Zn} donor antisite and the highest defect concentrations in $InAlZnO_4$ is for Al_{Zn} donor antisite. However, as shown in Figure 5.4, the equilibrium concentration of Al_{Zn} antisite defect exceeds the maximum possible defect concentration, $n_{max} \approx 1.2 \times 10^{22} cm^{-3}$, in In$AMO_4$, which is determined as the number of possible sites for this defect in the supercell divided by the volume of the supercell. Hence, the equilibrium native point defect concentrations should not exceed the possible maximum concentration, n_{max}, as illustrated in Figure 5.4. Otherwise, the material will not be stable at this temperature. For the case of $InGaZnO_4$, the material is stable and the antisite defect Ga_{Zn} results in the highest defect concentrations (not exceeding the n_{max}) for up to $pO_2 = 1 \times 10^{-8} atm$ at T=1000 K. The resulting equilibrium electron concentration, calculated based on the charge neutrality condition in the lattice, is also plotted in Figure 5.4. For $InGaZnO_4$, the electron concentration follows the $Log(pO_2)^{-1/4}$ dependence. The same dependence is obtained for the observed dependence of conductivity σ on the pressure in $InGaZnO_4$ [86]. The results also explain why the $InAlZnO_4$ samples were unstable under a wide range of growing conditions due to the formation of cation metal phases [9].
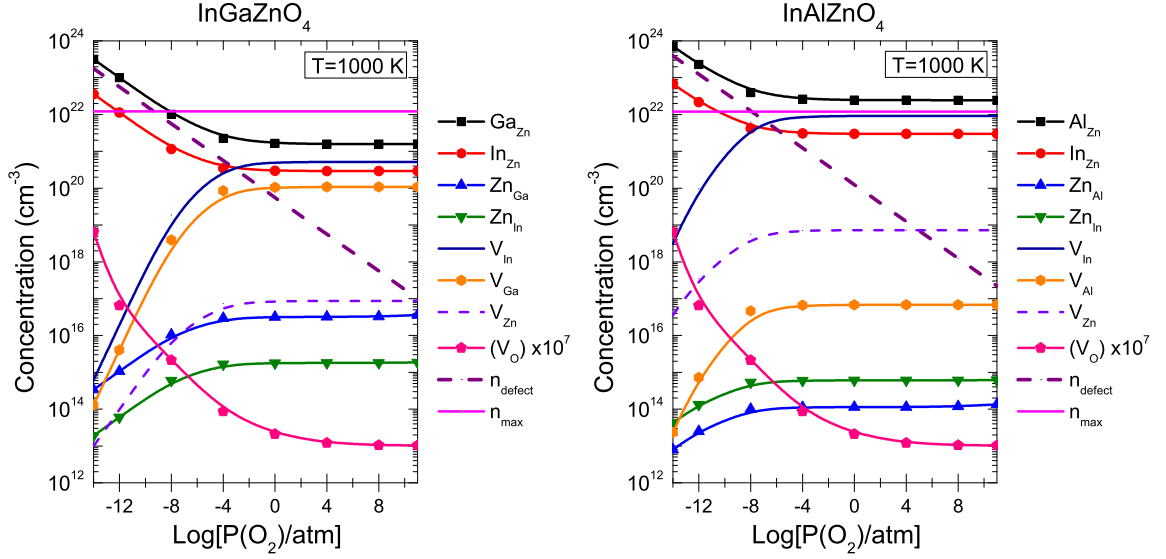
Figure 5.4: (Color online) Equilibrium defect concentrations plotted as a function of the oxygen partial pressure at 1000K temperature.

5.4. CONCLUSIONS

We have investigated the formation of native point defects in three representative multicomponent $InAMO_4$ compounds with none, one and two light metal constituents. We find that the donor antisite defect such as Ga_{Zn} in $InGaZnO_4$ has the lowest formation energies, hence, results in the highest defect concentrations, and can produce free carriers. The donor antisite defects have much lower formation energies compared to the oxygen vacancies which were believed to be the major donor defect in multicomponent oxides. In addition, we find that the formation energy of cation vacancies in $InAMO_4$ are much lower than the formation energy of the respective cation vacancies in binary TCOs. This agrees well with the large structural relaxation obtained around the defects in $InAMO_4$. As a result, the equilibrium Fermi level is affected by the presence of the cation vacancies and is 1.2–2.1 eV below the conduction band minimum (CBM) for the $InAMO_4$ oxides grown under the oxygen partial pressure of 0.0001 atm and temperature of 1000 K. Thus, the shift in equilibrium Fermi level increases with the number of the light-metal constituents. For

example, in InGaZnO$_4$ (without light-metal constituent), the equilibrium Fermi level is at 1.2 eV below CBM compared to 1.4 eV below CBM in InAlZnO$_4$ (with one light-metal constituent). However, in InAlCaO$_4$, in addition to the cation vacancies, the acceptor antisities also have low formation energies, hence the equilibrium Fermi level is very deep in the band-gap, at 2.1 eV, so that free carriers are not created. Overall, the obtained equilibrium carrier concentration is in excellent agreement with the observed dependence of the conductivity on the oxygen partial pressure in InGaZnO$_4$. The results also explain why the samples with light-metal constituents are unstable under a wide range of growing conditions, such as InAlZnO$_4$.

Acknowledgements

6. CONCLUSIONS

In conclusion, we have systematically investigated the structural, optical, and electronic properties of twelve undoped stoichiometric and nonstoichiometric complex multicomponent oxides with layered structure $RAMO_4$ [where R^{3+}=In or Sc, A^{3+}=Al or Ga, and M^{2+}=Ca, Cd, Mg, or Zn] using *ab-initio* full-potential linearized augmented plane wave method (FLAPW) based on density functional theory.

In Section 3, based on the results obtained from our electronic band structure calculations of the undoped stoichiometric $RAMO_4$ materials, we addressed two fundamental questions. First, we determined the role played by the local atomic coordination in the electronic properties such as the band gap, the electron effective mass, and the nature of the conduction band of $RAMO_4$. Second, we established how the optical properties and the available electron conduction paths in layered multicomponent oxide hosts vary with the chemical composition.

The compositional complexity of $RAMO_4$ leads to a wide range of band gap values varying from 2.45 eV for $InGaCdO_4$ to 6.29 eV for $ScAlMgO_4$ as obtained from our calculations. Most significantly, we demonstrated that the unusual fivefold coordination of the A^{3+} and M^{2+} metal atoms stabilized in $RAMO_4$ compounds, results in the electronic band structure of the complex oxides that differs from the one expected based on the electronic properties of the binary oxide constituents in their lowest-energy (ground state) phases. The unusual fivefold coordination of the A and M atoms in $RAMO_4$ compounds promotes a hybrid s-like conduction band composed from the s-states of *all* cations independent of the strength of the metal-oxygen interaction. As a result, an isotropic charge transport is possible in these layered materials.

Consistently, we find that in multicomponent oxides, all oxide constituents give equal contributions to the effective mass average. The calculated electron effective

masses (0.3–0.5 m_e) are nearly isotropic in $RAMO_4$, and also resemble those in conventional binary TCOs. However, they do not follow the trend expected from the variation in the band gap: we find that the structures with fivefold coordinated metals exhibit smaller band gaps but larger electron effective masses as compared to their sixfold coordinated counterparts. This finding is explained based on the $\mathbf{k \cdot p}$ theory.

Thus, the above results highlight the advantages of incorporating light main group metals in multicomponent oxides, which is highly attractive for lighter-weight, less-expensive, and environmentally-friendly devices.

Further, we have systematically investigated how the structural peculiarities and the composition affect the formation of native point defects in $RAMO_4$. The studies are instructive for better understanding of the role of the defects in carrier generation and transport in doped and/or non-stoichiometric $RAMO_4$ oxides.

In Section 4, we studied the oxygen vacancy formation in three representative multicomponent $InAMO_4$ compounds with none, one and two light metal constituents. We find that the oxygen vacancy defect prefers to be located in the $InO_{1.5}$ layer for all three $InAMO_4$ materials which correlates with the heat of formation of the corresponding binary oxides. However, due to a large atomic relaxation near the defect and the formation of stable fourfold structures for Zn, Al, and Ga atoms, we obtained a significant reduction in the formation energy of the oxygen defect located in the $AMO_{2.5}$ layer. This additional energy gain results in a more uniform distribution of the oxygen vacancy defect throughout the layered structure of $InGaZnO_4$ and $InAlZnO_4$. In particular, the tendency of Zn, Ga, and Al atoms to form stable structures with lower oxygen coordination, results in nearly identical vacancy concentrations in the $InO_{1.5}$ and $GaZnO_{2.5}$ layers in $InGaZnO_4$, and only an order of magnitude lower concentration in the $AlZnO_{2.5}$ layer as compared to the one in the $InO_{1.5}$ layer in $InAlZnO_4$. The presence of two light metal constituents in the

InAlCaO$_4$ along with Ca failure to form a stable fourfold coordination as revealed by its negligible relaxation near the defect, leads to a strong preference of the oxygen vacancy to be in the InO$_{1.5}$ layer.

In Section 5, we have systematically investigated the formation of native point defects including both acceptor (cation vacancies, acceptor antisites) and donor (oxygen vacancies, donor antisites) defects in three representative multicomponent InAMO$_4$ compounds. We find that the donor antisite defects, such as Ga$_{Zn}$ in InGaZnO$_4$ and Al$_{Zn}$ in InAlZnO$_4$ have lower formation energies compared to that of the oxygen vacancies. The latter are the major donor defects in nonstoichiometric binary oxides and, by analogy, they were assumed to be the origin of conductivity in multicomponent oxides. Our results refute this assumption, and, for the first time, establish antisite defects as the most abundant electron donor defects in InGaZnO$_4$ and InAlZnO$_4$ materials.

Moreover, we find that the formation energy of cation vacancies in InAMO$_4$ are much lower than the formation energy of cation vacancies in binary TCOs. We explain this behavior based on the large structural relaxation around the defects in InAMO$_4$ associated with the unusual fivefold coordination of A and M atoms as well as the presence of the strong metal-oxygen bonds near the vacancy. The obtained equilibrium carrier concentration is in excellent agreement with the observed dependence of the conductivity on the oxygen partial pressure in InGaZnO$_4$. The results also explain why the InAlZnO$_4$ samples are unstable under a wide range of growing conditions.

BIBLIOGRAPHY

[1] D. S. Ginley and C. Bright. Special issue on transparent conducting oxides. *MRS Bulletin.*, 25:15–18, 2000.

[2] R.G Gordon. Criteria for choosing transparent conductors. *MRS Bulletin*, 25:52, 2000.

[3] D. S. Ginley, H. Hosono, and D. C. Paine. *Handbook of Transparent Conductors.* Springer, 2011.

[4] G. Rupprecht. Untersuchungen der elektrischen und lichtelektrischen leitfhigkeit dnner indiumoxydschichten. *Z. Phys.*, 139(504), 1954.

[5] A. Facchetti and T. Marks. *Transparent Electronics: From Synthesis to Applications.* John Wiley & Sons, New York, 2010.

[6] K. L. Chopra, S. Major, and D. K. Pandya. Transparent conductors – a status review. *Thin Solid Films*, 102:1–46, 1983.

[7] T. J. Coutts, D. L. Young, and X. Li. Characterization of transparent conducting oxides. *MRS Bulletin*, 25:58–65, 2000.

[8] H. Kaga, R. Asahi, and T. Tani. Thermoelectric properties of highly textured Ca-doped $(ZnO)_{(m)}In_2O_3$ ceramics. *Jpn. J. Appl. Phys*, 43:7133–7136, 2004.

[9] M. Orita, M. Takeuchi, H. Sakai, and H. Tanji. New transparent conductive oxides with $YbFe_2O_4$ structure. *Jpn. J. Appl. Phys.*, 34:L1550–L1552, 1995.

[10] M. Orita, H. Ohta, M. Hirano, S. Narushima, and H. Hosono. Amorphous transparent conductive oxide $InGaO_3(ZnO)_{(m)}$ ($m{\leq}4$): a Zn 4s conductor. *Phil. Mag. B*, 81:501–515, 2001.

[11] N. Kimizuka and T. Mohri. Structural classification of $RAMO_4$. *J. Solid State Chem*, 78:98–384, 1989.

[12] H. Hosono. *in Transparent Electronics: From Synthesis to Applications*, pages 459–487. John Wiley & Sons, 2010.

[13] K. Nomura, H. Ohta, A. Takagi, T. Kamiya, M. Hirano, and H. Hosono. Room temperature fabrication of transparent flexible thin-film transistors using amorphous oxide semiconductors. *Nature*, 432:488–492, 2004.

[14] K. Nomura, T. Kamiya, H. Yanagi, E. Ikenaga, and K. Yang. Subgap states in transparent amorphous oxide semiconductor, InGaZnO, observed by bulk sensitive x-ray photoelectron spectroscopy. *Appl. Phys. Lett*, 92:202117, 2008.

[15] J. E. Medvedeva. *in Transparent Electronics: From Synthesis to Applications*, pages 1–29. John Wiley & Sons, 2010.

[16] A. Murat and J. E. Medvedeva. Composition-dependent oxygen vacancy formation in multicomponent wide-band-gap oxides. *Submitted to Physical Review B*, 2012.

[17] T. Minami. Substitution of transparent conducting oxide thin films for indium tin oxide transparent electrode applications. *Thin Solid Films*, 516(7):1314–1321, 2008.

[18] A. Suresh, P. Gollakota, P. Wellenius, A. Dhawan, and J. F. Muth. Transparent, high mobility InGaZnO thin films deposited by PLD. *Thin Solid Films*, 516:7, 2008.

[19] J. E. Medvedeva and C. L. Hettiarachchi. Tuning the properties of complex transparent conducting oxides: Role of crystal symmetry, chemical composition, and carrier generation. *Physical Review B*, 81:125116, 2010.

[20] E. Wimmer, H. Krakauer, M. Weinert, and A. J. Freeman. Full-potential self-consistent linearized-augmented-plane-wave method for calculating the electronic structure of molecules and surfaces – O_2 molecule. *Phys. Rev. B*, 24:864–875, 1981.

[21] E. Wimmer. Computational materials design: A perspective for atomistic approaches. *Journal of Computer-Aided Materials Design*, 1(3):215–242, 1994.

[22] K. Capelle. A bird's-eye view of density-functional theory. 2006.

[23] A. E. Delahoy and S. Guo. *Transparent Conducting Oxides for Photovoltaics*, pages 716–796. John Wiley and Sons, Ltd, 2011.

[24] J. E. Medvedeva and A. J. Freeman. Combining high conductivity with complete optical transparency: A band-structure approach. *Europhys. Lett*, 69:583–587, 2005.

[25] E. Fortunato, D. Ginley, H. Hosono, and D. C. Paine. Transparent conducting oxides for photovoltaics. *MRS Bulletin*, 32:242–247, 2007.

[26] A. J. Freeman, K. R. Poeppelmeier, T. O. Mason, R. P.H. Chang, and T. J. Marks. Chemical and thin-film strategies for new transparent conducting oxides. *MRS Bulletin*, 25:45–51, 2000.

[27] T. S. Moss. The interpretation of the properties of indium antimonide. *Proc. Phys. Soc. B*, 67:775–782, 1954.

[28] E. Burstein. Anomalous optical absorption limit in InSb. *Phys. Rev. B*, 93:632–633, 1954.

[29] D. M. Bylander and L. Kleinman. Good semiconductor band gaps with a modified local-density approximation. *Phys. Rev. B*, 41:7868–7871, 1990.

[30] A. Murat and J. E. Medvedeva. Electronic properties of layered multicomponent wide-band-gap oxides: A combinatorial approach. *Phys. Rev. B*, 85:155101, 2012.

[31] A. Walsh, J. D. Silva, and S. Wei. Multi-component transparent conducting oxides: progress in materials modelling. *J. Phys.: Condens. Matter*, 23:334210, 2011.

[32] H. Un'no, N. Hikuma, T. Omata, N. Ueda, T. Hashimoto, and H. Kawazoe. Preparation of $MgIn_2O_{4-X}$ thin films on glass substrate by rf sputtering. *Jpn. J. Appl. Phys*, 32:L1260–L1262, 1993.

[33] H. Kawazoe, N. Ueda, H. Un'no, T. Omata, H. Hosono, and H. Tanoue. Generation of electron carriers in insulating thin film of $MgIn_2O_4$ spinel by Li^+ implantation. *J. Appl. Phys.*, 76:7935–7941, 1994.

[34] M. Orita, H. Tanji, M. Mizuno, H. Adachi, and I. Tanaka. Mechanism of electrical conductivity of transparent $InGaZnO_4$. *Phys*, 61:1811–1815, 2000.

[35] M. Orita, H. Tanji, M. Mizuno, H. Adachi, and I. Tanaka. Mechanism of electrical conductivity of transparent $InGaZnO_4$. *Phys. Rev. B*, 61(3):1811–1816, 2000.

[36] J. E. Medvedeva. Averaging of the electron effective mass in multicomponent transparent conducting oxides. *Europhys. Lett.*, 78:57004, 2007.

[37] J. E. Medvedeva. Unconventional approaches to combine optical transparency with electrical conductivity. *Appl. Phys. A*, 89:43–47, 2007.

[38] P. P. Edwards, A. Porch, M. O. Jones, and D. V. Morgan. Basic materials physics of transparent conducting oxides. *Dalton Trans*, 19:2995–3002, 2004.

[39] D. A. Drabold and S. K. Estreicher. *Theory of defects in semiconductors*. Springer, 2007.

[40] M. Yan, M. Lane, C. R. Kannewurf, and R. P. H. Chang. Highly conductive epitaxial CdO thin films prepared by pulsed laser deposition. *APL*, 78(16):2324, 2001.

[41] T. Minami. New n-type transparent conducting oxides. *MRS Bulletin*, 25:38–43, 2000.

[42] J. Osorio-Guillén, S. Lany, S. V. Barabash, and A. Zunger. Magnetism without magnetic ions: Percolation, exchange, and formation energies of magnetism-promoting intrinsic defects in CaO. *Phys. Rev. Lett.*, 96:107203, 2006.

[43] S. Lany and A. Zunger. Assessment of correction methods for the band-gap problem and for finite-size effects in supercell defect calculations: Case studies for ZnO and GaAs. *Physical Review B*, 78(23):235104, 2008.

[44] S. Lany and A. Zunger. Dopability, intrinsic conductivity and nonstoichiometry of transparent conducting oxides. *Phys. Rev. Lett.*, 98:045501, 2007.

[45] J. Robertson and S. J. Clark. Limits to doping in oxides. *PRB*, 83(07525), 2011.

[46] H. Omura, H. Kumomi, K. Nomura, T. Kamiya, M. Hirano, and H. Hosono. First-principles study of native point defects in crystalline indium gallium zinc oxide. *J. Appl. Phys*, 105(093712), 2009.

[47] M. Weinert, E. Wimmer, and A. J. Freeman. Total-energy all-electron density functional method for bulk solids and surfaces. *Phys. Rev. B*, 26:4571–4578, 1982.

[48] M. Weinert, G Schneider, R Podloucky, and J Redinger. FLAPW: applications and implmentations. *J. Phys.: Condens. Matter*, 21, 2009.

[49] P. Hohenberg and W.Kohn. Inhomogeneous electron gas. *Physical Review*, 136:136, 1964.

[50] R. M. Martin. *Electronic Structure: Basic Theory and Practical Methods*. Cambridge University Press, 2004.

[51] L. H. Thomas. The calculation of atomic fields. *Proc. Camb. Phil. Soc.*, 23(542), 1927.

[52] E. Fermi. *Z. Phys*, 48(73), 1928.

[53] W. Kohn and L. J. Sham. Self-consistent equations including exchange and correlation effects. *Phys. Rev*, 140:A1133, 1965.

[54] M. Born and R. Oppenheimer. Zur quantentheorie der molekeln. *Ann. Phys. Lpz*, 84:124, 1927.

[55] B. G. Johnson, P. M. W. Gill, and J. A. Pople. The performance of a family of density functional methods. *J. Chem*, 98:5612, 1993.

[56] A. Garcia, C. Elsaesser, J. Zhu, S. Louie, and M. L. Cohen. Use of gradient-corrected functionals in total-energy calculations for solids. *Phys. Rev. B*, 46:9829, 1992.

[57] A. Seidl, A. Görling, P. Vogl, J. A. Majewski, and M. Levy. Generalized kohn-sham schemes and the band-gap problem. *Phys. Rev. B*, 53:3764–3774, 1996.

[58] A. D. Perdew. Density-functional approximation for the correlation energy of the inhomogeneous electron gas. *J.P., Phys. Rev.,*, B33, 1986.

[59] C. Stampfl, M. Kim, G. Profeta, R. Asahi, W. Mannstadt, and A. J. Freeman. *The full-potential linearized augmented plane-wave code FLAPW: Users guide*, 2002.

[60] J. C. Slater. Wave functions in a periodic potential. *Phys. Rev*, 51(846), 1937.

[61] O. K. Anderson. Linear methods in band theory. *Phys. Rev. B*, 12:3060, 1975.

[62] D. D. Koelling and G. O. Arbman. Use of energy derivative of the radial solution in an augmented plane wave method: application to copper. *J. Phys. F*, 5(2041), 1975.

[63] H. J. F. Jansen and A. J. Freeman. Total-energy full-potential linearized augmented-plane-wave method for bulk solids: Electronic and structural properties of tungsten. *Phys. Rev. B*, 30:561, 1984.

[64] A. Canning, W. Mannstadt, and A.J. Freeman. Parallelization of the FLAPW method. *Computer Physics Communications*, 2000.

[65] C. G. Broyden. A class of methods for solving nonlinear simultaneous equations. *Math. Comp*, 19:577, 1965.

[66] G. Thomas. Invisible circuits. *Nature*, 389:907 –908, 1997.

[67] P. P. Edwards, A. Porch, M. O. Jones, D. V. Morgan, and R. M. Perks. Basic materials physics of transparent conducting oxides. *Dalton Trans*, 19:2995–3002, 2004.

[68] D. S. Ginley, H. Hosono, and D. C. Paine. *Handbook of Transparent Conductors*. Springer, 2011.

[69] R. D. Shannon, J. L. Gillson, and R. J. Bouchard. Single crystal synthesis and electrical properties of $CdSnO_3$, Cd_2SnO_4, In_2TeO_6, $CdIn_2O_4$. *J. Phys. Chem. Solids*, 38:877–881, 1977.

[70] A. L. Dawar and J. C. Joshi. Semiconducting transparent thin films: their properties and applications. *J. Mater. Sci*, 19:1–23, 1984.

[71] J. M. Phillips, J. Kwo, and G. A. Thomas. Transparent conducting thin films of $GaInO_3$. *Appl. Phys. Lett*, 65:115–117, 1994.

[72] H. Kawazoe and K. Ueda. Transparent conducting oxides based on the spinel structure. *J. Amer. Ceram. Soc*, 82:3330–3336, 1999.

[73] B. J. Ingram, G. B. Gonzalez, D. R. Kammler, M. I. Bertoni, and T. O. Mason. Chemical and structural factors governing transparent conductivity in oxides. *J. Electroceram.*, 13:167–175, 2004.

[74] V. K. Kato, I. Kawada, N. Kimizuka, and T. Katsura. Die kristallstructur von $YbFe_2O_4$. *Z. Krist*, 141:314–320, 1975.

[75] N. Kimizuka and T. Mohri. Spinel, $YbFe_2O_4$, and $Yb_2Fe_3O_7$ types of structures for compounds in the In_2O_3 and Sc_2O_3-A_2O_3-BO systems [A: Fe, Ga or Al; B: Mg, Mn, Fe, Ni, Cu or Zn] at temperatures over 1000 C. *J. Solid State Chem*, 60:382–384, 1985.

[76] D. M. Bylander and L. Kleinman. Good semiconductor band gaps with a modified local-density approximation. *Phys. Rev. B*, 41:7868–7871, 1990.

[77] R. Asahi, W. Mannstadt, and A. J. Freeman. Optical properties and electronic structures of semiconductors with screened-exchange LDA. *Phys. Rev. B*, 59:7486–7492, 1999.

[78] C. B. Geller, W. Wolf, S. Picozzi, A. Continenza, R. Asahi, W. Mannstadt, A. J. Freeman, and E. Wimmer. Computational band-structure engineering of iii-v semiconductr alloys. *Appl. Phys. Lett.*, 79:368, 2001.

[79] M. Y. Kim, R. Asahi, and A. J. Freeman. Excited states and optical properties entirely from first principles: Extended FLAPW method and its graphical user interface. *J. Comput.-Aided Mater. Des.*, 9:173, 2002.

[80] N. Kimizuka, T. Mohri, and Y. Matsui. Homologous compounds. *J. Solid State Chem.*, 74:98–109, 1988.

[81] C. Li, Y. Bando, M. Nakamura, and M. Kimizuka. A modulated structure of $In_2O_3(ZnO)_{(m)}$ as revealed by high resolution electron microscopy. *J. Electron Microsc*, 46:119–127, 1997.

[82] H. Peng, J. H. Song, E. M. Hopper, Q. Zhu, T. O. Mason, and A. J. Freeman. Possible n–type carrier sources in $In_2O_3(ZnO)_k$. *Chemistry of Materials*, 24(1):106–114, 2012.

[83] A. Murat and J. E. Medvedeva. Native point defects in multicomponent transparent oxide hosts. *Submitted to Physical Review B*, 2012.

[84] Katsuyuki Matsunaga, Tomohito Tanaka, Takahisa Yamamoto, and Yuichi Ikuhara. First-principles calculations of intrinsic defects in Al_2O_3. *Phys. Rev. B*, 68:085110, 2003.

[85] J. E. Medvedeva, E. N. Teasley, and M. D. Hoffman. Electronic band structure and carrier effective mass in calcium aluminates. *Phys. Rev. B*, 76:155107, 2007.

[86] A.Adler and T. Mason. Unpublished.

VITA

Altynbek Murat was born in Bayan-Ulgii, Mongolia. He graduated from Mongolian-Turkish high school in 2002. He was awarded a full scholarship to study at United Arab Emirates University. In May 2007, he received his Bachelors of Science degree in Physics from UAE University. Upon his graduation from UAE University, he was awarded with a UAE President's Gold Medal Award for his academic excellence. In August 2007 he enrolled as a PhD student at Missouri University of Science and Technology. In 2011, he received his Master of Science degree in Engineering Management from Missouri S&T. In 2012, he earned his Doctor of Philosophy in Physics from Missouri S&T. While at Missouri S&T, Altynbek greatly enjoyed his work as a graduate research assistant to Dr. Julia E. Medvedeva for five years. He was awarded with several competitive grants to present his research and to participate in national and international scientific conferences. In addition, Altynbek earned multiple competition prizes for research presentations and showcases at the Missouri S&T.